Universidade de Aveiro
2019
Departamento de electrónica, telecomunicações e informática

Samaneh Moeini

Metamateriais Electromagnéticos Baseados em Geometria Fractal

Electromagnetic Metamaterials Based on Fractal Geometry

Universidade de Aveiro
2019

Departamento de electrónica, telecomunicações e informática

Samaneh Moeini

Metamateriais Electromagnéticos Baseados em Geometria Fractal

Electromagnetic Metamaterials Based on Fractal Geometry

Tese apresentada à Universidade de Aveiro para cumprimento dos requisitos necessários à obtenção do grau de Doutor em Engenharia Eletrotécnica-Telecomunicações, realizada sob a orientação científica do Doutor José Carlos Esteves Duarte Pedro, Professor Catedrático do Departamento de Electrónica, Telecomunicações e Informática da Universidade de Aveiro

Apoio financeiro da FCT/MEC no âmbito de fundos nacionais (PD / BD / 52589/2014)

*"**The only true voyage of discovery, the only fountain of Eternal Youth, would be not to visit strange lands but to possess other eyes**, to behold the universe through the eyes of another, of a hundred others, to behold the hundred universes that each of them beholds, that each of them is; and this we can contrive with an Elstir, with a Vinteuil; with men like these we do really fly from star to star."*

Marcel Proust [1]

o júri

presidente

Prof. Doutor Victor Miguel Carneiro de Sousa Ferreira
Professor Catedrático, Universidade de Aveiro

Prof. Doutor Carlos António Cardoso Fernandes
Professor Catedrático, Universidade de Lisboa

Prof. Doutor Henrique Manuel de Castro Faria Salgado
Professor Associado, Universidade do Porto

Prof. Doutor António Luís Campos da Silva Topa
Professor Auxiliar, Universidade de Lisboa

Prof. Doutor Sérgio de Almeida Santos
Professor Auxiliar, Iscte - Instituto Universitário de Lisboa

palavras-chave metamateriais, homogeneização, fractais, auto-similaridade.

resumo

Nas tendências de crescimento de diversas áreas tecnológicas, os metamateriais abriram novas oportunidades no controlo da radiação eletromagnética para aplicações avançadas. Existem diferentes tipos de metamateriais que: a) oferecem valores negativos para as partes reais da permitividade e/ou permeabilidade efetivas [meio duplamente negativo (DNG)]; b) proporcionam valores extremamente elevados e/ou anisotrópicos desses parâmetros [por exemplo, meios de fios condutores (WM)]; e c) apresentam valores próximos de zero desses parâmetros, como nos meios de permitividade elétrica próxima de zero (ENZ) ou de permeabilidade magnética próxima de zero (MNZ).

Uma das formas mais comuns dos metamateriais concebidos para aplicações de microondas são estruturas periódicas regulares. Embora a periodicidade possa às vezes ser uma propriedade necessária (como, por exemplo, nos metamateriais fotónicos de bandas proibidas (PBG)), algumas outras formas, como os meios de fios condutores (WM), não precisam ser periódicas para oferecer a mesma permitividade efectiva do material de tipo plasma. Além disso, a periodicidade em metamateriais projetados para a supressão da propagação pode abrir novas bandas nas quais as ondas podem se propagar.

Recentemente, a eletrodinâmica de estruturas fractais tem vindo a atrair uma grande atenção na conceção de dispositivos de microondas e ópticos e nas suas aplicações. Os fractais são padrões geométricos cujas dimensões topológicas não pode ser sempre representada por um número inteiro. Em vez disso, as dimensões nos fractais são descritas por outras definições, como a dimensão de Hausdorff. Devido ao seu padrão de auto-repetição, os fractais trazem novas oportunidades à conceção de metamateriais.

Neste trabalho, a abordagem fractal-geométrica foi estudada para construir diferentes tipos de metamateriais. Especificamente, os objetivos do projeto são modelar as características eletromagnéticas desses metamateriais com base em diferentes tipos de fractais; e fornecer novas técnicas de homogeneização para este grupo de metamateriais.

Para expandir ainda mais as aplicações da geometria fractal neste contexto, o novo conceito de metamateriais de codificação fractal foi também desenvolvido e estudado no âmbito deste projeto.

keywords metamaterials, homogenization, fractals, self-similarity.

abstract

In the growing trends in different technological areas, metamaterials opened new opportunities for controlling electromagnetic radiation for advanced applications. There are different types of metamaterials that a) offer negative values for the real parts of effective permittivity and/or permeability [double-negative (DNG) media]; b) provide for extremely high and/or anisotropic parameters (e.g., wire media); and c) have near-zero values of these parameters as in electric near-zero (ENZ) or magnetic near-zero (MNZ) media.

One of the most common forms of the metamaterials designed for microwave applications are regular periodic structures. Although periodicity can be sometimes a necessary property (like, for example, in the photonic band-gap (PBG) metamaterials), some other forms such as wire medium (WM) do not really need to be periodic to provide the same plasma-like effective permittivity. Moreover, periodicity in metamaterials designed for suppression of the propagation may open new bands in which waves can propagate.

Recently, electrodynamics of fractal structures caught a vast attention in the design of microwave and optical devices and their applications. Fractals are geometric patterns whose topological dimensions cannot be always represented by an integer number. Instead, dimensions in fractals are described by other definitions such as the Hausdorff dimension. Due to their self-repeating pattern, fractals can bring new opportunities in the design of metamaterials.

In this work, the fractal-geometric approach has been studied in order to build different types of metamaterials. Specifically, the project objectives are to model electromagnetic characteristics of these metamaterials based on different types of fractals; and to provide new homogenization techniques for this group of metamaterials.

To further expand the idea of fractal applications, the new concept of fractal coding metamaterials also has been developed and studied in the framework of this project.

Acknowledgments

This journey would not have been possible without the support of my supervisor, Professor José Carlos Pedro. His help during all these years was beyond being just a scientific advisor; I had learned from him how to look at problems and approach solutions. My special thanks go to him for having trust in me and giving me freedom to investigate different ideas in the course of this work.

I would like to extend my gratitude also to Professor Tie Jun Cui and to his team for the awesome three months spent for the research visit at the Southeast University, China. It was one of the best experiences of my PhD.

There are people whose efforts are reflected in this work, and those whose help was invisible and yet fundamental for my life and my achievements. Those who taught me, corrected my misinterpretations, who guided me: My dear family, the great teachers, the supportive friends, the kind colleagues — I would like to thank them all.

I would like to give very special thanks to my wonderful parents who made me friends with books. This friendship never faded.

In the "Cosmos: A Spacetime Odyssey" series, Neil Tyson recalls that he always knew he wanted to become a scientist, but after meeting Carl Sagan, he learned from Carl the kind of person he wanted to become. I do feel the same for my husband, the love of my life. There is no word that can describe my gratitude to him for being a part of this journey and the most important part of my life.

Last, if I could, I would send my tremendous thanks to the composers Pyotr Ilyich Tchaikovsky and Giuseppe Verdi, whose music filled my days with joy in the noisy room 33.1.43 in IT Aveiro.

I dedicate this work to my loving and supportive family. You give me strength to go through the adventures of my life.

Contents

List of Figures

Abbreviations

BC	**B**oundary **C**ondition
CNC	**C**omputer **N**umerical **C**ontrol
CST	**C**omputer **S**imulation **T**echnology
DNG	**D**ouble **N**e**G**ative
EBG	**E**electromagnetic **B**and **G**ap
EM	**E**lectro**M**agnetic
ENZ	**E**lectric **N**ear-**Z**ero
FDTD	**F**inite **D**ifference **T**ime **D**omain
FIF	**F**ractal **I**nterpolation **F**unction
FOM	**F**igure **O**f **M**erit
FSS	**F**requency **S**elective **S**urface
IFS	**I**terated **F**unction **S**ystem
MEEP	**M**IT **E**lectromagnetic **E**quation **P**ropagation
MM	**M**eta**M**aterial
MNZ	**M**agnetic **N**ear-**Z**ero
MPB	**M**IT **P**hotonic-**B**ands
NIM	**N**egative **I**ndex **M**aterials
NRW	**N**icolson-**R**oss-**W**eir
PBG	**P**hotonic **B**and-**G**ap
PCB	**P**rinted **C**ircuit **B**oard
RCS	**R**adar **C**ross **S**ection
SRR	**S**plit **R**ing **R**esonator
TE	**T**ransverse **E**lectric
TM	**T**ransverse **M**agnetic
WM	**W**ire **M**edium

Dedicated to my family

Chapter 1

Introduction

1.1 Metamaterials: a Brief History

Metamaterials (MMs) are under active research since the beginning of this millennium. These materials are patterned composites in which we change the overall material response (electric, magnetic, or mechanical) by using different material constituents in order to obtain the properties that we need. Usually the patterns in metamaterials are repeating.

There are various types of metamaterials such as negative index materials (NIM), electromagnetic band gap (EBG) materials, frequency selective surface (FSS) based metamaterials, and others. Fig. 1.1 shows the classification of magneto-dielectric materials and MMs based on their μ and ε values.

Theoretical prediction of the media with simultaneously negative permittivity and permeability first appeared in the V. Veselago's paper in 1968 [2]. Although there is no natural material with such properties [3], in the 1990s, J. Pendry proposed the use of composite materials comprising conducting metallic wires [4] for negative permittivity, and split ring resonators (SRRs) for negative permeability [5]. Later, R. Shelby and D. Smith successfully fabricated and examined the first DNG medium by combining these ideas [6]. Their material operated at a specific frequency in the microwave band. Since then there has been active research on different phenomena in these materials such as: negative refraction; super-resolution focusing [7, 8]; invisibility cloaking [9–11]; photonic band-gap [12–14] and nonlinear effects [15–17].

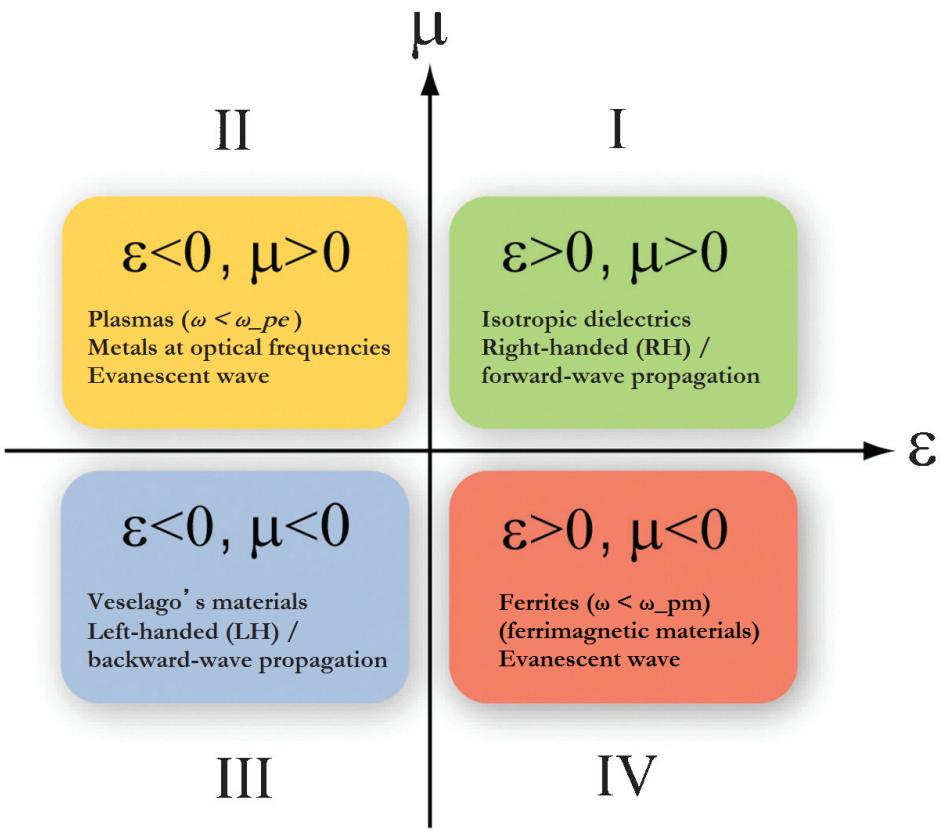

FIGURE 1.1: Permittivity-permeability (ε-μ) diagram where ω is angular frequency and ω_{pe} and ω_{pm} represent the electric and magnetic plasma frequencies, respectively.

Since the birth of the MM era, there have been different proposals to design and fabricate MMs with good quality and desired ε and μ. Some of the well-known structures include Ω-rings [18], S-rings [19], metallic rod pairs [20, 21], and metallic crosses [22].

The concept of macroscopic electromagnetics using averaged microscopic field quantities was first proposed by Plank [23]. By expanding this idea, characterization of the effective responses of MMs became possible [24, 25]. Due to the complexity of the MM structures, and in order to have accurate and efficient techniques for determining the EM response of a given structure, different EM characterisation methods were proposed. Describing complex MMs by a set of a few effective parameters is desirable in engineering applications. This observation gave rise to a class of characterization techniques known as the homogenization methods. These methods rely on the fact that, when the distances between the elements of a MM are small compared to the wavelength, the MM is effectively continuous and can be understood as a homogeneous medium.

There are macroscopic methods belonging to this class, which are based on the results of physical or numerical experiments such as measurements or simulations of the reflection

and transmission coefficients of the MM samples. In particular, in the Nicolson-Ross-Weir retrieval method (NRW) [26, 27], a layered MM structure is described as a bulk material with effective parameters μ and ε retrieved from the reflection-transmission measurements or simulations. Although the NRW method comes with a rather simple formulation, the ambiguity in choosing the right branch of the complex logarithm function (due to the 2π periodicity in the phase of the transmitted signal) involved in the calculations of the effective refractive index, and, respectively, the effective permittivity and permeability, makes the use of this method problematic for thick MM samples.

Various generalizations of the NRW method using the inversion of computed or measured scattering data [28, 29] exist. These methods usually perform poorly in MMs with bianistropic and spatially dipersive effects. They as well suffer from the branch uncertainities and give multiple answers for the homogenization problem, so that, in some cases, it is not easy to determine the right solution, although certain methods have been proposed to reduce this ambiguity [30–32].

Another group of the EM characterization methods is based on the microscopic point of view at the MM lattice level. These methods determine the EM behavior of the MMs by studying the complex EM response of their unit cells. The unit cell response is determined not only by its chemical composition, but also by the geometric properties of the unit cell elements, the lattice symmetry, etc. However, in contrast to the photonic crystals whose complex EM behavior results dominantly from their periodicity and granularity, the homogenizable MMs are effectively continuous structures. The material parameters of such homogenizable periodic MMs can be determined, for instance, with the source driven homogenization methods [33], or by using the multipolar expansion [34].

For the MM with periods much smaller than the wavelength, or random dense MM, the classical analytical homogenization theories [35] can be used. These methods consider the MM as a composite or mixture of two or more components and define the MM effective parameters by using, e.g. the Clausius-Mossotti (Maxwell-Garnett) or the coherent potential approximations [36]. These theories are valid under certain limitations and are often not applicable to MMs formed by conductors and resonators with high inclusion volume fractions. Besides that, these methods do not take into account the spatial dispersion resulting from the periodicity of the MM.

There are methods which use the band structure of the MM to obtain the effective parameters, but such methods usually are not applicable within the EM band gaps or in the MM structures with high losses. Special homogenization techniques based on the plane wave expansion and the band structure calculations [37] and on the combination of asymptotic multiscale methods with wave-field conception [38] are also known.

1.2 Fractal Geometry and its Applications

Fractal geometry can be seen as an extension of the classical geometry. Fractals can be described by irregular mathematical sets that provides better representation of many natural phenomena than the classical approach [39].

Although fractals have been around for centuries, application of fractal geometry in EM design is a relatively new area. The term "fractal" was, itself, first coined by B. Mandelbrot in 1975 from the Latin word "fractus" meaning made-up of broken or irregular fragments. By Mandelbrot definition, a fractal is a set for which the Hausdorff–Besicovitch dimension strictly exceeds the topological dimension. Unlike Euclidean geometrical figures, if a fractal's 1-D length is doubled, the spatial content of fractal scales gets a fractal dimension that exceeds the fractal topological dimension. The latter is not necessarily an integer. This fractal dimension is the Hausdorff–Besicovitch dimension that was first introduced by Felix Hausdorff in 1918 and is a measure of the local size of a set of numbers. In traditional geometry, it's an integer corresponding to the topology of the structure.

However, we cannot describe all different types of fractals by Mandelbrot definition. In the more general mathematical description, fractal is a set with the following properties:

- having a fine structure: available details on arbitrary small scales,
- being too irregular,
- having some form of self-similarity,
- usually fractal dimension[1] is strictly bigger than topological dimension,
- mostly you can describe them by simple definitions e.g. recursively.

[1] The term fractal dimension in this thesis always refers to Hausdorff–Besicovitch dimension.

Fractals usually have repeating patterns at every scale. The replication can be exactly the same at each scale (self-similar pattern, e.g. Koch Snowflake) or nearly the same (e.g. Mandelbrot set), or it can have a detailed pattern that repeats itself but does not show self-similar behaviour even statistically (e.g. coastline [40]).

Self-similar fractals can be classified according to their correlation at different scales as deterministic or random (statistically self-similar). Deterministic fractals can have geometrical replication or algebraic replication. Fig. 1.2 depicts a few examples of different classes of fractals.

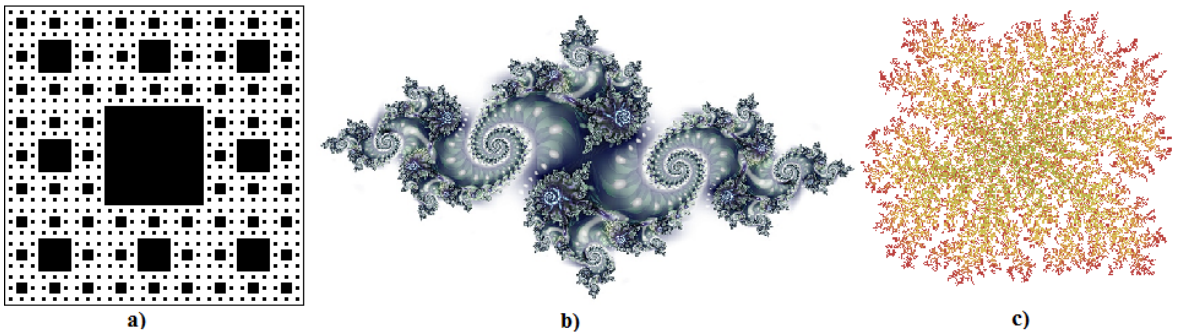

FIGURE 1.2: Some examples of different fractal geometries: a) Sierpinski carpet (deterministic geometric fractal); b) Julia set (deterministic algebraic fractal); c) Brownian tree (non-deterministic random fractal)

The application of fractals in engineering designs is very recent. In particular, fractals in EM designs dates back to 1986 when they were used in the design of linear arrays of antennas [41].

Many types of fractals can be used in high-frequency designs to achieve desired EM characteristics. One of the most interesting possibilities in fractal approach to antenna design is that with using such structures one may develop invariant frequency antennas or multiband antennas due to the mentioned self-similarity property of fractals [42]. With respect to this property a fractal antenna is similar to a log-periodic antenna. Fractal approach to the design of reflectarray unit cells resulted in improved properties such as miniaturization and low loss [43].

Enhanced diffraction properties can be obtained by using Sierpinski gasket [44]. Fractals also have been used for wave localization at microwave and terahertz frequencies [45, 46]. Eigenmodes in a fractal cavity have been studied in [47]. There has been also some research on using fractal structures in optical transmission [48–50].

Fractal structures share some similarity in properties with MMs [51].

Besides the interesting properties of fractals in antenna and high frequency designs, there have been some investigations toward using them in metamaterial design. The most common fractal that has been used in different studies of MMs is the H-shape fractal. Due to the multiband and sub-wavelength behavior, it has been used to build electric MMs [52–54], magnetic MMs made of metallic planar fractal structures and metallic sheets [55, 56], and palsmonic MMs comprising metallic plates drilled with periodic fractal slits [57, 58].

1.3 Research Gaps

Although the idea of MMs is very interesting and brought novel perspectives to various applications, the existing structures for MMs are far from practical use in many applications. Among them, structures with resonant elements do not provide a good transmission medium due to low intrinsic quality factor that is associated with each resonator [59]. On the other hand, as it has been pointed out before, these structures besides being bulky, exhibit narrowband behaviour and have high loss.

There has been successful research on electrodynamics of fractals but there is not too much focus on using fractal geometry in MM designs. The well-studied MMs typically have simple periodic structures of very narrowband nature. On the other hand, fractal structures are typically aperiodic, being thought for wideband operation.

Particularly, the focus in electrodynamics of fractal structures has been on the calculation of dispersion diagrams or impedances in fractal antennas and, only for a few known structures, it has been done in a general way.

Besides the limitations in MM structures, the known analytical methods for homogenization of MMs are too limited and do not cover the wide variety of MM structures. Although there are exact methods for periodic MMs, the homogenization methods for aperiodic MMs are still under development and just a few approximate methods exist in this case. Developing a more general analytical method for homogenization of MMs based on their geometry is an important step towards using MMs in engineering applications.

The known homogenization theories for random media are not directly applicable for fractal structures, because fractal structures possess a much higher degree of order as compared to disordered media. In particular, the existing methods for periodic MM rely on strict

periodicity of the medium, and are not applicable to fractal structures, which are not periodic. On the other hand, the methods for random media rely on randomness in the positions of inclusions, but again for many fractals this property does not hold: fractals are self-repeating structures, but generally not random.

In contrast, depending on the type of fractal chosen for a fractal MM, the structural MM elements may drastically vary in size, orientation, and electrical properties. For instance, such elements can become electrically connected or disconnected, be scaled, rotated, etc., within a single fractal MM sample. In order to study such structures, the scattering properties of the microscopic building blocks have to be thoroughly analysed, which will later allow for a general macroscopic description of the fractal MM itself.

1.4 Objectives

The focus of this thesis is on the study of EM behaviour of MMs based on self-similar fractals. This is done numerically and, when possible, by deriving analytical formulas. Different fractal MMs in 1D, 2D , and 3D are investigated, and applicable homogenization techniques for each class are developed.

The result of this work provides better understanding of the EM behaviour of these structures in general.

In particular, a special attention is paid to self-similar fractals due to their potential in the prediction of the system behaviour at different scales. Such structures find applications where self-repeating (at different scales) patterns of the structural elements lead to improvements in the performance of the structure.

Apart from the study of fractal MMs, a new coding strategy based on fractal interpolation function is introduced. Taking advantage of the mathematical properties of the fractals, an analytical approach for fractal coding MMs is developed.

1.5 Thesis outline

In the part I of this work, in chapter 2, we design one-dimensional fractal metamaterials and derive the effective parameters of such structures. In chapter 3, the design of a two-dimensional metamaterial based on the Hilbert curve [60] has been studied. A homogenization technique applicable to this type of fractal MMs has been developed and an equivalent circuit model based on the Babinet's principle [61] has been proposed. In chapter 4, we present a three-dimensional fractal metamaterial based on the Sierpinski carpet and investigate the features of this fractal WM that it can offer in contrast to the traditional MMs such as the wire medium.

In the part II, in chapter 5, we propose the new concept of the fractal coding MMs. Using a fractal interpolation function we derive a theoretical model for this class of structures. The theory has been verified through numerical simulations and confirmed with an experiment. Chapter 6 highlights the main achievements and draws the main conclusions of this thesis project.

The results of this thesis are published in Refs. [62–68].

Part I

Metamaterials based on Fractals

Chapter 2

1D MM based on Deterministic Geometrical Fractal:

Layered Dielectric based on a Fractal Set

The purpose of this chapter is to develop a method to derive the effective material parameters of such a complex MM, that is, to homogenize it. In the first section, we develop a transfer matrix-based homogenization approach applicable to self-similar fractal structures. With this method, we derive the material parameters of a layered fractal MM comprising two different dielectrics with permittivities equal to ε_1 and ε_2, respectively, in which the layers are distributed based on a fractal set. In the second section, we develop homogenization techniques on the spatial scale Λ such that $L \ll \Lambda$, where Λ is the characteristic wavelength of the external electromagnetic field which excites the structure.

In this work, we are interested in fractal MMs, constituents of which follow a fractal down-scaling rule and therefore have (theoretically) infinitely many internal parts of infinitesimal dimensions. Here, the self-similarity properties of fractals are exploited for proposing a new homogenization method for such MMs based on fractal geometry.

2.1 Extraction of Material Parameters

The example structure we consider for this work is a layered fractal MM comprising two different dielectrics. In this case, an unbounded fractal MM can be formed by periodically

repeating fractal unit cells.

This structure is shown in Fig. 2.1, with the z-axis oriented perpendicularly to the layers. The structure is infinite and regular in the xy-plane.

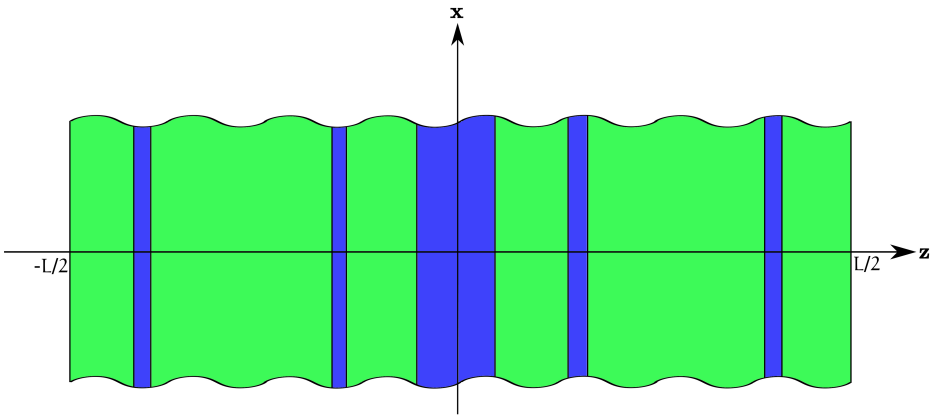

FIGURE 2.1: The geometry of the proposed fractal structure (third order). The third order fractal has 11 dielectric layers. The blue color corresponds to permittivity $\varepsilon_{\mathrm{r}} = \varepsilon_1$ and the green layers correspond to $\varepsilon_{\mathrm{r}} = \varepsilon_2$.

Along the z-axis, the MM is formed by periodically repeated fractal cells of length L, with the geometry of each cell obtained as follows: In the first order fractal (Fig. 2.2a), we consider a cell formed by three layers (a triplet): the middle dielectric layer with permittivity ε_1 and thickness d_1, and the two outer layers with permittivity ε_2 and thickness d_2. One such cell has thickness $L = d_1 + 2d_2$. By increasing the fractal order, the outer layers of the first-order cells are replaced by triplets of layers which are geometrically self-similar to the original cells, but with the roles of the two dielectrics interchanged, i.e., ε_1 is replaced with ε_2 and *vice versa*. For a fractal of n-th order this procedure is repeated $n - 1$ times. The resulting profiles for the first four iterations $\varepsilon_{\mathrm{r}}(z)$ are shown in Fig. 2.2.

Thus the geometrical structure of an infinite-order fractal cell of length L can be defined with a single dimensionless parameter: The ratio between the thickness of the outer layers in the first-order cell to the total length of the cell, $r = \frac{d_2}{L}$, which we call *fractal ratio*. By definition, $0 \leq r < 0.5$. As is easy to verify, when $r = 0$, the whole MM is a uniform dielectric with permittivity ε_1. On the other hand, when $r \to 0.5$ the fractal cells do not reduce to a uniform dielectric with permittivity ε_2. Instead, in this limit the cells are formed by interlacing dielectric layers with infinitesimal thickness and permittivities ε_1, ε_2.

In the following we consider a structure having just one such cell. The effective parameters of the 1D fractal medium can be calculated analytically using the transfer (ABCD) matrix

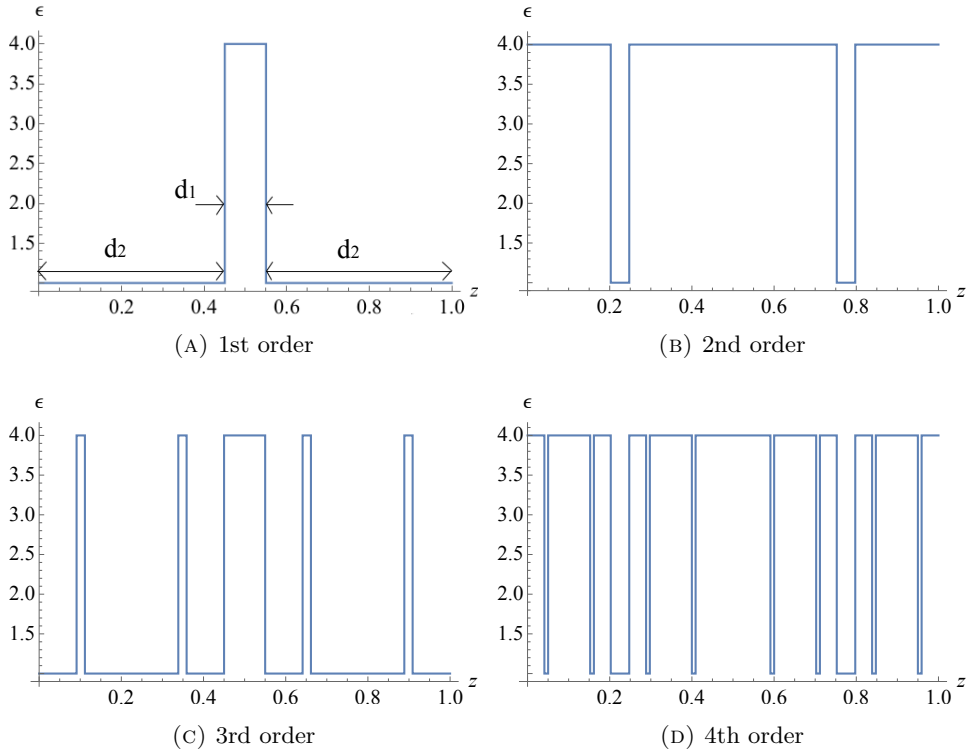

(A) 1st order (B) 2nd order

(C) 3rd order (D) 4th order

FIGURE 2.2: ε profile for different orders of fractal MM. In this example, $L = d_1 + 2 \times d_2 = 1$, $d_2 = 0.45L$, $\varepsilon_1 = 4$ and $\varepsilon_2 = 1$.

approach. The transfer matrix, A, is defined as follows [69]:

$$\begin{pmatrix} E_{x1} \\ H_{y_1} \end{pmatrix} = A_{\text{diel}} \cdot \begin{pmatrix} E_{x2} \\ H_{y_2} \end{pmatrix}, \tag{2.1}$$

in which $E_{x1,2}$ and $H_{y_{1,2}}$ are the transverse fields at the input and the output of the structure and A_{diel} is the transfer matrix of a dielectric layer which can be written as shown below [70] (for the time dependence of $\exp(-i\omega t)$; where $i = \sqrt{-1}$):

$$A_{\text{diel}} = \begin{pmatrix} \cos kd & -i\eta \sin kd \\ -\dfrac{i}{\eta} \sin kd & \cos kd \end{pmatrix}, \tag{2.2}$$

where d is the thickness of the dielectric layer, and

$$\eta = \eta_0 \sqrt{\frac{\mu_r}{\varepsilon_r}}, \tag{2.3}$$

$$k = k_0 \sqrt{\varepsilon_r \mu_r}, \tag{2.4}$$

and η_0 and k_0 are the wave impedance and the wave propagation factor in free space, respectively.

For nonmagnetic materials, we have $\mu_r = 1$ and if we use the field units such that $\eta_0 = 1$, the equation for A_{diel} with relative permittivity ε_r can be simplified as shown below:

$$A_{\text{diel}} = \begin{pmatrix} \cos k_0\sqrt{\varepsilon_r}d & -i\dfrac{\sin k_0\sqrt{\varepsilon_r}d}{\sqrt{\varepsilon_r}} \\ -i\sqrt{\varepsilon_r}\sin k_0\sqrt{\varepsilon_r}d & \cos k_0\sqrt{\varepsilon_r}d \end{pmatrix}. \tag{2.5}$$

Using these expressions, the total transfer matrix of a stack of dielectric layers is calculated as an ordered product of the transfer matrices of the separate layers.

2.1.1 Eigenvalues of the Transfer Matrix and the Band Dispersion Diagram

By knowing the eigenvalues of the transfer matrix, the band diagram [71, p. 29] of the structure can be calculated. The eigenvalues $\Lambda_{1,2}$ of the total transfer matrix are related to the propagation factors $k_z = k_0\sqrt{\varepsilon_{\text{eff}}}$ as $\Lambda_{1,2} = \exp^{\pm ik_zL}$. Within propagation bands, k_z is real (when there is no loss) and the two eigenvalues of the transfer matrix are complex conjugate of each other. On the other hand, within stopbands, k_z is purely imaginary and the two eigenvalues have distinct real values.

The band diagram (the dispersion characteristic) for the fractal structure of 9th order obtained with the transfer matrix approach is shown in Fig. 2.3. In this diagram, the propagation factor k_z is calculated as

$$k_z = \frac{1}{L}|\text{Im}(\log\Lambda_1)|. \tag{2.6}$$

2.1.2 Effective Permittivity in the Quasi-Static Approximation

When the fractal order is increasing, the total number of layers in the structure grows very fast (in geometric progression), which makes direct numerical computation of the total transfer matrix and the band diagram inefficient. Therefore, to describe fractal structures of order $n \to \infty$, an alternative approach is needed.

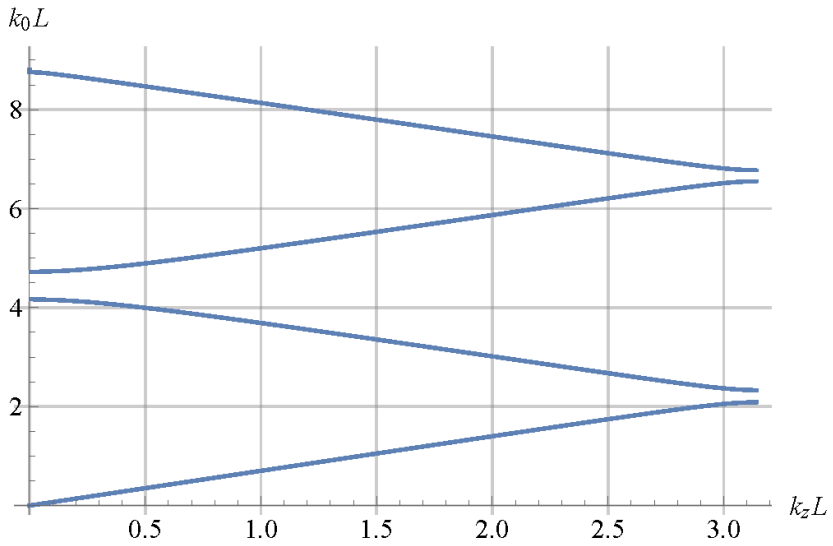

FIGURE 2.3: The band diagram for the 9th order fractal MM. Four propagation bands and three band gaps are seen in the diagram.

In order to develop such approach, we note that the transfer matrix of the whole structure of infinite fractal order A_∞ can be calculated recursively due to the self-repeating property of the fractal:

$$A_\infty(k_0, L, \varepsilon_1, \varepsilon_2) = B_\infty \cdot A_{\text{diel}}(k_0, d_1, \varepsilon_1) \cdot B_\infty, \tag{2.7}$$

where B_∞ is the transfer matrix of the two fractal parts which surround the middle dielectric layer of thickness $d_1 = (1 - 2r)L$. By using fractal's self-similarity property, B_∞ can be expressed as

$$B_\infty = A_\infty(k_0, r^2L, \varepsilon_1, \varepsilon_2) \cdot A_{\text{diel}}(k_0, rd_1, \varepsilon_2) \cdot A_\infty(k_0, r^2L, \varepsilon_1, \varepsilon_2). \tag{2.8}$$

The equations 2.7 and 2.8 are functional equations for the unknowns A_∞ and B_∞. Resolving these equations analytically for arbitrary values of the parameters appears impossible. However, when interested only in the behaviour of the structure at low frequencies, the following method can be used. The same approach also allows us to find the effective permittivities of the structure at low frequencies.

In order to solve Eqs. 2.7 and 2.8 with the effective medium approach, we equate the unknown transfer matrices A_∞ and B_∞ to the transfer matrices of uniform dielectric layers with some effective permittivities $\varepsilon_{A,\text{eff}}$ and $\varepsilon_{B,\text{eff}}$: $A_\infty = A_{\text{diel}}(k_0, L, \varepsilon_{A,\text{eff}})$ and $B_\infty = A_{\text{diel}}(k_0, rL, \varepsilon_{B,\text{eff}})$,

and search for such $\varepsilon_{A,\text{eff}}$ and $\varepsilon_{B,\text{eff}}$ which satisfy the equations 2.7 and 2.8. In the quasi-static limit of $k_0 L\sqrt{\epsilon_r} \ll 1$ the expression for the transfer matrix of the dielectric layer can be approximated as:

$$A_{\text{diel}}(k_0, d, \varepsilon) = \begin{pmatrix} 1 - \frac{\varepsilon}{2}(k_0 d)^2 & -ik_0 d \\ -i\varepsilon k_0 d & 1 - \frac{\varepsilon}{2}(k_0 d)^2 \end{pmatrix} + O\left((k_0 d)^3\right). \tag{2.9}$$

Using this expression for A_∞ and B_∞, we solve the system of equations (Eq. 2.7 and 2.8), which follows from the self-similarity property of the fractal:

$$\begin{aligned} A(k_0, L) &= B(k_0, rL) \cdot A_{\text{diel}}(k_0, d_1, \varepsilon_1) \cdot B(k_0, rL), \\ B(k_0, rL) &= A(k_0, r^2 L) \cdot A_{\text{diel}}(k_0, d_2, \varepsilon_2) \cdot A(k_0, r^2 L). \end{aligned} \tag{2.10}$$

The solution of this system of equations is:

$$\varepsilon_{A,\text{eff}} = \frac{\varepsilon_1 + 2\varepsilon_2 r}{1 + 2r}, \tag{2.11}$$

$$\varepsilon_{B,\text{eff}} = \frac{\varepsilon_2 + 2\varepsilon_1 r}{1 + 2r}, \tag{2.12}$$

where, $\varepsilon_{A,\text{eff}} \equiv \varepsilon_{\text{eff}}$ is the effective epsilon of the whole fractal. Note that, in the quasi-static limit, the effective permittivity of the structure is expressed as a weighted average of the permittivities of the layers.

In order to understand the range of applicability of the obtained quasi-static expressions for the effective permittivity, we compare the eigenvalues of the total transfer matrices calculated by the effective medium approach and by the multilayer approach.

The transfer matrix eigenvalues for both the effective medium approach and the direct numerical calculation for multiple layers are shown in Fig. 2.4. This figure depicts the real part and the absolute value of the imaginary part of the two eigenvalues as functions of $k_0 L$. The curves representing these functions (the blue and golden curves) coincide within the propagation bands and split (form "loops" visible in Fig. 2.4) in the stopbands. Fig. 2.4 shows that outside of the stopbands and when $k_0 L \lesssim 2$, the result from the effective medium calculations is similar to the result from numerical calculations for 9th order.

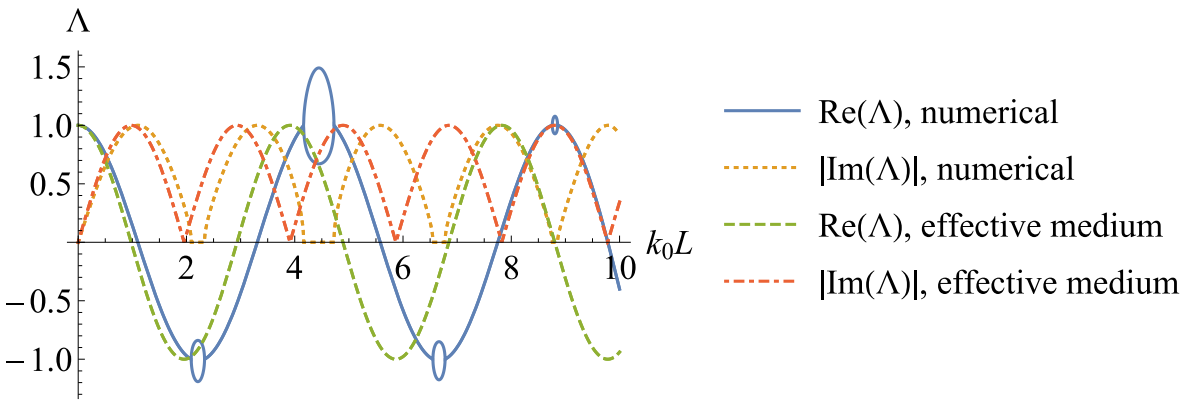

FIGURE 2.4: The imaginary and real parts of eigenvalues obtained from numerical results and effective medium calculations for the 9th order fractal MM.

2.1.3 FDTD Simulations

In order to verify the analytical results obtained with the transfer matrix approach, MIT Photonic-Bands (MPB)[1] package and MIT Electromagnetic Equation Propagation (MEEP)[2] simulation software package have been used [72].

In contrast with the transfer-matrix based calculations, in which considering structures that have thousands of dielectric layers is feasible, in FDTD[3]-based numerical calculations working with higher orders of fractals is more difficult. Therefore, the following results are given only for 9th and 11th order fractal MMs which have 683 and 2731 dielectric layers in the whole structure, respectively. Fig. 2.5 shows the ε profile of the fractal of 9th order.

2.1.3.1 FDTD-Based Band Diagram Calculations

Fig. 2.6.a depicts the permittivity profile of the 9th order fractal MM as it is represented by the MPB. With increasing the resolution of the figure the distribution of ε is better seen for higher orders.

[1]The MIT Photonic-Bands (MPB) package is a free program for computing the band structures (dispersion relations) and electromagnetic modes of periodic dielectric structures.

[2]The MIT Electromagnetic Equation Propagation (MEEP) is a free finite-difference time-domain (FDTD) simulation software package developed at MIT to model electromagnetic systems, along with MPB eigenmode package.

[3]FDTD is one of the approximation methods to solve differential equations in computational electromagnetics. Being a time-domain techniques allows wide frequency coverage with each simulation. In order to solve a problem with this method, we need to write partial differential Maxwell's equations in time dependent discrete form. The system of obtained equations should be solved in leapfrog manner until it reaches the steady-state behaviour.

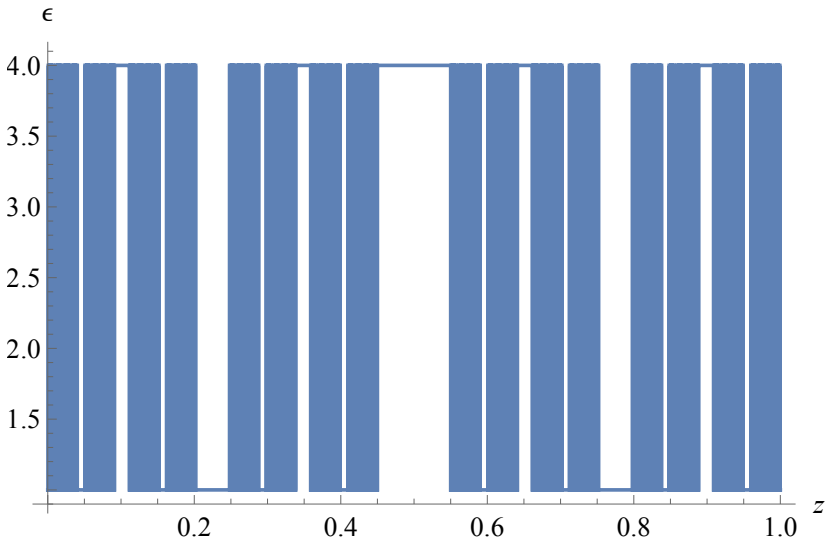

FIGURE 2.5: ε profile for the 9th order fractal MM. Due to the limited resolution of the figure, the very thin dielectric layers located in the coloured regions are not seen.

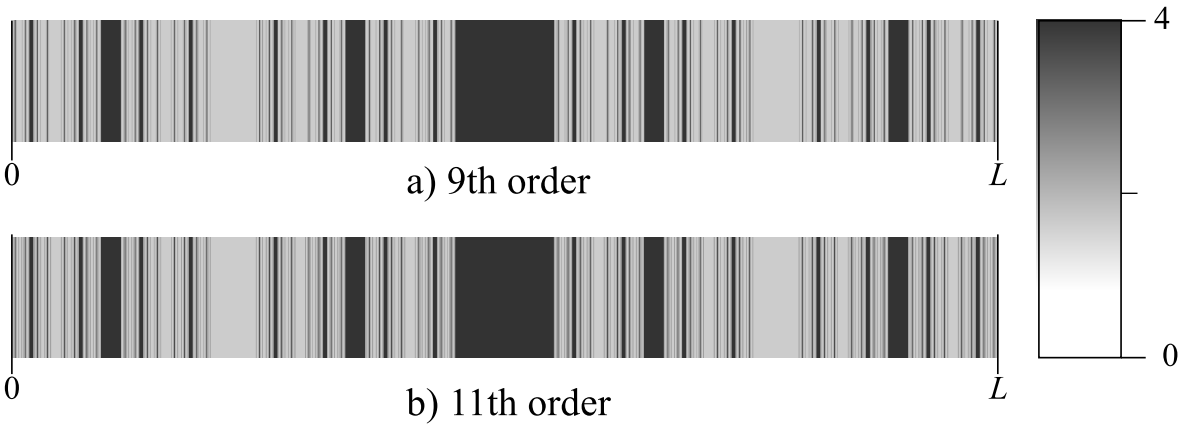

FIGURE 2.6: ε profile for the 9th and 11th order fractal MM by MPB. The black and gray color are ε_1 and ε_2 respectively.

The number of layers in each order of this structure is $\frac{1}{3}(2^{n+2} - (-1)^n)$. The smallest layer thickness equals to Lr^n for $\frac{1}{3} < r < \frac{1}{2}$, and $L(1-2r)r^{n-1}$ for $r < \frac{1}{3}$. Considering these conditions, the physical limits for the highest order of this structure can be estimated.

Fig. 2.7 shows the band diagram for the 9th and 11th orders (the epsilon profile of this order is shown in Fig. 2.6.b) of fractal MM. As is seen from the band diagram for the 9th order, the simulation results follow closely the analytical results shown in Fig. 2.3.

As it is seen from Fig. 2.7, since the finest fractal elements are already too small in these orders (as compared to wavelength), the band diagrams are very close to each other.

Fig. 2.8 shows the agreement between analytical results and numerical calculations for the fractal of 9th order.

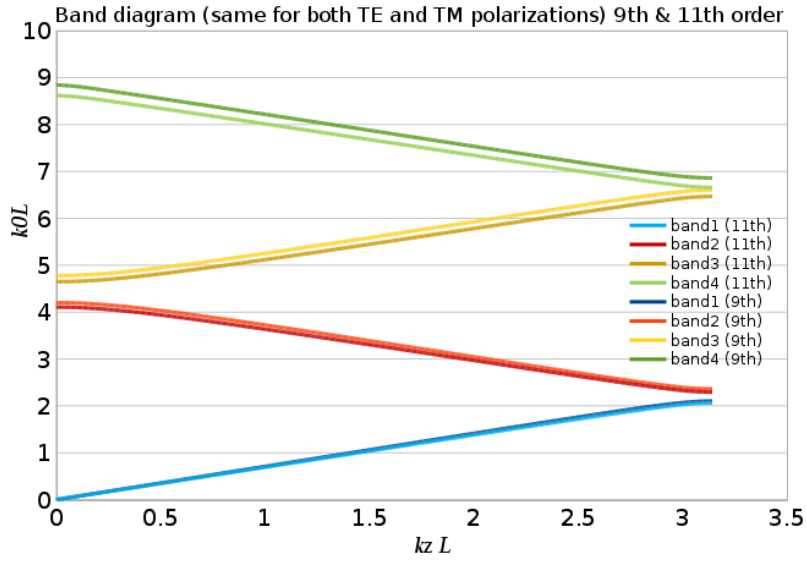

FIGURE 2.7: Band diagrams for 9th and 11th order by MPB.

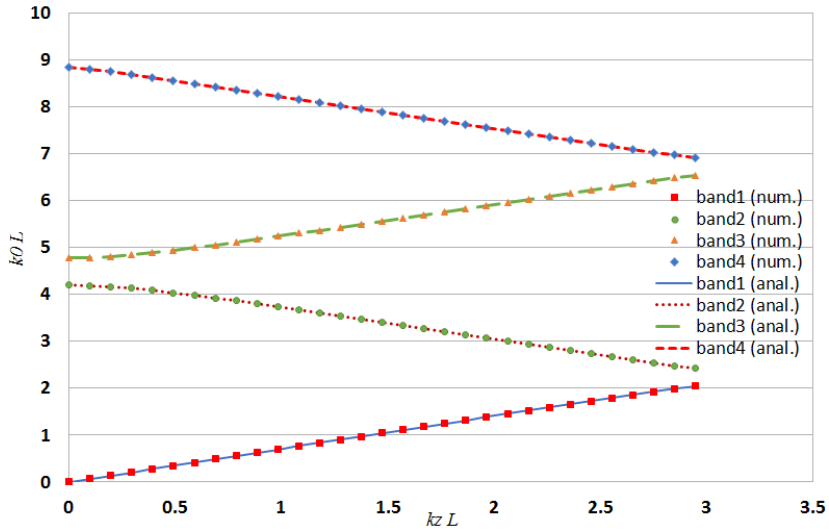

FIGURE 2.8: Comparison between band diagrams from analytical and numerical calculation for a 9th order fractal MM.

2.1.3.2 Field Distributions in the Propagation Bands

Using the FDTD algorithm allows us also to study how the electromagnetic field of the modes propagating inside the structure is distributed within the multilayer structure.

The field distribution along the fractal structure is shown in Fig. 2.9, for four bands of propagation. In these examples, $k_z L = \frac{\pi}{2}$. As one can see, the field distributions closely resemble the ones for plane waves propagating in uniform media, which shows that the studied fractal structure can be considered as effectively homogeneous in these frequency bands.

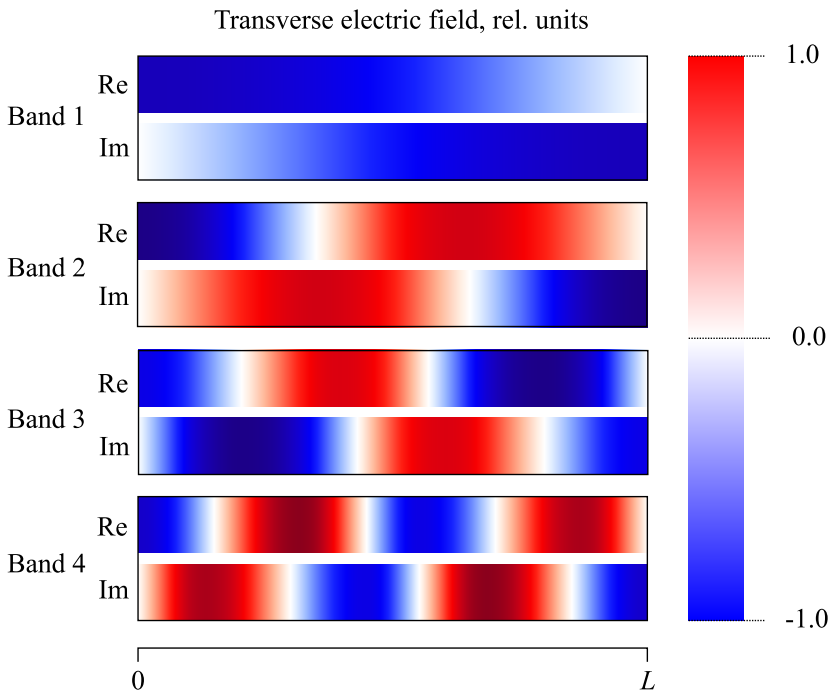

FIGURE 2.9: Distribution of the transverse electric field (real and imaginary parts) inside the fractal structure for different propagation bands (in units relative to the field maximum).

2.2 Homogenization in Spatially Dispersive Case

Constitutive relations for a wide class of materials — including MMs — can be represented[73] as in Eq. (2.13):

$$\begin{pmatrix} \vec{D}(\omega,\vec{k}) \\ \vec{B}(\omega,\vec{k}) \end{pmatrix} = \begin{pmatrix} \overline{\overline{\varepsilon}}(\omega,\vec{k}) & \overline{\overline{\xi}}(\omega,\vec{k}) \\ \overline{\overline{\zeta}}(\omega,\vec{k}) & \overline{\overline{\mu}}(\omega,\vec{k}) \end{pmatrix} \cdot \begin{pmatrix} \vec{E}(\omega,\vec{k}) \\ \vec{H}(\omega,\vec{k}) \end{pmatrix}, \tag{2.13}$$

where $\vec{E}$ and $\vec{H}$ are electric and magnetic fields and $\vec{D}$ and $\vec{B}$ are electric displacement and magnetic induction, respectively. The material parameters in Eq. (2.13) are the dyadics of permittivity $\overline{\overline{\varepsilon}}$ and permeability $\overline{\overline{\mu}}$, and the magnetoelectric coupling dyadics $\overline{\overline{\xi}}$ and $\overline{\overline{\zeta}}$. In reciprocal media [4], $\overline{\overline{\xi}} = -\overline{\overline{\zeta}}^{T}$ [73].

In our case, because we consider a MM formed by reciprocal dielectric (nonmagnetic) layers we may assign $\overline{\overline{\mu}} = \mu_0 \overline{\overline{I}}$ (here, $\overline{\overline{I}}$ is the unity dyadic). In addition, the symmetry of our structure and of its excitation implies no magnetoelectric interaction effects and thus $\overline{\overline{\xi}} = -\overline{\overline{\zeta}}^{T} = 0$. Therefore, here we only calculate the effective permittivity dyadic of the structure as a function of the frequency and wave vector: $\overline{\overline{\varepsilon}}_{\text{eff}}(\omega,\vec{k})$. In this work, we consider that

[4] The reciprocal media here is the media such that the Lorentz reciprocity theorem holds.

$\vec{k}$ has just the z component: $\vec{k} = k_z\vec{z}_0$. Note that in Eq. (2.13) ω and $\vec{k}$ are considered as independent variables, so that the constitutive relations are valid also at the $(\omega, \vec{k})$ points which do not belong to any dispersion branch for the waves that may propagate in the structure. This is important when considering the electromagnetic response of a MM inside band gaps, or in cases when there is an external source embedded in the material.

Taking into account the above remarks, Eq. (2.13) can be simplified in our case as follows:

$$\vec{D}(\omega, k_z) = \overline{\overline{\varepsilon}}_{\text{eff}}(\omega, k_z)\vec{E}(\omega, k_z), \tag{2.14}$$

where,

$$\overline{\overline{\varepsilon}}_{\text{eff}}(\omega, k_z) = \varepsilon_0\overline{\overline{\varepsilon}}_{\text{r}}(\omega, k_z) = \varepsilon_0 \begin{pmatrix} \varepsilon_{xx} & \varepsilon_{xy} & \varepsilon_{xz} \\ \varepsilon_{yx} & \varepsilon_{yy} & \varepsilon_{yz} \\ \varepsilon_{zx} & \varepsilon_{zy} & \varepsilon_{zz} \end{pmatrix}. \tag{2.15}$$

Since the layered fractal structure we are considering is uniaxial (only one special direction exists — the z-axis direction), $\overline{\overline{\varepsilon}}_{\text{eff}}$ is a diagonal dyadic with $\varepsilon_{xx} = \varepsilon_{yy} \neq \varepsilon_{zz}$:

$$\overline{\overline{\varepsilon_{\text{r}}}}(\omega, k_z) = \begin{pmatrix} \varepsilon_{xx}(\omega, k_z) & 0 & 0 \\ 0 & \varepsilon_{xx}(\omega, k_z) & 0 \\ 0 & 0 & \varepsilon_{zz}(\omega, k_z) \end{pmatrix}. \tag{2.16}$$

In order to extract the effective dispersive permittivity $\overline{\overline{\varepsilon}}_{\text{eff}}(\omega, k_z)$ with the frequency ω and the wave number k_z, understood as independent variables, the structure is excited by an embedded source (App. B) $\vec{J}_{\text{ext}}(t, z) = \vec{J}_0 e^{-i\omega t} e^{ik_z z}$, which is a plane wave of distributed electric currents with independently set ω and k_z. We find the induced electromagnetic fields inside the structure either by using Finite-Difference Time-Domain (FDTD) technique (in numerical calculations) or solving Maxwell's equations directly (in analytical calculations). Since in the external source we can set ω and k_z independently (see more on this in App. B), we can expect that in steady state the fields induced by such source vary similarly within the structure with the same characterictic wavelength $\Lambda = \frac{2\pi}{k_z}$ and the same frequency ω. Thus, by applying an external source, we are able to study the electromagnetic response of the MM while k_z and ω are independent from each other. The same idea has been previously employed for homogenization of spatially-dispersive periodic media [33]. In a similar way, the

dispersion behaviour of our structure can be studied as a function of the frequency and the wavenumber.

Hence, we need to find the solution of the non-uniform Maxwell's equations within the region occupied by the structure when an embedded external source is applied to the structure:

$$\begin{aligned} \nabla \times \vec{E} &= -\mu_0 \frac{\partial \vec{H}}{\partial t}, \\ \nabla \times \vec{H} &= \varepsilon_0 \varepsilon_{\mathrm{r}}(z) \frac{\partial \vec{E}}{\partial t} + \vec{J}_{\mathrm{ext}}(t, z), \end{aligned} \tag{2.17}$$

where $\varepsilon_{\mathrm{r}}(z)$ is the dielectric permittivity profile (e.g. Fig. 2.5) in the structure which is assumed real valued and not dispersive. Since the external source and the induced fields vary only along the z-axis, we can equate $\nabla = \vec{z}_0(\frac{\partial}{\partial z})$. In order to extract the two independent components ε_{xx} and ε_{zz} of the effective permittivity dyadic (which is, in general, different from $\epsilon_r(z)$), the source current must have non-vanishing components along the x and z axes. Under these assumptions, $\vec{E} = \vec{x}_0 E_x + \vec{z}_0 E_z$ and $\vec{H} = \vec{y}_0 H_y$, and thus Maxwell's equations are reduced to

$$\frac{\partial E_x}{\partial z} = -\mu_0 \frac{\partial H_y}{\partial t}, \tag{2.18}$$

$$\frac{\partial H_y}{\partial z} = -\varepsilon_0 \varepsilon_{\mathrm{r}}(z) \frac{\partial E_x}{\partial t} - J_{x,\mathrm{ext}}(t, z), \tag{2.19}$$

$$\varepsilon_0 \varepsilon_{\mathrm{r}}(z) \frac{\partial E_z}{\partial t} = -J_{z,\mathrm{ext}}. \tag{2.20}$$

In order to have a unique solution, we must also define the boundary conditions (BC) at the edges of the fractal cell and an initial condition at $t = 0$. As the BCs must be compatible with the variation of the source currents, we use the Bloch-periodic BCs of the form

$$\begin{aligned} E_{x,z}\big|_{z=L} &= E_{x,z}\big|_{z=0} e^{ik_z L}, \\ H_y\big|_{z=L} &= H_y\big|_{z=0} e^{ik_z L}. \end{aligned} \tag{2.21}$$

Because these relations involve complex values (and also because the external source is complex-valued) in numerical calculations we have to use an FDTD implementation which allows for complex values of the time-domain fields. Fortunately, MEEP can work with complex-valued fields and sources in the time domain [72].

The initial condition at $t = 0$ can be set as $\vec{E}_x = \vec{H}_y = 0$ everywhere in the structure. MEEP's FDTD implementation also allows us to specify a gradual turn on of the sources, so that the currents do not change abruptly at $t = 0$, but, instead, approach the steady-state amplitude smoothly during a specified period of time. This reduces inaccuracies in the numerical extraction algorithm.

After finding the field values at different points inside the structure (the "microscopic" fields), we find the average ("macroscopic") electric field $\vec{E}_{\text{av}}(\omega, k_z)$ and the electric displacement $\vec{D}_{\text{av}}(\omega, k_z)$ as follows:

$$\begin{aligned} \vec{E}_{\text{av}}(\omega, k_z) &= \frac{1}{TL} \int_0^L \int_0^T \vec{E}(t, z) e^{i\omega t} e^{-ik_z z}\, dt\, dz, \\ \varepsilon_0^{-1} \vec{D}_{\text{av}}(\omega, k_z) &= \frac{1}{TL} \int_0^L \int_0^T \varepsilon_{\text{r}}(z) \vec{E}(t, z) e^{i\omega t} e^{-ik_z z}\, dt\, dz, \end{aligned} \tag{2.22}$$

where in these Fourier transforms $T \gg \frac{2\pi}{\omega}$ (ideally, $T \to \infty$). The final result for the effective permittivity components ε_{xx} and ε_{zz} can be obtained by using the following expressions:

$$\varepsilon_{xx}(\omega, k_z) = \left. \frac{\varepsilon_0^{-1} D_{x,\text{av}}(\omega, k_z)}{E_{x,\text{av}}(\omega, k_z)} \right|_{\vec{J}_0 = J_{0,x}\vec{x}_0}, \tag{2.23}$$

$$\varepsilon_{zz}(\omega, k_z) = \left. \frac{\varepsilon_0^{-1} D_{z,\text{av}}(\omega, k_z)}{E_{z,\text{av}}(\omega, k_z)} \right|_{\vec{J}_0 = J_{0,z}\vec{z}_0}. \tag{2.24}$$

When extracting ε_{xx}, the source current is directed along the x-axis (the other two components are zeros), and when extracting ε_{zz}, the source current is set up along the z-axis.

2.2.1 Analytical Calculations

The analytical calculations are done by solving the non-uniform Maxwell's equations (Eq. 2.17). In these equations we replace $\frac{\partial}{\partial t} \mapsto -i\omega$ and solve the resulting system in each case with the appropriate embedded source. The time harmonic dependency $e^{-i\omega t}$ is omitted in this section for the sake of brevity.

2.2.1.1 Calculation of ε_{zz}

In order to derive ε_{zz}, the source current is set up along the z-axis: $J_z(z) = J_{0,z}e^{ik_z z}$. Since there are no variations of current along x and y axes $\vec{H} = 0$ and Maxwell's equations are reduced to Eq. (2.20). By solving this equation, we obtain the following relations for the electric field and electric displacement:

$$E_z = -\frac{iJ_{0,z}}{\omega\varepsilon_{zz}(z)}e^{ik_z z}, \tag{2.25}$$

$$D_z = -\frac{iJ_{0,z}}{\omega}e^{ik_z z}. \tag{2.26}$$

The averaged electric field and displacement can be calculated using Eq. (2.22). Since the distribution of ε_{r} among the fractal layers depends on the parity of n, the averaged electric field also depends on the same condition:

$$\begin{aligned} \text{If n is even: } E_{z,av} &= -\frac{iJ_{0,z}}{\omega}\left(\frac{1+(2r)^{n+1}}{\varepsilon_1(1+2r)} + \frac{2r(1-(2r)^n)}{\varepsilon_2(1+2r)}\right), \\ \text{If n is odd: } E_{z,av} &= -\frac{iJ_{0,z}}{\omega}\left(\frac{1-(2r^{n+1})}{\varepsilon_1(1+2r)} + \frac{2r(1+(2r)^n)}{\varepsilon_2(1+2r)}\right), \end{aligned} \tag{2.27}$$

$$D_{z,v} = -\frac{iJ_{0,z}}{\omega}. \tag{2.28}$$

The epsilon in this case now can be obtained using Eq. (2.24):

$$\begin{aligned} \text{If n is even: } \varepsilon_{zz} &= \left(\frac{1+(2r)^{n+1}}{\varepsilon_1(1+2r)} + \frac{2r(1-(2r)^n)}{\varepsilon_2(1+2r)}\right)^{-1}, \\ \text{If n is odd: } \varepsilon_{zz} &= \left(\frac{1-(2r^{n+1})}{\varepsilon_1(1+2r)} + \frac{2r(1+(2r)^n)}{\varepsilon_2(1+2r)}\right)^{-1}. \end{aligned} \tag{2.29}$$

2.2.1.2 Calculation of ε_{xx}

In the case of ε_{xx}, we solve the system of two differential equations, namely, Eqs. (2.18) and (2.19), written for a single dielectric layer with uniform permittivity $\varepsilon_{\mathrm{r},xx}$ and an embedded current source. The layer is located at $z_1 < z < z_2$. The embedded source current is along x-axis: $J_x(z) = J_{0,x}e^{ik_z z}$. The differential equations are solved by the method of

variation of parameters, with which we find the following general solutions for E_x and H_y:

$$\begin{aligned} E_x(z) &= C_1\cos(kz) + C_2\sin(kz) \\ &\quad - \frac{ik_0\eta_0}{k}\Big(\sin(kz)\int\cos(kz)J_x(z)dz - \cos(kz)\int\sin(kz)J_x(z)dz\Big), \qquad (2.30) \\ H_y(z) &= \frac{i}{k_0\eta_0}\left(C_1 k\sin(kz) - C_2 k\cos(kz)\right) \\ &\quad - \Big(\cos(kz)\int\cos(kz)J_x(z)dz + \sin(kz)\int\sin(kz)J_x(z)dz\Big), \qquad (2.31) \end{aligned}$$

where $k = k_0\sqrt{\varepsilon_{\mathrm{r},xx}}$, $k_0 = \omega\sqrt{\varepsilon_0\mu_0}$, and $\eta_0 = \sqrt{\frac{\mu_0}{\varepsilon_0}}$.

To find the C_1 and C_2 parameters in these equations, we express them through the electric and magnetic fields at the point $z = z_2$ (one of layer's boundaries) with known electric and magnetic field values. From here, the values for C_1 and C_2 are:

$$\begin{aligned} C_1 &= -\frac{i\eta_0 k_0}{k}\sin(kz_2)H_y(z_2) + \cos(kz_2)E_x(z_2) - \frac{i\eta_0 k_0}{k}\int J_x(z)\sin(kz)dz\Big|_{z=z_2}, \\ C_2 &= \frac{i\eta_0 k_0}{k}\cos(kz_2)H_y(z_2) + \sin(kz_2)E_x(z_2) + \frac{i\eta_0 k_0}{k}\int J_x(z)\cos(kz)dz\Big|_{z=z_2}. \qquad (2.32) \end{aligned}$$

By substituting Eq. (2.32) into Eq. (2.31) and representing the result in a matrix form, we obtain the following matrix relation:

$$\begin{aligned} \begin{pmatrix} E_x(z) \\ H_y(z) \end{pmatrix} &= \begin{pmatrix} \cos(k(z_2-z)) & -i\eta\sin(k(z_2-z)) \\ -\frac{i}{\eta}\sin(k(z_2-z)) & \cos(k(z_2-z)) \end{pmatrix} \cdot \begin{pmatrix} E_x(z_2) \\ H_y(z_2) \end{pmatrix} \qquad (2.33) \\ &\quad + \begin{pmatrix} \frac{\eta J_{0,x}}{k_z^2-k^2}\Big(ike^{-ik_z z} + e^{-ik_z z_2}\big(k_z\sin(k(z_2-z)) - ik\cos(k(z_2-z))\big)\Big) \\ -\frac{J_{0,x}}{k_z^2-k^2}\Big(ik_z e^{-ik_z z} + e^{-ik_z z_2}\big(k\sin(k(z_2-z)) - ik_z\cos(k(z_2-z))\big)\Big) \end{pmatrix}, \end{aligned}$$

where $\eta = \frac{\eta_0}{\sqrt{\varepsilon_{\mathrm{r},xx}}}$.

Using the above formula, and the known fields values at the edge $z = \frac{L}{2}$ of the structure, fields values at any $-\frac{L}{2} \le z < \frac{L}{2}$ are:

$$\begin{pmatrix} E_x \\ H_y \end{pmatrix}_{z=z_{m,n}} = \prod_{i=1}^{m-1} A_{m-i,n} \cdot \begin{pmatrix} E_x \\ H_y \end{pmatrix}_{z=\frac{L}{2}} + \sum_{k=1}^{m-2} \prod_{i=1}^{k} A_{m-i,n} J_{m-k-1,n} + J_{m-1,n} \qquad m \in [1, 2^{n+1}], \tag{2.34}$$

where

$$z_{m,n} = \begin{cases} z_{\frac{m}{2}+1,n-1} + r^{n-1}(1-r)L & \text{if} \quad m = 4p-2, \quad p \in [1, 2^{n-2}], \\ z_{\frac{m+1}{4},n-1} + r^{n+1}L & \text{if} \quad m = 4p-1, \quad p \in [1, 2^{n-2}], \\ z_{\frac{m}{2},n-1} & \text{if} \quad m = 4p, \quad p \in [1, 2^{n-2}], \\ z_{\frac{m+1}{2},n-1} & \text{if} \quad m = 4p+1, \quad p \in [1, 2^{n-2}-1], \end{cases} \tag{2.35}$$

$$A_{l,n} = \begin{pmatrix} \cos k_0\sqrt{\varepsilon_{q,n}}(z_{l,n} - z_{l+1,n}) & -\frac{i\eta_0}{\sqrt{\varepsilon_{q,n}}} \sin k_0\sqrt{\varepsilon_{q,n}}(z_{l,n} - z_{l+1,n}) \\ -\frac{i\sqrt{\varepsilon_{q,n}}}{\eta_0} \sin k_0\sqrt{\varepsilon_{q,n}}(z_{l,n} - z_{l+1,n}) & \cos k_0\sqrt{\varepsilon_{q,n}}(z_{l,n} - z_{l+1,n}) \end{pmatrix}, \tag{2.36}$$

$$J_{l,n} = \frac{J_{0,x}}{k_z^2 - k_0^2\varepsilon_{q,n}} \begin{pmatrix} \frac{\eta_0}{\sqrt{\varepsilon_{q,n}}} \left(ik_0\sqrt{\varepsilon_{q,n}} e^{-ik_z z_{l+1,n}} + \right. \\ \left. - \left(ik_z e^{ik_z z_{l+1,n}} + \right. \right. \\ e^{-ik_z z_{l,n}} \left(k_z \sin k_0\sqrt{\varepsilon_{q,n}}(z_{l,n} - z_{l+1,n}) - ik_0\sqrt{\varepsilon_{q,n}} \cos k_0\sqrt{\varepsilon_{q,n}}(z_{l,n} - z_{l+1,n})\right)\right) \\ e^{-ik_z z_{l,n}} \left(k_0\sqrt{\varepsilon_{q,n}} \sin k_0\sqrt{\varepsilon_{q,n}}(z_{l,n} - z_{l+1,n}) - ik_z \cos k_0\sqrt{\varepsilon_{q,n}}(z_{l,n} - z_{l+1,n})\right) \end{pmatrix}, \tag{2.37}$$

where z is the coordinate of one of the boundaries of the fractal layers, m is the number of the boundary counting from the right edge ($z = \frac{L}{2}$) to the left, n is the order of the fractal, $l \in [1, m-1]$. The quantity $\varepsilon_{q,n}$ is the relative permittivity of the layer number q in the fractal of order n which can be determined using following conditions:

$$\begin{aligned} \varepsilon_{2^n,n} &= \varepsilon_1, \\ \varepsilon_{2^{2s_1}(2s_2+1),n} &= \left\{ \begin{array}{ll|l} \varepsilon_1 & \text{if } n : \text{even} & s_1 \in [0, \lfloor \frac{n-1}{2} \rfloor] \\ \varepsilon_2 & \text{if } n : \text{odd} & s_2 \in [0, 2^{n-2s_1+1} - 1] \end{array} \right., \\ \varepsilon_{2^{2s_3+1}(2s_4+1),n} &= \left\{ \begin{array}{ll|l} \varepsilon_1 & \text{if } n : \text{odd} & s_3 \in [0, \lceil \frac{n-1}{2} \rceil], \\ \varepsilon_2 & \text{if } n : \text{even} & s_4 \in [0, 2^{n-2s_3-2} - 1], \end{array} \right., \\ \varepsilon_{2^{n+1}-s_5,n} &= \varepsilon_{s_5,n}, \quad s_5 \in [1, 2^{n-1}]. \end{aligned} \tag{2.38}$$

The total number of layers in the fractal of order n is $2^{n+1} - 1$.

By applying the periodic boundary condition to the final result, we obtain the analytical expressions for E_x and H_y inside the whole fractal structure.

$$\begin{pmatrix} E_x \\ Hy \end{pmatrix}_{z=\frac{L}{2}} = \left(e^{-ik_z L} I - \prod_{i=1}^{2^{n+1}-1} A_{2^{n+1}-i,n} \right)^{-1} \cdot \left(\sum_{k=1}^{2^{n+1}-2} \prod_{i=1}^{k} A_{2^{n+1}-i,n} J_{2^{n+1}-k-1,n} + J_{2^{n+1}-1,n} \right), \tag{2.39}$$

where I is the unity matrix. Now this expression can be substituted into Eq. (2.23) and the effective epsilon is found from this formula and by that the homogenization problem is solved for this structure.

2.2.1.3 Extra recursive formulas related to the structure

If z is the coordinate of the boundaries of the fractal layers, m is the number of the boundary counting from the right to left, and n is the order of the fractal:

$$z_{m,n+1} = \begin{cases} z_{\frac{m}{2}+1,n} + r^n(1-r)L, & m = 4p-2, \text{ and } \quad p \in [1, 2^{n-1}], \\ z_{\frac{m+1}{4},n} + r^{n+1}L, & m = 4p-1, \text{ and } \quad p \in [1, 2^{n-1}], \\ z_{\frac{m}{2},n}, & m = 4p, \text{ and } \quad p \in [1, 2^{n-1}], \\ z_{\frac{m+1}{2},n}, & m = 4p+1, \text{ and } \quad p \in [1, 2^{n-1}-1]. \end{cases} \tag{2.40}$$

2.2.2 Numerical Results

We use FDTD to solve the Maxwell's equations with a source numerically in the case of ε_{xx}. In this work, MEEP has been used as an FDTD solver software to study the structure. In the FDTD algorithm we employed, the structure is excited by an external source in the form of a superposition of many plane waves with different values of k_z:

$$J_{x,\text{ext}}(t,z) = e^{-i\omega t} e^{ik_{z_0} z} \sum_{n=0}^{N} e^{in\Delta k_z z} = e^{-i\omega t} e^{ik_{z_0} z} \frac{1 - e^{i(N+1)\Delta k_z z}}{1 - e^{i\Delta k_z z}}. \tag{2.41}$$

Thus, in this expression, the k_z values start from $k_z = k_{z0}$ and continue increasing up to $k_z = k_{z0} + N\Delta k_z$ with the step Δk_z. This way in a single run of the FDTD algorithm we obtain a set of values of $\varepsilon_{xx}(\omega, k_z)$ at different k_z, as it will be explained later.

In order to be able to have a small value of the step Δk_z and at the same time keep the source variation compatible with the Bloch-periodic BCs at the edges of the structure, the unit cell in the FDTD simulation is formed by combining several fractal cells into a bigger supercell. If we select a smaller value for Δk_z, we need to combine more cells in order to have the desired accuracy in k_z. Namely, the number of fractal cells within the supercell can be calculated as

$$N_{\text{cells}} = \frac{2\pi}{\Delta k_z L}. \tag{2.42}$$

We use $\frac{L\Delta k_z}{2\pi} = \frac{1}{51}$ to run for fifty one wavenumber, and thus we combine $N_{\text{cells}} = 51$ fractal cells to form one supercell. The Bloch periodic BCs are applied at the edges of this supercell.

In the simulations we only have E_x and H_y components of the fields. We simulate the structure over a certain period of time and then sample the field values along the structure. Because the source is off at $t < 0$ and thus is not exactly a continuous wave, the sampling of the field should start only after a certain amount of simulation time passed which is defined in the program as delay start time.

By calculating the mean square variation (variance) of the field complex amplitude values sampled at successive moments of simulation time (Eq. (2.46)), we determine the moment when the simulation reaches the steady state. During the simulation, the variance of the samples is calculated iteratively.

$$\overline{X}_N = \frac{1}{\tilde{N}} \sum_{n=1}^{N} \alpha^{N-n} X_n; \tag{2.43}$$

$$\sigma^2 = \frac{1}{\tilde{N}} \sum_{n=1}^{N} \alpha^{N-n} (X_n - \overline{X}_N)^2, \tag{2.44}$$

where $\tilde{N} = \alpha^{N-1} + ... + \alpha^0 = \dfrac{1-\alpha^N}{1-\alpha}$. The above equations can be written in an iterative form:

$$\overline{X}_{N+1} = \frac{\alpha(1-\alpha^N)}{1-\alpha^{N+1}} \overline{X}_N + \frac{1-\alpha}{1-\alpha^{N+1}} X_{N+1}, \tag{2.45}$$

$$\sigma^2_{N+1} = \overline{X^2_{N+1}} - \overline{X}^2_{N+1}. \tag{2.46}$$

The Courant number[5] ($C = \frac{c\Delta t}{\Delta z}$) is equal to Meep default value and is 0.5 (which is lower than the maximum number ($C_{max,explicit} = 1$) we can choose for one-dimensional cases).

After the simulation reaches the steady state we calculate the Fourier-transforms (Eq.2.22) at each k_z value and obtain the averaged fields. Next the effective permittivity is calculated as explained in Sec. 2.2. The dependence of the effective permittivity on frequency in a wide range of $k_0 L$ parameter, for three selected values of the parameter $\frac{k_z L}{2\pi}$ is shown in Fig. 2.10.

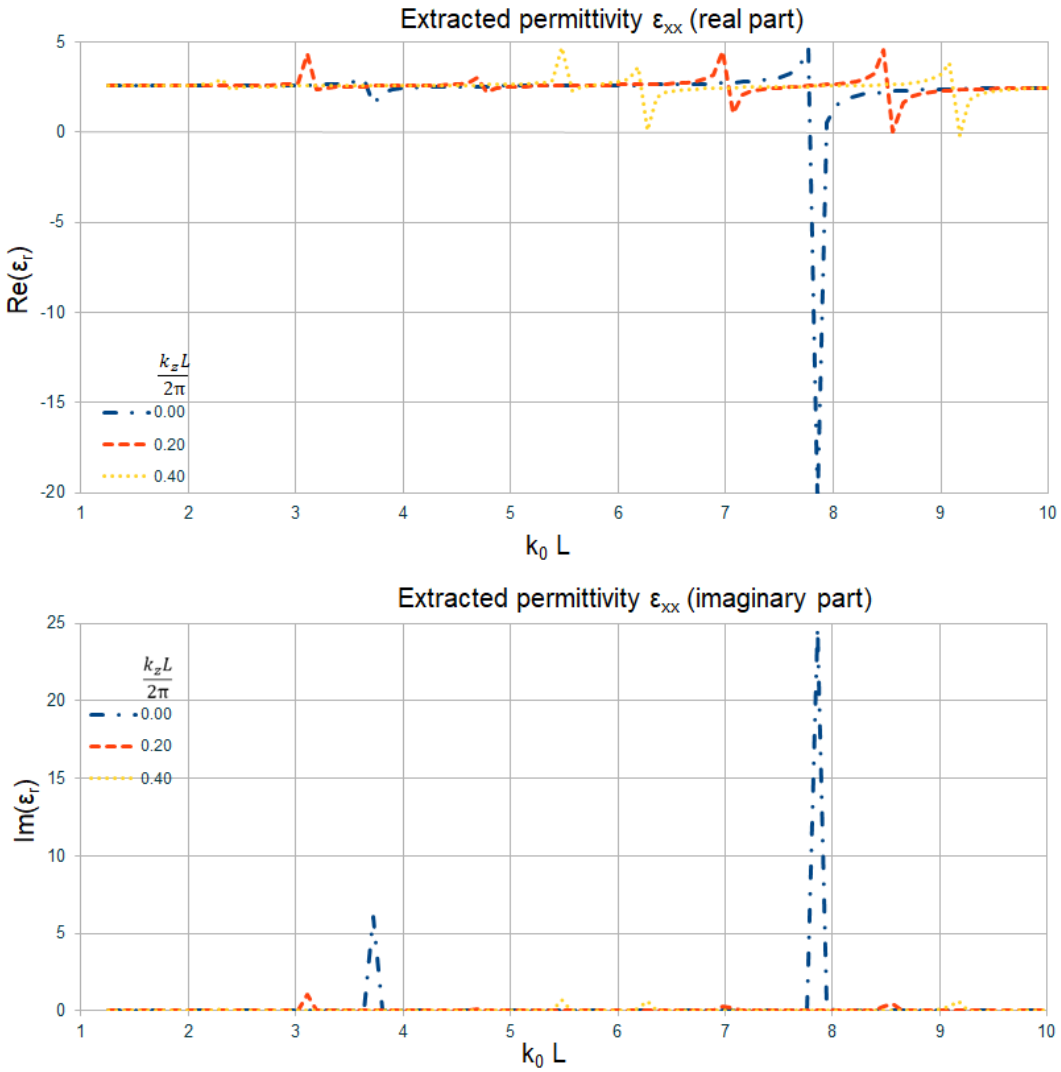

FIGURE 2.10: Real part and imaginary part of the extracted permittivity ε_{xx} as functions of $k_0 L$ for three different values of $\frac{k_z L}{2\pi}$ indicated in the plot.

The simulation has been also performed for more values of the normalized wavenumber $\frac{k_z L}{2\pi}$ ranging from zero to one, and the obtained results are presented in Fig. 2.11. From these results we may conclude that the effective permittivity of the structure depends on both

[5]This number is determined by Courant–Friedrichs–Lewy condition which is a necessary condition for convergence in solving partial differential equations in finite differences methods.

frequency and the wavenumber in a resonant manner. Moreover, for a fixed wavenumber value a few resonances can be identified from Fig. 2.11. The resonances observed at $\frac{k_z L}{2\pi} = 0.5$ correspond to the band gaps: in these regions the real part of the effective permittivity is negative which forbids propagation.

The curve with $\frac{k_z L}{2\pi} = 0$ at small values of the normalized frequency $\frac{k_0 L}{2\pi}$ corresponds to the quasistatic case discussed in Sec. 2.1 [63]. Using Eq. 2.12 in which the quasistatic limit for the effective permittivity ε_{xx} was found and for the parameters considered in this work ($\varepsilon_1 = 4$ and $\varepsilon_2 = 1$), we have $\varepsilon_{xx} \approx 2.58$. This result is in good agreement with the numerical simulations.

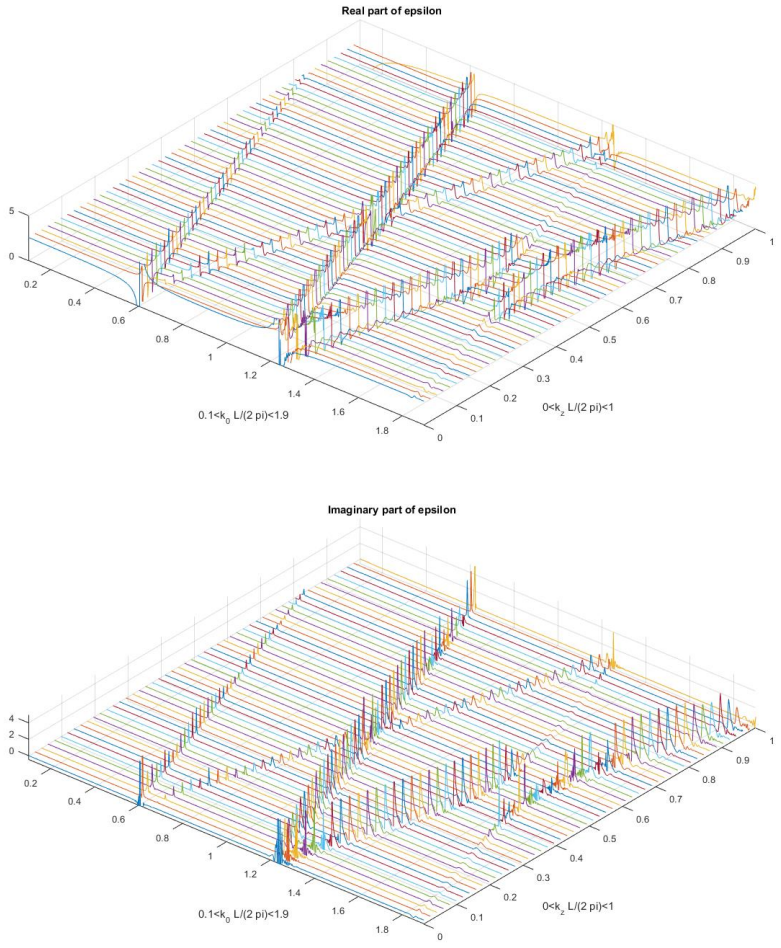

FIGURE 2.11: Real part and imaginary part of the extracted permittivity ε_{xx} as functions of the normalized frequency $\frac{k_0 L}{2\pi}$ and the normalized wavenumber $\frac{k_z L}{2\pi}$.

The resonance regions are more clearly presented in contour plots of ε_{xx} which are shown in Fig. 2.12. The dependence of the resonant frequency on k_z is better seen in this figure.

The simulation control file for this part is presented in App.C.

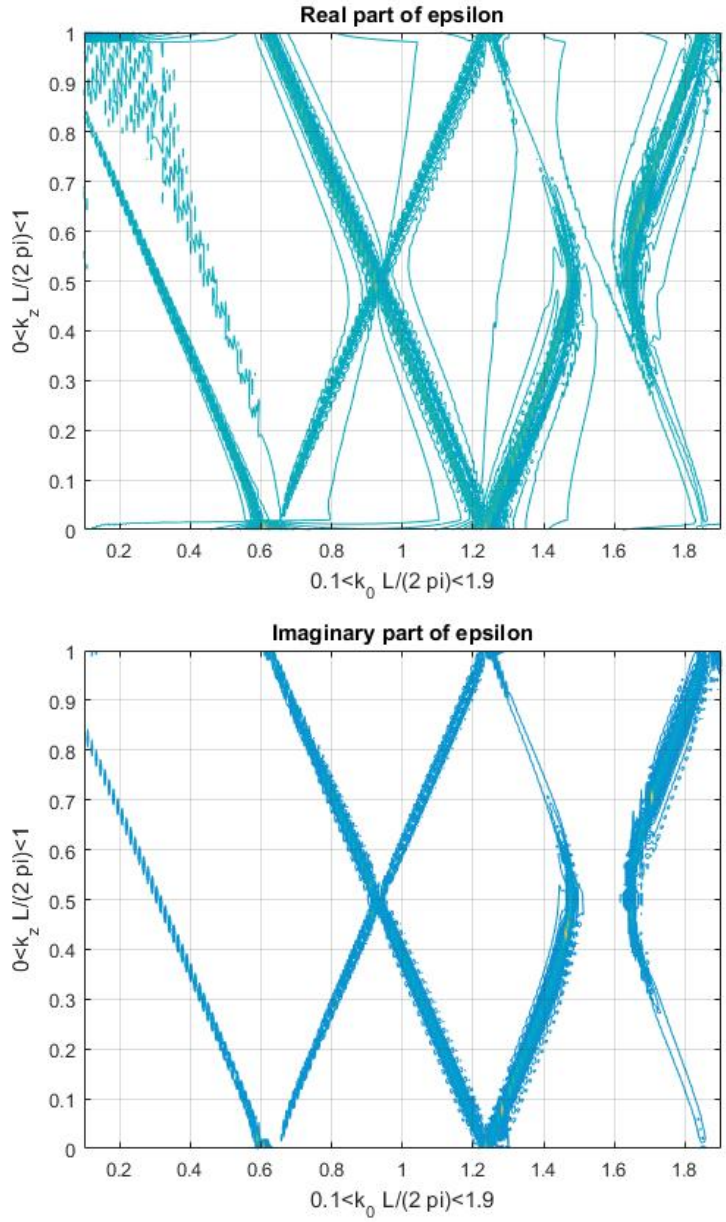

FIGURE 2.12: Contour plot of real part and imaginary part of the extracted permittivity ε_{xx} as functions of the normalized frequency $\frac{k_0 L}{2\pi}$ and the normalized wavenumber $\frac{k_z L}{2\pi}$.

2.3 Conclusion

In this chapter a new 1D MM which is based on a fractal set has been presented. In the first section, a homogenization method that uses self-similarity property of the structure has been developed. We have derived the effective material parameters of this fractal MM structure and verified them numerically. The quasi-static effective permittivity obtained with this method is expressed as a weighted average of permittivity of dielectric layers in the fractal. This

result agrees well with the known quasi-static solutions for layered media, which confirms the validity of the proposed homogenization method.

In the second section, a layered non-magnetic fractal MM has been considered. The effective material parameter dyadics have been derived (in this case we just have effective permittivity dyadic), both analytically and numerically.

Analytical expressions are obtained as the result of solving Maxwell's equations in each case. In order to do that, a number of recursive formulas are derived for the parameters of the fractal structure such as the coordinates of the boundaries for each layer in the structure, the transfer matrices for each layer and the total transfer matrix, including the terms due to the presence of the embedded external source, as it appears in the final result.

For the numerical calculations, MEEP was used as an FDTD solver and the obtained numerical results are presented. The obtained numerical results are in good agreement with the derived analytical formulas.

Chapter 3

2D MM based on Deterministic Fractal:

Metasurface based on Hilbert Curve

In this chapter, we develop a homogenization approach for a quasi-2D fractal-based MM (fractal-based metasurface [1]). As it was mentioned in the introduction, in order to homogenize a metasurface, one has to introduce effective electric and magnetic surface currents on the metasurface and find the relations between them and the applied electric and magnetic fields. The structure that we consider in this chapter is a quasi-periodic array of patches based on the Hilbert curve. The array can be placed above a metallic ground plane, be printed on a dielectric substrate, or it can be considered free-standing in air. In this study, we develop a theoretical model for the effective surface impedance of the structure by using the self-similarity of the fractal and the electromagnetic Babinet principle. We numerically simulate the reflection of the plane waves incident on such a metasurface (with the substrate plane included). The properties of the Hilbert fractal metasurface will be extracted from the data obtained in these simulations. Our aim is to find the effective parameters and construct an equivalent model for the fractal patches.

[1] 2D metamaterials are widely known as metasurfaces. Beside being a dimension reduction of MMs, metasurface also can be seen as a functional extensions of frequency selective surfaces [74]. Metasurfaces are lighter and less lossy (due to the volume reduction) as compared to MMs. And in comparison to FFSs, they are more flexible and have richer functionalities.

3.1 Introduction

Space-filling, self-similar curves were first introduced by Giuseppe Peano in 1890 [75]. The Peano curve is a surjective and continuous functional mapping of a unit interval onto the unit square. Due to this fact, the space-filling curves are mostly referred to as the Peano curves. However, the Peano curve is just one example from numerous other fractals with similar behaviours. David Hilbert among many others refined the curve in 1891 [60] and introduced a simpler algorithm to build a space-filling curve, known as the Hilbert curve.

Following the technological advancement in the last century, new requirements for the design of telecommunication devices were introduced. The appearance of small-sized devices brought more attention to the advantages that space-filling curves could offer. Since then, there have been many studies that involve different aspects of the use of fractal structures, more specifically, the space-filling and self-repeating curves.

Application of Hilbert curve-based fractal MMs in antenna design results in reconfigurable and/or wideband properties, and helps in miniaturization. Some representative studies, among numerous others, can be found in Refs. [76–81]. Such fractal structures have been used in microwave filter design for size reduction and improving the quality factor [82, 83]. The peculiar properties of these fractal curves have been also used in the design of optical devices [84].

Following the successful application of the space-filling curves-based structures in antennas, there have been studies on the MMs that utilize the Hilbert curve in the electromagnetics and acoustics [85–89].

However, in regard to the electromagnetics of the fractal MMs based on the Hilbert curve, most of the known results are limited just to numerical simulations. In contrast, in this chapter we develop a semi-analytical model for the Hilbert-based metasurface.

3.2 Geometry of the Structure

The recursive procedure of the Hilbert curve construction (Fiq. 3.1) involves a “path” following these conditions [90]:

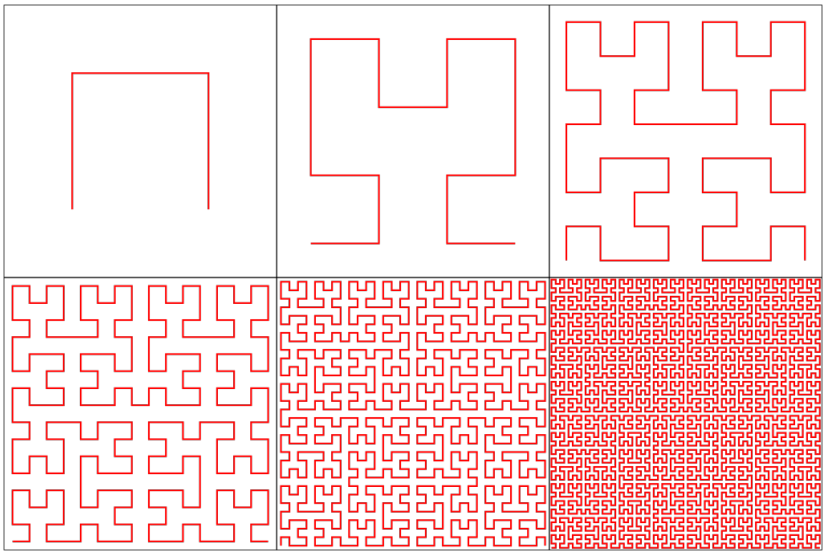

FIGURE 3.1: The first six orders of Hilbert curve.

- If in order n, we divide the square into 2^{n+1} equal size squares, the path should go through each square once,
- the path's starting point is through a definite neighbouring edge [2] of one of the corners,
- the path's final point is through the opposite edge of the first one and in the neighbourhood of the other corner (not diagonally-opposite),
- if you quarter an existing square, the rules should still be applicable.

The Hausdorff dimension of the Hilbert curve is 2 due to the space-filling property, while the Euclidean length of the path with the rules defined above is $2^n - \frac{1}{2^n}$. Although the length grows exponentially with the order n, the curve is always limited by the borders of the covering square.

In order to apply these rules in practice, instead of filling a fixed area with the ideal Hilbert curve of zero width, we fill the entire 2D plane with an approximation of the Hilbert curve formed by a finite-width metal strip, by following this rule: while following the Hilbert curve and advancing forward by a small fixed step dl, we attach a square patch of metallization with the dimensions $dl \times dl$ to the path, so that one of the sides of the square coincides with the path and the square's middle is always at the right-hand side with respect to the direction of path traversal. The first five iterations of this design are shown in Fig. 3.2.

[2] The edge of the original square.

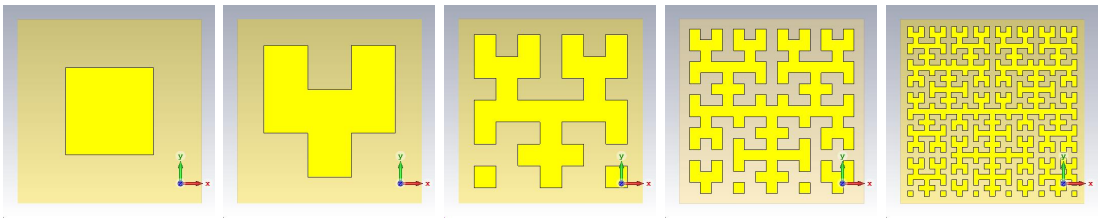

FIGURE 3.2: The first five iterations of Hilbert structure.

The resulting structure has recursive properties. If you divide the n-th order structure into four smaller equal size squares, the top squares are simply the $(n-1)$-th order and the bottom ones are the complementary structures of the $n-1$ order, where by the complementary structure we mean the one that can be obtained by replacing the metallized areas by the empty areas and vice versa. The smallest feature of this structure has the dimension of $dl_n = \frac{a}{2^{n-1}}$, where a is the size of the enclosing square (same as the unit cell is some designs). The number of filled squares is $2^{n-1}(2^n-1)$ where n is the order of the curve. The relative unit cell area coverage for the structure with order n is $\frac{2^{n-1}(2^n-1)}{2^{2n}}$. Therefore, when n tends to infinity, the area coverage tends to 0.5. Note that when dl is fixed and is the same for all orders, each fractal order iteration increases the area of the enclosing square by a factor of 2^2, so that the structure fills the 2D plane area rather quickly and essentially forms a fractal metasurface. In the following sections, we study the electromagnetic properties of such a metasurface.

3.3 Reflection Simulations

In order to extract the surface impedance data for the Hilbert curve-based metasurface, we first simulate the structure numerically within the CST Microwave Studio. In order to keep the overall size of the structure less than $\frac{\lambda}{2}$, which is necessary to be able to perform the simulations effectively in a wide frequency range in a single-mode waveguide, [3] in this example, we investigate just the first five iterations of the structure. In each order n, we slightly modify the original Hilbert curve-based structure of order n by adding a metallized strip of width $\frac{dl_n}{2}$ at the bottom of the structure. This is done in order to account for the electrical connection between the subareas of the order $n-1$ that compose the n-th order structure. This change to the fractal structure is shown in Fig. 3.3.

[3] Such PEC-PMC waveguide, due to reflections in its walls, effectively models a periodic array.

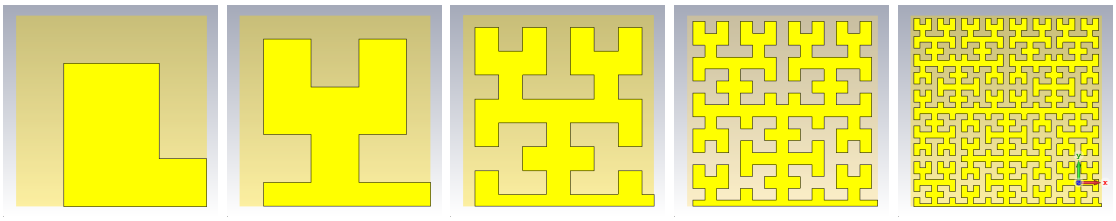

FIGURE 3.3: The first five iterations of fractal metasurface in x-y plane as fitting the same unit cell area.

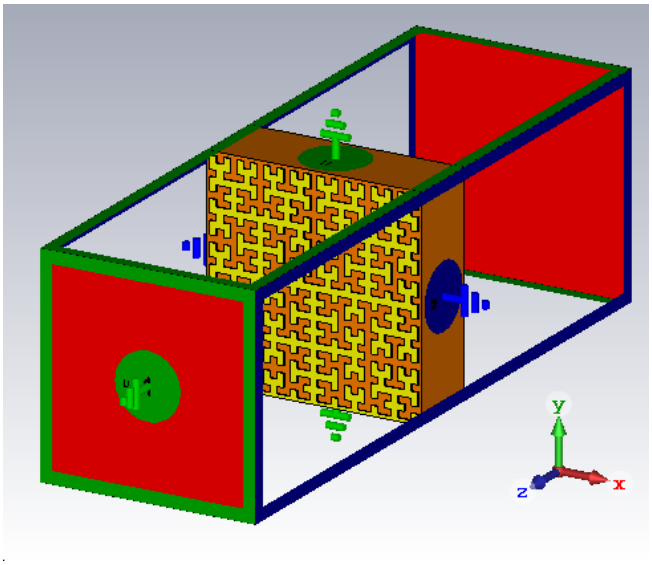

FIGURE 3.4: Port positions (red squares) and boundary conditions for the simulation of the 5th order fractal metasurface (the perfect electric conductor (PEC) walls are labelled with the green ground symbols and the perfect magnetic conductor (PMC) walls are labelled with the blue symbols).

The fractal structure on a dielectric substrate with the positions of the exciting ports and the boundary condition settings as modelled in CST are shown in Fig. 3.4.

The substrate in this example is Rogers RO3006 with the relative permittivity $\varepsilon_r = 6.15$ and the thickness $h = 1.28$ mm. The metallization thickness is $t = 0.017$ mm. The sizes of the substrate square in each order are as follows: 0.23 mm, 0.46 mm, 0.94 mm, 1.88 mm, 3.75 mm. The numerically simulated S-parameters (here, for the surface impedance extraction we just need the reflection from one side of the structure, for instance, S_{22}, for each order of the fractal) for each order are shown in Fig. 3.5.

It should be noted that for the normally incident plane wave with vertical polarization there is no cross-talk to the horizontal polarization, due to the symmetry of the structure. Then, from the reciprocity it follows also that there is no cross-polarized vertical component when the incident wave is horizontally polarized.

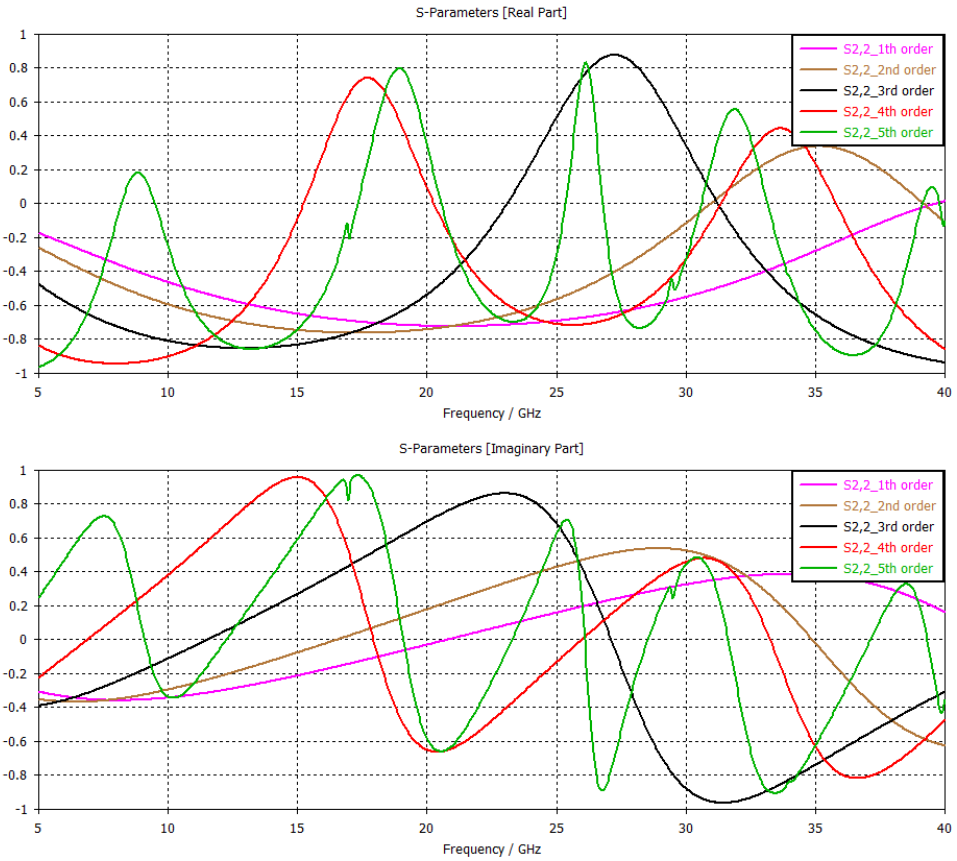

FIGURE 3.5: Top: the real part of S_{22}, Bottom: the imaginary part of S_{22}

3.4 Extraction of the Effective Impedance of the Metasurface

Knowing the obtained S-matrix parameters (we just need S_{22}) for the fractal metasurface and using the following equations, we extract the surface impedance of the fractal metasurface Z_s (in what follows, the time dependence is $\exp(j\omega t)$; where $j = \sqrt{-1}$):

$$Z_s = \frac{\eta_0 Z_l}{\eta_0 - Z_l}, \tag{3.1}$$

where $\eta_0 \approx 377$ Ohm is the vacuum impedance and Z_l is expressed as

$$Z_l = \eta \frac{Z_{in} - j\eta \tan(kh)}{\eta - jZ_{in} \tan(kh)}, \tag{3.2}$$

where $\eta = \frac{\eta_0}{\sqrt{\varepsilon_r}}$, ε_r is the substrate relative permittivity, h is the substrate thickness, $k = \frac{\omega}{c}\sqrt{\varepsilon_r}$, and

$$Z_{in} = \eta_0 \frac{1 + S_{22}}{1 - S_{22}}. \tag{3.3}$$

These equations are obtained by employing the transmission line analogy for the normal plane wave incidence on the structure. In this analogy, Z_{in} is the input impedance of the structure, as seen from the side of the dielectric substrate and Z_l is the total load impedance at the other side of the substrate, which is a parallel connection of Z_s and the free space impedance η_0.

After extracting the numerical data for the complex surface impedance, $Z_s = R_s + jX_s$, at a large number of frequency points (about 10^3) in the frequency interval of our interest, we apply the cubic spline interpolation for the real and imaginary parts of Z_s as functions of the frequency. This information is used next to construct an equivalent circuit model for the fractal metasurface.

3.5 Equivalent Circuit Model for the Fractal Metasurface

The Babinet's principle was formulated in 1800s by Jacques Babinet for optics and it describes a relation between the diffraction pattern of an opaque body with a hole and of the complementary body of the same size [91]. Although originally used in Fourier optics, the Babinet's principle can be modified in order to describe the Maxwellian electromagnetic phenomena as well.

In its application to the antenna design the Babinet-Booker's [92] principle states that

$$Z_s Z_s^{\text{comp}} = \frac{\eta^2}{4}, \tag{3.4}$$

where Z_s and Z_s^{comp} are the surface impedances of two mutually complementary structures rotated by 90 degrees with respect to each other (e.g., a metallic patch with arbitrary holes and its compliment with the metallized areas replaced by empty areas and vice-versa and rotated) and η is the intrinsic impedance of the surrounding medium.

Some extensions of this principle are known. In general, there are two classes of problems when it comes to the Babinet's principle application in electromagnetics. Either we are dealing with an array of metallic patches (or similar structures) in a uniform background medium, or such an array lays on the boundary between two different media (e.g., a dielectric substrate and air). In the case of uniform medium, the Booker's impedance relation can be derived by requiring the sum of the transmission matrices of the complementary structures

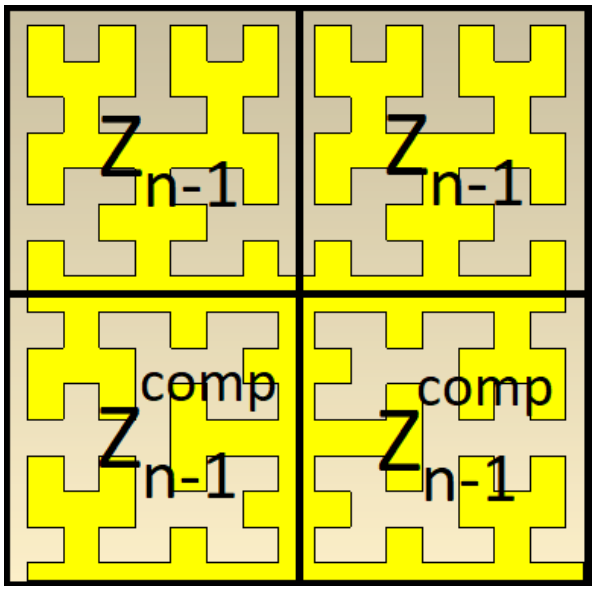

FIGURE 3.6: The relation between the n-th order metasurface and its parts of the order $n-1$ (the 4th order is shown here).

be equal to the unity matrix. In the case of non-uniform medium the fields need to be decomposed into non-coupling parts, while keeping in mind that the product of the effective surface inductance of one structure to the effective surface capacitance of the complementary structure is constant based on Babinet's principle [93].

As it was mentioned before, the Hilbert curve-based structure with order n can be decomposed into four patches of the order $n-1$ and their complements (Fig. 3.6).

From the Babinet-Booker's principle we may write first for the inductive and capacitive complementary screens in air

$$\text{if} \quad Z_s = \frac{1}{j\omega C_s}, \quad \text{then} \quad Z_s^{\text{comp}} = j\omega L_b, \tag{3.5}$$

and

$$\text{if} \quad Z_s = j\omega L_s, \quad \text{then} \quad Z_s^{\text{comp}} = \frac{1}{j\omega C_b}, \tag{3.6}$$

where $L_b = \frac{\eta_0^2 C_s}{4}$ and $C_b = \frac{4L_s}{\eta_0^2}$ are the quantities transformed in accordance with the Booker's impedance formula. In order to take into account the dielectric permittivity of the substrate in the quasi-static approximation, we have to multiply the free-space capacitance C_s by the factor $\frac{\varepsilon_r+1}{2}$, which is the average permittivity of the two materials on both sides of the metasurface. The inductance remains unmodified as we assume that the relative permeability of the substrate $\mu_r = 1$.

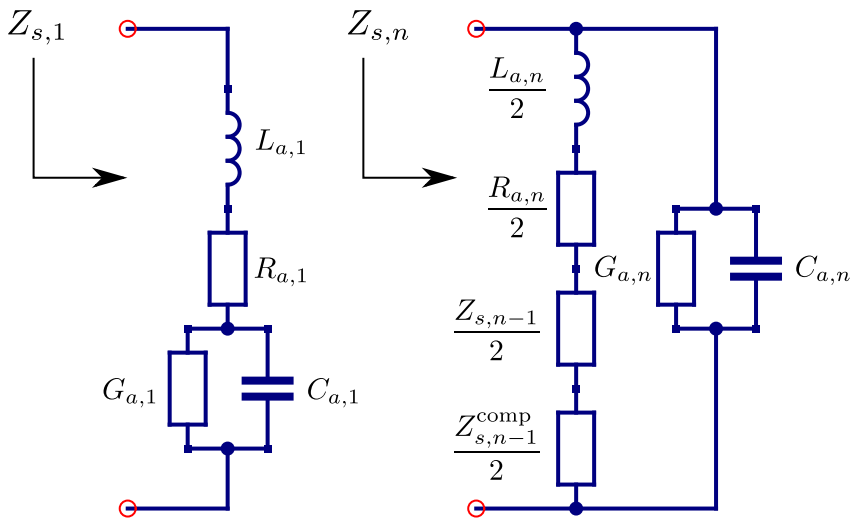

FIGURE 3.7: The equivalent circuit model for the effective surface impedance of the first (left) and n-th order (right) fractal metasurface.

Therefore, for a metasurface formed by a combination of the capacitive, $C_{a,i}$, and inductive, $L_{a,i}$, patches, we can derive the following relations for the corresponding parameters of the complementary structure, $C_{b,i}$ and $L_{b,i}$,

$$C_{b,i} = \frac{4L_{a,i}}{\eta_{\text{eff}}^2}, \tag{3.7}$$

$$L_{b,i} = \frac{\eta_{\text{eff}}^2 C_{a,i}}{4}, \tag{3.8}$$

where $\eta_{\text{eff}} = \eta_0\sqrt{\frac{2}{\varepsilon_r+1}}$.

Thus, we may construct the equivalent model for the surface impedance of the Hilbert curve-based metasurface as follows

$$Z_{s,1} = R_{a,1} + jL_{a,1}\omega + \frac{1}{G_{a,1} + j\omega C_{a,1}}, \tag{3.9}$$

$$Z_{s,n} = \frac{1}{G_{a,n} + j\omega C_{a,n} + \dfrac{2}{Z_{s,n-1} + Z^{\text{comp}}_{s,n-1} + R_{a,n} + j\omega L_{a,n}}}. \tag{3.10}$$

In this model, the effective impedance of the n-th order metasurface, $Z_{s,n}$, is expressed through the impedances of the $(n-1)$-th order of the same structure, $Z_{s,n-1}$, the impedances of their complements, $Z^{\text{comp}}_{s,n-1}$, and the free parameters $C_{a,n}$, $L_{a,n}$, $G_{a,n} \equiv \omega A_n$, and $R_{a,n}$, which account for the mutual coupling between the $(n-1)$-th order parts of the n-th order structure and the excess loss due to the distributed fields (Fig. 3.7). The motivation for this circuit model becomes apparent from Fig. 3.6.

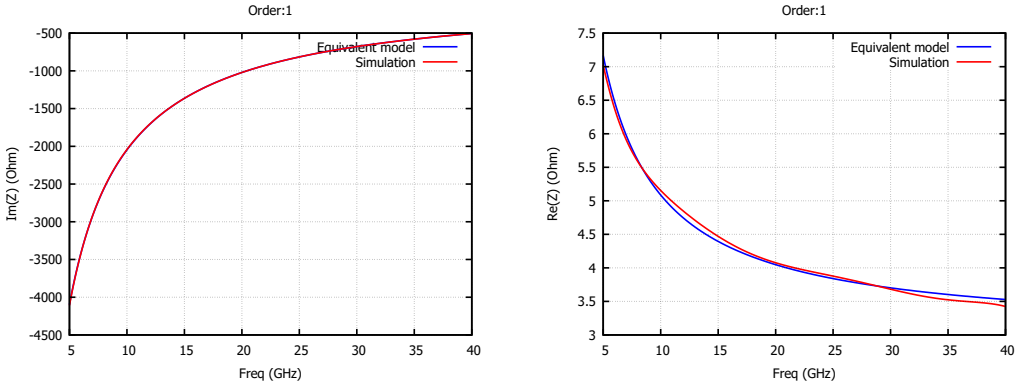

FIGURE 3.8: Imaginary and real part of the impedance Z_s obtained from the equivalent model vs. simulation results for the 1st order.

In order to find the values of the free parameters, we use the curve fitting approach with the following figure of merit (FOM) and the optimization algorithm LBFGS [4]:

$$\mathrm{FOM}(n, f_{min}, f_{max}, N) = \frac{1}{N}\sum_{k=0}^{N-1}\left[(\mathrm{Re}(Z_{s,n}(f_k)) - R_{s,n}(f_k))^2 + (\mathrm{Im}(Z_{s,n}(f_k)) - X_{s,n}(f_k))^2\right], \tag{3.11}$$

where $f_k = f_{min} + \frac{k}{N-1}(f_{max} - f_{min})$ and f_{min} and f_{max} define the frequency range in which the optimization algorithm is applied, n is the order of the fractal, and N is number of frequency samples. In this formula, $Z_{s,n}(f_k)$ is the value given by the circuit model at the frequency $f = f_k$ and $R_{s,n}(f_k)$, $X_{s,k}(f_k)$ are the interpolated values obtained from the CST simulations.

Figs. 3.8- 3.12 show the imaginary and real parts of the effective surface impedance obtained from the equivalent model in comparison to the simulation results. A very good agreement is obtained for the orders from 1 to 4 (the disagreements in the real parts are below 1 Ohm, while the absolute impedance values are on the order of hundreds of Ohm). The disagreement in the 5th order at frequencies higher than 20 GHz is due to the fact that the 5th order structure approaches the size of $\frac{\lambda}{4}$ at around 20 GHz, which is already too large for the quasi-static homogenization assumptions that we use.

Fig. 3.13 shows the obtained values for the equivalent model parameters for each order of the fractal metasurface. From this figure represented in double log scale one can notice the clear trend in the change of the parameters with increasing of n: All parameters (except the excess

[4]Limited-memory BFGS (LBFGS) is an optimization algorithm based on quasi-Newton methods that approximates the Broyden–Fletcher–Goldfarb–Shanno (BFGS) algorithm using a limited amount of computer memory. The Broyden–Fletcher–Goldfarb–Shanno (BFGS) algorithm is an iterative method for solving unconstrained nonlinear optimization problems.

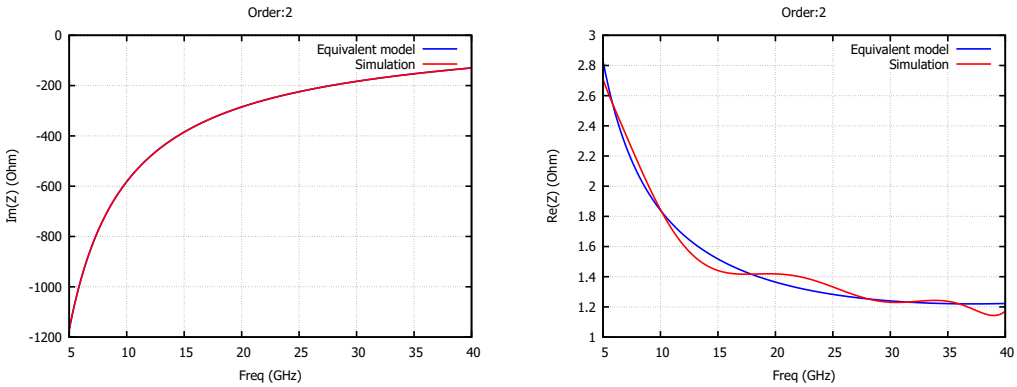

FIGURE 3.9: Imaginary and real part of the impedance Z_s obtained from the equivalent model vs. simulation results for the 2nd order.

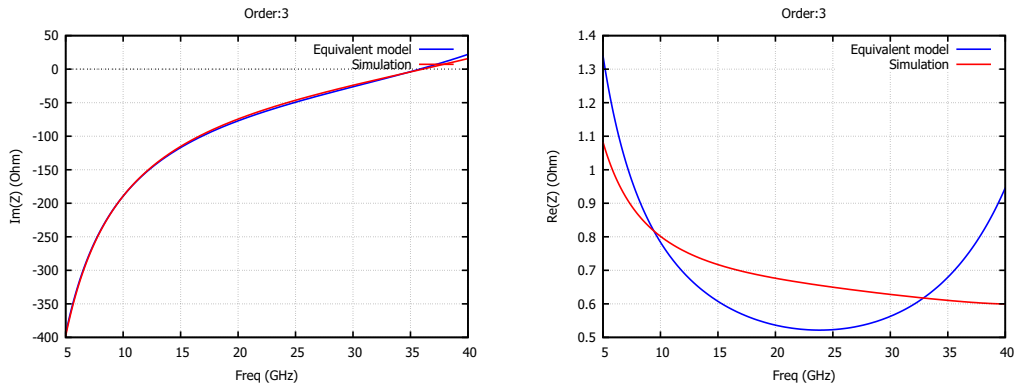

FIGURE 3.10: Imaginary and real part of the impedance Z_s obtained from the equivalent model vs. simulation results for the 3rd order.

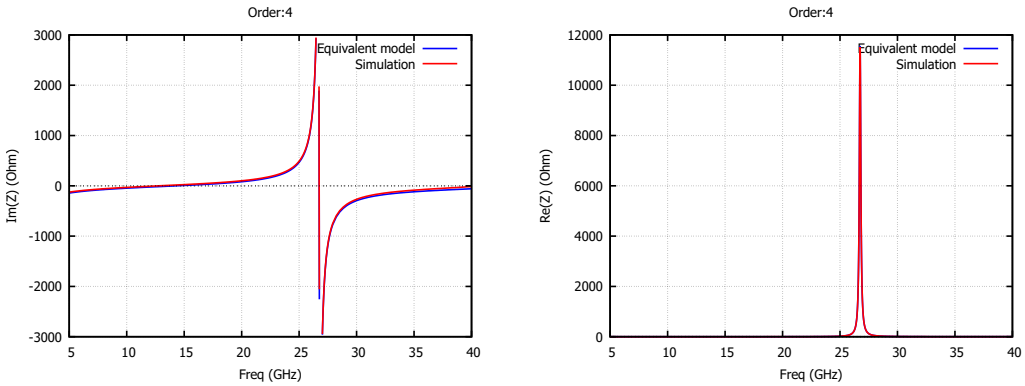

FIGURE 3.11: Imaginary and real part of the impedance Z_s obtained from the equivalent model vs. simulation results for the 4th order.

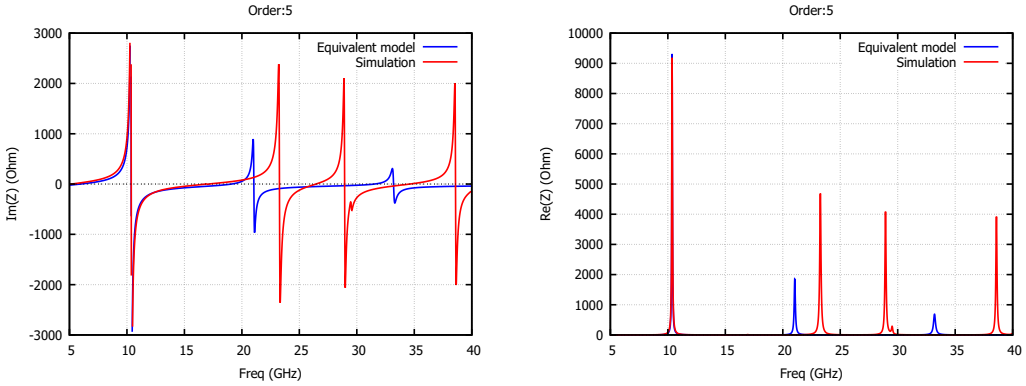

FIGURE 3.12: Imaginary and real part of the impedance Z_s obtained from the equivalent model vs. simulation results for the 5th order.

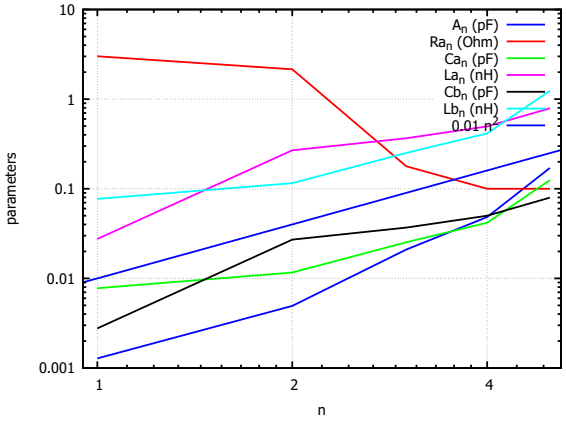

FIGURE 3.13: Obtained values for the equivalent model for each order of the fractal

metal loss parameter $R_{a,n}$ which decreases nonlinearly when n increases), vary approximately proportional to n^2, which is in perfect agreement with the fact that the Hilbert curve is a space-filling curve with the Hausdorff's dimension equal to 2.

3.6 Conclusion

In this chapter, we addressed the homogenization problem of the fractal Hilbert-curve based metasurface. By taking into account the self-similarity properties of the structure, we could obtain an equivalent model based on an extension of Babinet-Booker's principle for electromagnetics. The results of this model show very good agreement with the simulation results.

Chapter 4

3D MM based on Deterministic Geometrical Fractal:

Wire medium based on Sierpinski Carpet

In this chapter we implement the idea of fractal geometry in a three-dimensional MM formed by an array of parallel metallic cylinders – the wire medium (WM) [62]. This MM has a stop-band at frequencies below an effective plasma frequency which is determined by the radius of the cylinders and the structural period. In contrast to the standard periodic WM, now we distribute the positions of the cylinders and their radii over the cross-section of the structure by following the Sierpinski carpet fractal pattern. It is shown that a WM with a fractal structure can perform similarly to the regular WM while opening new possibilities to make the structure lighter and using less material. The proposed structure also offers better control over the selection of the frequency range.

4.1 Theory

A wire medium (WM) is a metamaterial characterized by negative effective permittivity below a certain threshold frequency, also known as the plasma frequency. A WM formed by a dense array of parallel metallic wires is a very common component in present day metamaterials.

For frequencies below the plasma frequency, the propagation of the electromagnetic waves whose electric field vector is parallel to the wires, is suppressed. Therefore, such waves are

totally reflected from a WM slab. If the period of the wires (a) is much smaller than the wavelength (λ), the WM effectively behaves as a continuous material [51].

For the waves propagating perpendicularly to the wires, the effective permittivity of the WM is found in Ref. [94] as:

$$\varepsilon = \varepsilon_0 \left(1 - \frac{\omega_p^2}{\omega^2}\right), \tag{4.1}$$

where ω_p, the plasma frequency, is given by

$$\omega_p = \frac{c}{a}\sqrt{\frac{2\pi}{\ln\left(\frac{a^2}{4r(a-r)}\right)}}, \tag{4.2}$$

and r is the wire radius.

Most of the MMs designed for microwave applications are regular periodic structures. Although periodicity can be sometimes a necessary property (like, for example, in the photonic band gap (PBG) MMs), a dense WM does not really need to be periodic to provide the same plasma-like effective permittivity of Eq. 4.1. Moreover, periodicity in MMs designed for suppression of the propagation may open new bands in which waves can propagate. In this work we consider WM-like structures with periods much smaller than the wavelength, in which the stop band is determined not because of the periodicity, but due to the fact that, for $\omega < \omega_p$, the effective permittivity of the WM is negative.

This work is centred on the planar fractal structure of Fig. 4.1, which is known as the Sierpinski carpet. It is formed by taking a unit square, dividing it into 9 equal smaller sub-squares and then filling in the central square (the black square in the middle). Then, we repeat the procedure recursively for each sub-square, in an iterative form.

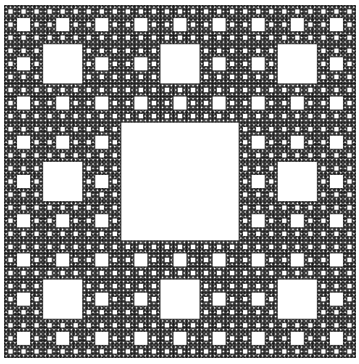

FIGURE 4.1: Geometry of the Sierpinski carpet fractal

It can be shown that the remaining unfilled geometrical area of the fractal structure can be calculated from Eq. 4.3

$$A_n = \left(\frac{8}{9}\right)^n \tag{4.3}$$

where n is the fractal iteration order. Because this remaining area (A_n) tends to zero when $n \to \infty$, the structure will be successively more filled as the fractal iteration is increased. The Hausdorff dimension of the Sierpinski carpet is $dim = \frac{\ln 8}{\ln 3} = 1.8928$, which is smaller than 2.

4.2 Design

In this work, we design a WM-like MM of cylindrical wires, based on the Sierpinski carpet fractal. In order to represent this fractal in the electromagnetic simulation software, we used the IFS method as described by the following set of equations:

$$\begin{aligned}
f_1(x) &= \begin{pmatrix} \frac{1}{3} & 0 \\ 0 & \frac{1}{3} \end{pmatrix} x, & f_2(x) &= \begin{pmatrix} \frac{1}{3} & 0 \\ 0 & \frac{1}{3} \end{pmatrix} x + \begin{pmatrix} 0 \\ \frac{1}{3} \end{pmatrix}, \\
f_3(x) &= \begin{pmatrix} \frac{1}{3} & 0 \\ 0 & \frac{1}{3} \end{pmatrix} x + \begin{pmatrix} 0 \\ \frac{2}{3} \end{pmatrix}, & f_4(x) &= \begin{pmatrix} \frac{1}{3} & 0 \\ 0 & \frac{1}{3} \end{pmatrix} x + \begin{pmatrix} \frac{1}{3} \\ 0 \end{pmatrix}, \\
f_5(x) &= \begin{pmatrix} \frac{1}{3} & 0 \\ 0 & \frac{1}{3} \end{pmatrix} x + \begin{pmatrix} \frac{1}{3} \\ \frac{2}{3} \end{pmatrix}, & f_6(x) &= \begin{pmatrix} \frac{1}{3} & 0 \\ 0 & \frac{1}{3} \end{pmatrix} x + \begin{pmatrix} \frac{2}{3} \\ 0 \end{pmatrix}, \\
f_7(x) &= \begin{pmatrix} \frac{1}{3} & 0 \\ 0 & \frac{1}{3} \end{pmatrix} x + \begin{pmatrix} \frac{2}{3} \\ \frac{1}{3} \end{pmatrix}, & f_8(x) &= \begin{pmatrix} \frac{1}{3} & 0 \\ 0 & \frac{1}{3} \end{pmatrix} x + \begin{pmatrix} \frac{2}{3} \\ \frac{2}{3} \end{pmatrix}.
\end{aligned} \tag{4.4}$$

Here, x is the 2-dimensional vector representing a point within a unit square. Thus, the Sierpinski carpet has 8 similar parts, corresponding to each of the above equations in each iteration [95].

We distributed the wire position and the radius as is shown in Fig. 4.2. In this figure, which shows the cross-section orthogonal to the wires, the central wire has the radius $r = 0.15a$, where a is the dimension of the cell. The cells are periodically repeated so that a crystal of infinite parallel cylinders is formed. In order to simulate this structure, we used MPB (MIT Photonic Band) and Meep.

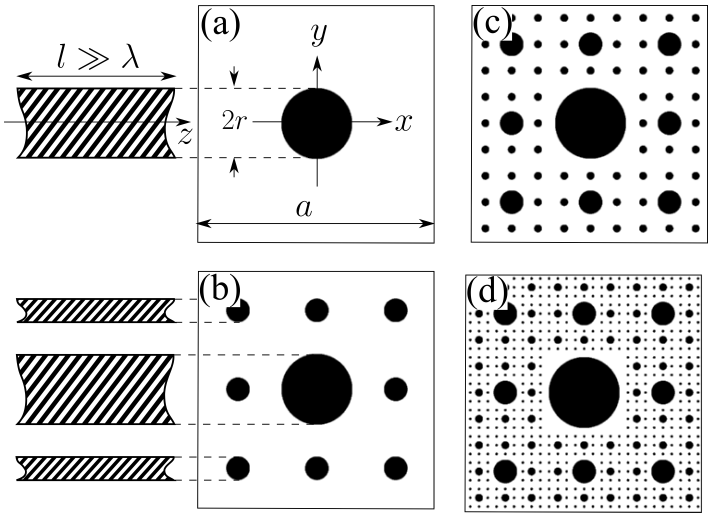

FIGURE 4.2: WM structures based on Sierpinski Carpet distribution. a) the 1st order structure (the traditional WM): the unit cell cross-section in xy-plane, b) the same as a) but for the 2nd order structure, c) the same as a) but now for the 3rd order structure, d) the same as a) for the 4th order structure. The drawings on the left are the cross-sections in yz-plane.

We simulated WM-like structures comprised by either conducting or dielectric wires. On one hand, MPB simulator was used to calculate the band structure of the dielectric fractal array since this simulator only allows for dispersionless dielectrics with positive ε. On the other hand, Meep was used to calculate the band structure for the metallic wire medium characterized by a Drude-type negative dispersive permittivity. In both simulators, we used the IFS approach to build the fractal structure.

The relative permittivity of the dielectric wires has been selected to be high enough so that, for the waves polarized orthogonally to the wires (the TM waves in which the electric field is in the plane of Fig. 4.2), the properties of the dielectric structure are similar to the ones of the metallic structure. For the waves with the electric field polarized along the wires (the TE waves), the dielectric and the metallic structure behave differently. When possible, using a frequency-domain tool such as MPB for band structure calculations is preferable, because MPB is known to be more reliable than Meep (which is a time-domain solver) in this regard. For instance, in MPB, the modal frequencies are uniquely sorted by bands, while in Meep, in some situations, the closely located bands may mix up.

4.3 Simulation Results

The simulated band diagrams for the first three Sierpinski-based fractal geometries shown in Fig. 4.3 (panels a, b, c) demonstrate similar frequency response (especially, in the case of the TM polarization). These results are shown in Fig. 4.3 for the two lowest bands of transmission in the structures mentioned above, both for TE and TM polarized waves.

The TE band curves shown in this figure are for the structures with metallic wires. On the other hand, it was found that simulated TM curves for the WM structures with metallic wires and with the dielectric ones practically coincided. Fig. 4.3 depicts only the TM curves obtained with MPB for the structures with dielectric wires.

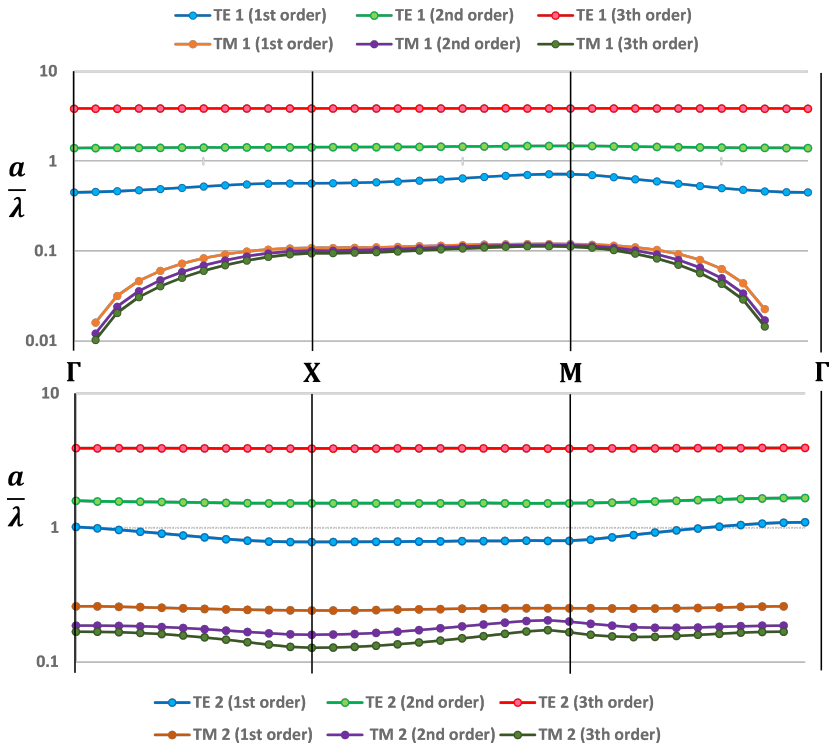

FIGURE 4.3: Band structure of the fractal WM MM. The top plot shows the diagrams for the first TE and TM bands in the WM fractal structures of the 1st, 2nd and 3rd order [Fig. 4.2 (a,b,c)]. The bottom plot depicts the diagrams for the second TE and TM bands for the same structures. The points Γ, X, and M on the horizontal axis represent the values $(0,0),(\frac{\pi}{a},0),(\frac{\pi}{a},\frac{\pi}{a})$ of the wave vector k in the xy-plane, respectively. The intermediate values for k are obtained by linear interpolation between these points.

We see that the TE waves do not propagate at frequencies below a certain cut-off frequency. Moreover, the obtained results demonstrate that, by replacing the regular WM structure by the fractal one, we can significantly increase the cut-off frequency (the plasma frequency) of

the structure for the TE polarized waves by up to 8 times, without affecting propagation in the lowest TM bands.

Fig. 4.4 shows the relation between the plasma frequency and the radius of the wires for the fractal structures of the 1st, 2nd and 3rd order [Fig. 4.2 (a,b,c)]. It is seen that the plasma frequency increases simultaneously with the radius. The upper limit for the radius of the wires can be calculated for each structure, in order to avoid the contact between the wires. For the 1st order, the maximum is $r_{max} = \frac{a}{2}$. This value gets smaller as the order increases. For the 2nd and 3rd order the maximum acceptable radius values are $\frac{a}{4}$ and $\frac{a}{5}$, respectively.

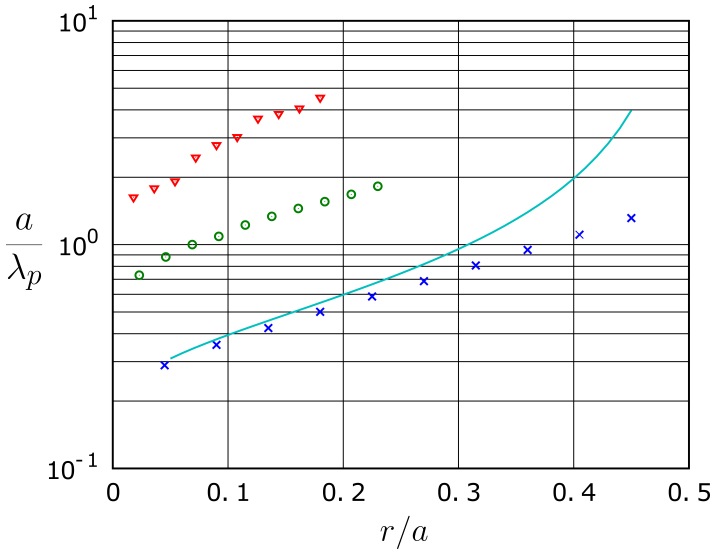

FIGURE 4.4: The cut-off (plasma) frequency as a function of wire radius for the first TE band in the WM fractal structures of the 1st, 2nd and 3rd order [Fig. 4.2 (a,b,c)]. Blue crosses: 1st order fractal structure. Green circles: 2nd order fractal structure. Red triangles: 3rd order fractal structure. The solid line shows the theoretical estimation by the approximate Eq. 4.2 for the first-order structure, where $\frac{a}{\lambda_p} = \frac{\omega_p a}{2\pi c}$.

It can be concluded from the geometry of this structure that the weight of the structure is proportional to:

$$W_n = \pi r^2 l \sum_{k=0}^{n-1} \left(\frac{8}{9}\right)^k \tag{4.5}$$

where l is the height of the cylinders, and n is again the iteration order of the Sierpinski carpet fractal structure. From this equation we can conclude that the mentioned change in the geometry of the structure is associated with an increase in the weight of the structure. However, while the plasma frequency increases by about 8 times, the structural weight increases only by about 2.7 times, as compared to the original structure (Fig. 4.2). On the other hand, it can be estimated from Eq. 4.2 that to increase the plasma frequency in the

same proportion, one would have to increase the wire radius by about 3 times, which would result in a greater increase of the structural weight.

4.4 Conclusion

In this chapter we have studied a wire medium type MM with the wires distributed in accordance with the Sierpinski carpet fractal. We have simulated the band diagrams of this fractal structure for TE and TM polarized waves and have shown that the Sierpinski wire medium structure in certain cases outperforms traditional periodic wire media.

Part II

Fractal-based Coding Strategies

Chapter 5

Fractal Coding Metamaterials

We propose the concept of fractal coding metamaterials, which can be used to design reflective metasurfaces with self-similar pseudo-random phase responses based on the coding strategy utilizing fractal interpolation functions (FIF). We consider the class of fractals whose FIF is formed by a contraction mapping on the y-coordinate and an arbitrary linear function of the x-coordinate. This formulation is used in deriving the theoretical model and in the experimental realization. An analytical relation between the reflection phase distribution in the form of the above-mentioned FIF and the far-field radiation pattern of the structure is derived. In the numerical example, a reflecting metasurface formed by slotted metallic patches of varying sizes is considered. A number of full wave scattering simulations for such a metamaterial reflectarray are performed and the optimal designs which make the response of the structure more accurate as compared with the analytical predictions are identified. Following the simulation results, the array is built and a number of measurements are performed. The results of this work may find applications in phased antenna array design and beam forming.

5.1 Introduction

This chapter deals with the concept of fractal coding metamaterials. Historically, the coding metamaterials started with the concept of digital metamaterials first presented in Ref. [96]. The goal of this concept is to build metamaterials with the desired effective parameters, like the effective dielectric permittivity ε_{eff}. In Ref. [96], the metamaterial structure is made of two components: one with negative epsilon (silver (Ag) with $\varepsilon_{\text{m}} = -4.7 + i0.22$) and another with

positive epsilon (silica (SiO_2) with $\varepsilon_d = 2.42$). The resulting ε_{eff} depends on the geometrical arrangement of these two materials and the direction of the incident field which is applied to the structure (i.e., the structure is anisotropic). The effective permittivity can be either in the range between the two permittivity values ε_m and ε_d (the weighted average of them) or well outside of this range. Considering the desired value of ε the structure and material can be selected. Since the study of Ref. [96] was done for just the two-dimensional (2D) case, the validity of the formulas for the three-dimensional (3D) case should be tested separately. Also, the structures are studied just at a single wavelength and thus cannot not be considered for operation in a wide bandwidth.

Later, in Ref. [97], the concepts of coding metamaterials, digital metamaterials and programmable metamaterials were presented in order to pursue the goal of controlling electromagnetic waves. In Ref. [97], the basic elements of the structure are not just blocks of different materials. Instead, the "0" and "1" elements are represented by metallic patches on a dielectric substrate. These elements when reflecting an incident electromagnetic wave have different phase responses. For example, for the 1-bit coding metamaterial the maximum phase difference one can use is π and therefore one of the patches is designed to have 0 phase response and another one with π phase response. The phase difference stays 180° in a quite wide range of frequencies and thus one may realize the desired phase response in a wider bandwidth. It is clear that with this method one can also introduce n-bit coding metamaterials with $2n$ different elements. When n increases, the phase differences decrease and the accuracy in the design becomes more important. Also, the requirement of having wider bandwidth puts more restrictions onto the design of the elements.

In order to control the phase response of the structure electrically, in Ref. [97], a single element has been introduced with a diode that connects two symmetric metallic patches on the dielectric substrate (F4B with dielectric constant of 2.65 and loss tangent of 0.001). It is shown that by turning the diode on and off one can obtain the phase responses corresponding to the "0" and "1" elements as discussed above. The phase difference stays in the vicinity of π in a shorter bandwidth as compared with the previous design. The programmable metasurface proposed in the same reference is controlling "0" and "1" sequences with a Field Programmable Gate Array (FPGA). By triggering switches in the FPGA, the distribution of the induced current changes on the surface of the structure and consequently the structural elements will perform either as "0s" or "1s" as programmed. The basic elements can be phase-controlled or polarization-controlled.

Following the introduction of the coding metamaterials, there have been numerous papers trying to address various problems with this newly developed concept such as dealing with abnormal scattering and reflection properties [98–100], designing coding metamaterials based on the Quick-Response code [101], performing coding relevant to the electromagnetic waves polarization [102], etc. More examples and reviews of the coding and programmable metamaterials for different applications can be found in Refs. [103–106]. Some other methods for beam forming also have been studied in Refs. [107–109].

In order to expand the idea of controlling electromagnetic waves by coding metasurfaces, here we approach the problem from a different point of view. In this work we design an array of patches with varying size in a way that the phase response of the final structure can be presented in the form of a fractal. Fractal functions are known to exhibit self-similarity and pseudo-randomness, which can be useful in applications such as complex beam forming for phased array antennas, in the design of Multiple Input Multiple Output (MIMO) antenna systems, and in other areas.

Namely, in this work we develop a method of designing a reflective metasurface with a given form of the phase response using the concept of coding metamaterials extended by the novel idea of fractal coding. Having the ability to predict the behaviour of such fractal structures in terms of the far-field radiation patterns is interesting for the above-mentioned applications. In order to achieve this goal, we consider fractal metasurfaces whose encoded phase response is determined by the fractal interpolation function (FIF) ($y = f(x)$), which is formed by a linear contraction mapping on y and an arbitrary linear function of x. We consider analytically the case when the phase distribution on the structure takes the form of the above-mentioned FIF and find the far-field radiation pattern of the structure. In the numerical examples we consider a reflecting metasurface formed by metallic patches of varying sizes with four slots of varying lengths. We perform a number of full wave scattering simulations for such a metamaterial reflectarray and identify the optimal designs which make the final response of the structure more accurate when compared with the analytical predictions. At the last stage, the final structure is built and the corresponding validation measurements are performed.

5.2 Theory

5.2.1 Fractal interpolation functions

To derive the radiation pattern of the reflect array with a fractal phase distribution, we need some mathematical tools in order to represent fractals analytically. Iterative function systems (IFS) can be considered as such a tool for self-similar fractals [110]. IFS is one of the most general ways to formulate fractals mathematically.

Fractal interpolation function (FIF) was first introduced by Barnsley [95]. The idea is based on iterated function systems (IFS). By definition, the fractal interpolation curve or surface is a unique function that is the attractor of the related IFS. IFS itself is the generalization of Banach fixed-point theorem.[1] There is still no evidence of the existence of the FIF in complete metric space. One should also note that in principle it is possible to use other fixed-point theorems (e.g. Rakotch's fixed point theorem) in order to prove the existence of FIF.

By definition, the fractal interpolation function (FIF) which is generated by the iterative function system is a unique function $f : X \to \mathbb{R}$ that maps the affine map of a set of points to a contraction map:

$$f(L_j(x)) = F_j(x, f(x)), \quad j = 1, 2, ..., N, \quad x \in X, \tag{5.1}$$

where $X = [x_0, x_N]$, $L_j : X \to X$ is an affine map satisfying $L_j(x_0) = x_{j-1}$, $L_j(x_N) = x_j$, $j = 1, 2, ..., N$ (let $x_0 < x_1 < ... < x_N$) and $F_j : X \times \mathbb{R} \to \mathbb{R}$ is the contraction mapping (the distance between a set of points after transformation is smaller than α multiplied by their original distance):

$$F_j(x_0, y_0) = y_{j-1}, \tag{5.2}$$

$$F_j(x_N, y_N) = y_j, \qquad j = 1, 2, ..., N, \tag{5.3}$$

$$|F_j(x, y_1) - F_j(x, y_2)| \leqslant |\alpha_j||y_1 - y_2|, \qquad -1 < \alpha_j < 1, \tag{5.4}$$

where $y_0, y_1, ..., y_N \in \mathbb{R}$.

[1] Banach fixed-point theorem guarantees the existence and uniqueness of fixed points of specific self-maps (compact sets) of metric space. The theory also presents a method to find these points[111].

Eqs. 5.2 and 5.3 define the continuity condition for function f. Deterministic fractal associated with this FIF is the attractor of the IFS on $X \times \mathbb{R}$ [112]. When an IFS satisfies the condition 5.4, that iterated function system is called hyperbolic. It is proven that a hyperbolic IFS has a unique attractor [95]. So as we said before, we can say that the FIF is unique, which can be used as the project function for the phase distribution on the reflecting metasurface.

In this work we consider a group of FIF with the following form of contraction mapping:

$$F_j(x, y) = q_j(x) + \alpha_j y, \tag{5.5}$$

where q_j is linear.

In this case, it can be proven that the integral of such FIF is also a FIF. For the integral of fractal interpolation function we have in this case[112]:

$$\begin{aligned} g(L_j(x)) &= \int_{x_0}^{x} f(L_j(t))\, dt \\ &= {q'}_j(x) + {\alpha'}_j g(x), \end{aligned} \tag{5.6}$$

where

$${\alpha'}_j = \alpha_j \frac{x_j - x_{j-1}}{x_N - x_0}, \tag{5.7}$$

$${q'}_j(x) = g(x_0) + g(x_{j-1}) - {\alpha'}_j g(x_0) + \frac{{\alpha'}_j}{\alpha_j} \int_{x_0}^{x} q_j(t) dt. \tag{5.8}$$

which shows that the integral of the FIF is also a FIF with a similar form as compared to the function under integral. In a similar way, it can be proven that the Fourier transform of a FIF with linear $q_j(x)$ is also a FIF [113]. Using the above mentioned theorems we can prove that the Fourier transform of an exponential function of a FIF can be also a FIF. For that we consider a FIF with linear $q_j(x)$:

$$f(L_j(x)) = q_j(x) + \alpha_j f(x), \tag{5.9}$$

where we have:

$$q_j(x) = a_j x + b_j. \tag{5.10}$$

Now we want to prove that $\hat{f}(x)$ can be also a FIF, where

$$\hat{f}(x) = e^{f(x)}. \tag{5.11}$$

Using the continuity condition of the affine map ($L_j(x_0) = x_{j-1}$, $L_j(x_N) = x_j$), we can prove that:

$$\hat{f}(x_j) - \hat{f}(x_{j-1}) = \hat{f}(x_N)^{\alpha_j} e^{q_j(x_N)} - \hat{f}(x_0)^{\alpha_j} e^{q_j(x_0)}. \tag{5.12}$$

Considering the equality $\hat{f}(x_j) = \hat{f}(x_0) + \sum_{n=1}^{j}(\hat{f}(x_n) - \hat{f}(x_{n-1}))$, we have:

$$\hat{f}(x_j) = \hat{f}(x_0) + \sum_{n=1}^{j}(\hat{f}(x_N)^{\alpha_n} e^{q_n(x_N)} - \hat{f}(x_0)^{\alpha_n} e^{q_n(x_0)}). \tag{5.13}$$

Therefore, for the $\hat{f}(L_j(x))$ we have:

$$\hat{f}(L_j(x)) = \hat{f}(x)^{\alpha_j} e^{q_j(x)}. \tag{5.14}$$

Using the Taylor polynomial we have:

$$\hat{f}(L_j(x)) \approx \hat{\alpha_j}\hat{f}(x) + \hat{q_j}(x), \tag{5.15}$$

where,

$$\hat{\alpha_j} = \alpha_j e^{q_j(x_k)} \hat{f}(x_k)^{\alpha_j - 1}, \tag{5.16}$$

$$\hat{q_j}(x) = \hat{a_j} x + \hat{b_j},$$

$$\hat{a_j} = a_j \hat{f}(x_k)^{\alpha_j} e^{q_j(x_k)}, \tag{5.17}$$

$$\hat{b_j} = (1 - a_j x_k + \alpha_j)\hat{f}(x_k)^{\alpha_j} e^{q_j(x_k)} \tag{5.18}$$

where x_k is the point around which we perform the linearisation and $\hat{f}(x_k)$ can be obtained from Eq. 5.13.

5.2.2 Radiation pattern of a fractal reflect array

We assume that the structural elements are distributed over a rectangular surface laying on the xy plane. The z axis is perpendicular to the center of this surface. The surface is illuminated by a normally incident plane electromagnetic wave $\vec{E}_{\text{inc}} = E_{\text{inc}}\vec{y}_0$ such that after the reflection from the surface, the electric field of the reflected wave on the surface is $\vec{E} = E_y\vec{y}_0$ with $E_y = E_0 \mathrm{e}^{j\phi(x,y)}$, where $\phi(x,y)$ is the reflection phase distribution on the surface. This surface acts as an emitting aperture antenna. The far-field electric field created by the small rectangular element of the surface (dx, dy) is [114]:

$$d\vec{E}|_R = \vec{y}_0(\vec{u}_0 \cdot \vec{z}_0)\frac{jkE_0}{2\pi R(x,y)}\mathrm{e}^{-jkR(x,y)}\mathrm{e}^{j\phi(x,y)}\,dx\,dy, \tag{5.19}$$

where $\vec{u}_0$ is the vector in the direction of the line which connects the center of the structure to the far field observation point, and $R(x,y)$ is the distance between the point on the surface and the far field point:

$$R(x,y) = R_0 - x(\vec{x}_0 \cdot \vec{u}_0) - y(\vec{y}_0 \cdot \vec{u}_0) = R_0 - (x\vec{x}_0 + y\vec{y}_0) \cdot \vec{u}_0. \tag{5.20}$$

By substituting Eq. 5.20 in Eq. 5.19 and defining $\boldsymbol{\vec{\rho}} = x\vec{x}_0 + y\vec{y}_0$, we obtain:

$$d\vec{E}|_R = \vec{y}_0(\vec{u}_0 \cdot \vec{z}_0)\frac{jkE_0}{2\pi R(x,y)}\mathrm{e}^{-jkR_0}\mathrm{e}^{jk\boldsymbol{\vec{\rho}}\cdot\vec{u}_0}\mathrm{e}^{j\phi(x,y)}\,dx\,dy. \tag{5.21}$$

The varying distance $R(x,y)$ in the denominator can be approximated by the distance to the center of the surface R_0. The far field is obtained by integrating Eq. 5.21 over the reflecting surface:

$$\begin{aligned}\vec{E}|_R &= \iint_A d\vec{E}|_R \\ &= \vec{y}_0(\vec{u}_0 \cdot \vec{z}_0)\frac{jk}{2\pi R_0}\mathrm{e}^{-jkR_0}\iint_A E_0\mathrm{e}^{j\phi(x,y)}\mathrm{e}^{j(k_x x + k_y y)}dxdy,\end{aligned} \tag{5.22}$$

where $k_x = k(\vec{x}_0 \cdot \vec{u}_0)$, and $k_y = k(\vec{y}_0 \cdot \vec{u}_0)$.

From Eq. 5.22, it can be seen that, in the far zone, the reflected field is proportional to the Fourier transform of the same field as distributed on the reflecting surface. In order to investigate the effect of the fractal phase distribution on the far-field pattern, we go through an example and build a reflectarray which demonstrates such properties.

5.3 Numerical Example: A linear reflect array formed by slotted metallic patches

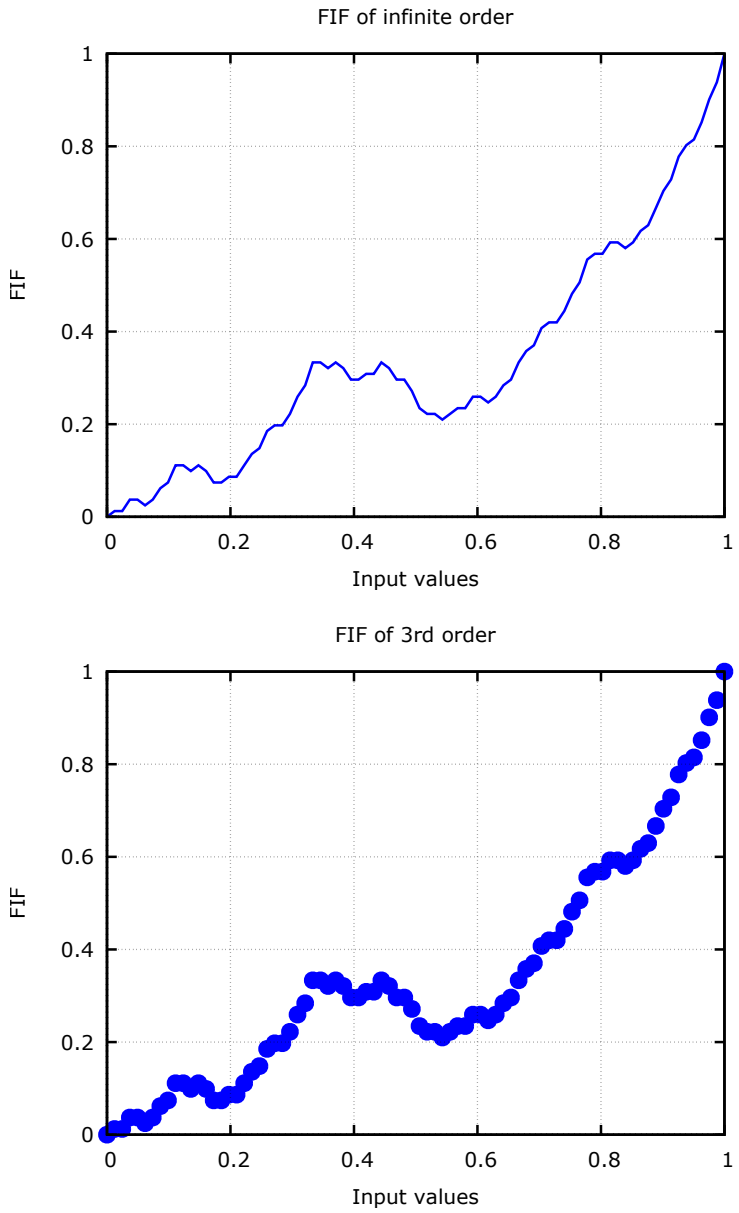

FIGURE 5.1: Top: Fractal interpolation function of order $N \to \infty$. Bottom: Approximation of the fractal interpolation function of order 3 by a set of 82 discrete points. We want the unwrapped phase response of the reflect array with 82 elements to resemble this graph.

In this section we study a linear reflect array formed by slotted metallic patches on a dielectric substrate. In order to design the necessary phase distribution along the array, we consider the following affine and contraction mappings which define the FIF that will be used as an

example for the following simulations:

$$L_1(x) = \frac{x}{3}, \quad L_2(x) = \frac{x}{3} + \frac{1}{3}, \quad L_3(x) = \frac{x}{3} + \frac{2}{3}, \tag{5.23}$$

$$F_1(x,y) = \frac{y}{3}, \quad F_2(x,y) = \frac{y}{3} - \frac{x}{3} + \frac{1}{3}, \quad F_3(x,y) = \frac{y}{3} + \frac{x}{3} + \frac{1}{3}, \tag{5.24}$$

and f passing through $(0,0)$, $(1/3,1/3)$, $(2/3,1/3)$ and $(1,1)$. The number of points in this function is $3^{N+1}+1$, where N is the number of interpolations. When N goes to infinity the fractal function will tend to the graph shown in Fig. 5.1 (top). The x and y axes on this plot correspond to, respectively, the relative position along the reflect array and the relative value of the reflection phase as to be realized in an ideal case.

In practice, we have to limit the number of fractal elements in a realization to a reasonable value. In this example we go through just three iterations of FIF (i.e., $N = 3$), which results in a set of 82 discrete points approximately representing the original fractal function. The plot of this set is shown in Fig. 5.1 (bottom).

In order to build the reflectarray we first need to design an array element with high enough reflection phase variation. A large number of possible designs were tested, ranging from simple square metallic elements with varying sizes, to complex structures such as slotted metallic patches based on the Hilbert space-filling curve fractal (Fig. 5.2).

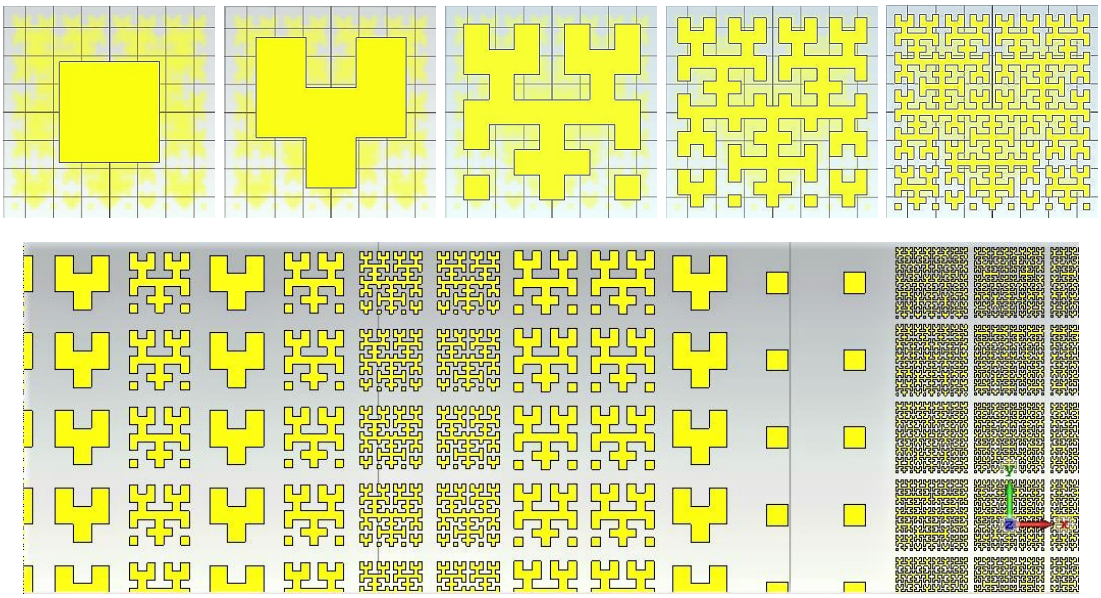

FIGURE 5.2: Patches designed based on the Hilbert curve and the corresponding array.

The patch design with the widest range of phase variation with respect to its geometric parameters such as width, the slot length, etc. at around 9 GHz frequency has been selected.

This selected design of the slotted patch is shown in Fig. 5.3 (top). The simulation result of the phase response of this patch when changing the sizes of the slots and the patch is shown in Fig. 5.3 (bottom).

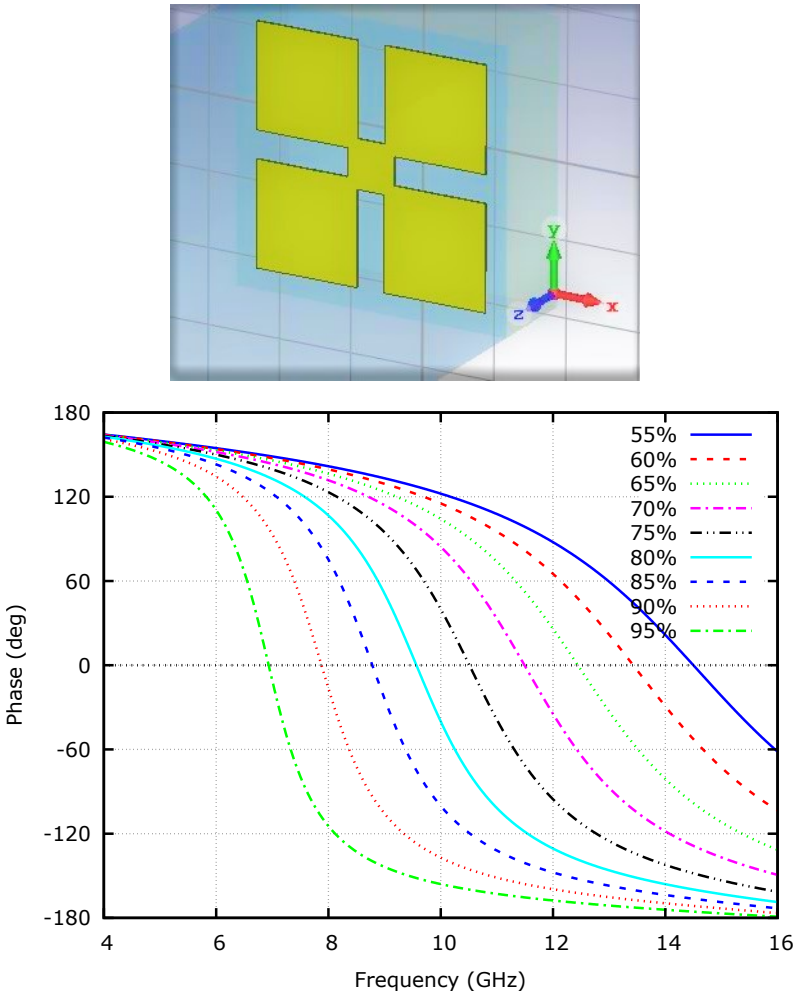

FIGURE 5.3: Top: Basic element of the reflectarray: a slotted metallic patch on a grounded dielectric substrate with $\varepsilon = 6.15$ and thickness $1.524mm$. Bottom: Simulation results for phase response of the basic element as a function of frequency and one of the structural parameters (the relative sizes of the patch). The overall size of the array element (the unit cell size) is $4.16mm$.

Based on these results, the optimal operating frequency which gives the widest range of the phase variation with the patch size that has been selected, and the relation between the size of the patch and the reflected phase at this specific frequency have been found by constructing an interpolation function. The result of such interpolation at 9 GHz is shown in Fig. 5.4.

Next, by using this interpolation function we can map the required fractal phase distribution to the required patch size in each unit cell of the array. We select the total phase variation along the complete array to be 6π radians (3×360 degrees). The mapping result is presented

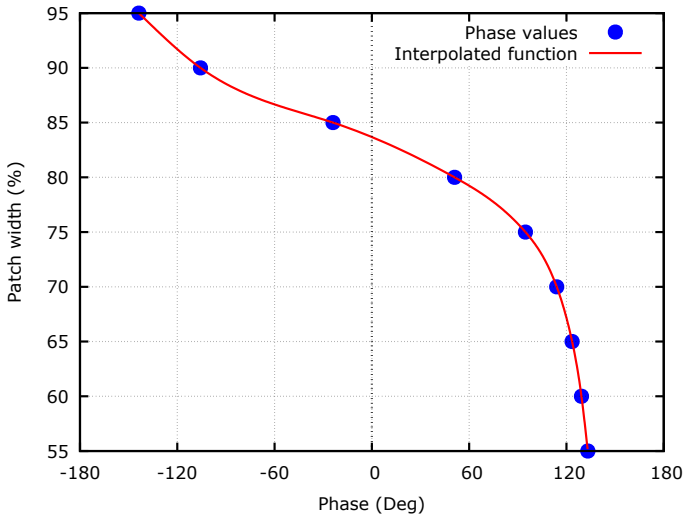

FIGURE 5.4: Phase response of the slotted patch on a grounded substrate at 9 GHz as a function of the relative patch size.

in Fig. 5.5 (top). The abrupt changes in the patch size in this figure correspond to the points where the phase wraps over the realizable phase interval $-150° < \phi + \phi_0 < +150°$, where $\phi_0 = 20°$. Note that, because at the end points of this interval the reflection phase is rather close to $\pm 180°$, such abrupt changes in the patch size do not result in large variations of the phase factor $e^{i\phi}$, and thus this factor changes more or less smoothly along the array even at those points. If the patch sizes in the array follow the values obtained from Fig. 5.5 (top), then we will have the fractal reflection phase distribution shown in Fig. 5.5 (bottom).

Based on these results, we have simulated such an array of patches with varying sizes (which will have the desired phase response) and calculated its far field radiation pattern by using the CST Microwave Studio. The geometry of the complete reflectarray is shown in Fig. 5.6. The array is formed by 11 horizontal rows of patches of varying size. The linear patch arrays in each row have the same geometry. Hence, this reflectarray will have the radiation pattern in the horizontal plane determined by the fractal phase distribution along the patch arrays.

The simulation results for the reflection phase response of this array (as well as similar structures formed by five rows of patches, and effectively infinite number of rows) compared to the original theoretical prediction are presented in Fig. 5.7. As it is seen from this Figure the simulation results are in good agreement with the theoretical results, which shows that the presented method for realization of the reflectarray works well.

We have also calculated the far field radiation pattern of these structures in the CST Microwave Studio and compared it with the theoretical one obtained with Eq. 5.22. The result

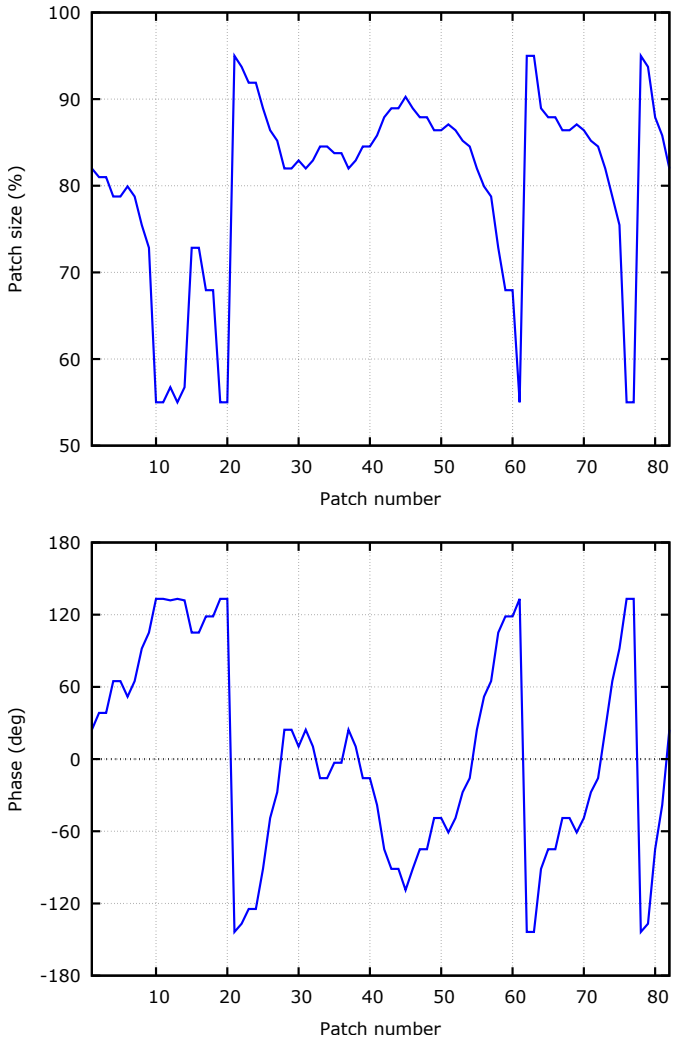

FIGURE 5.5: Top: Patch size for the elements of the reflectarray as a function of the element index (patch number). Bottom: Phase response of the same array as a function of the element index.

of these calculations can be seen in Fig. 5.8. We observe a satisfactory agreement between the theoretically predicted radiation pattern and the simulated ones in the main beam region. The discrepancies seen in Fig. 5.8 can be explained by the fact that the theoretical formula takes into account only the phase variation of the reflected field assuming the fixed reflection amplitude, while in the real structure the amplitude of the reflected field also changes along the structure. The theoretical result also does not take into account the edge diffraction effects, which may have a detrimental effect on the radiation pattern, especially on the level of the side lobes.

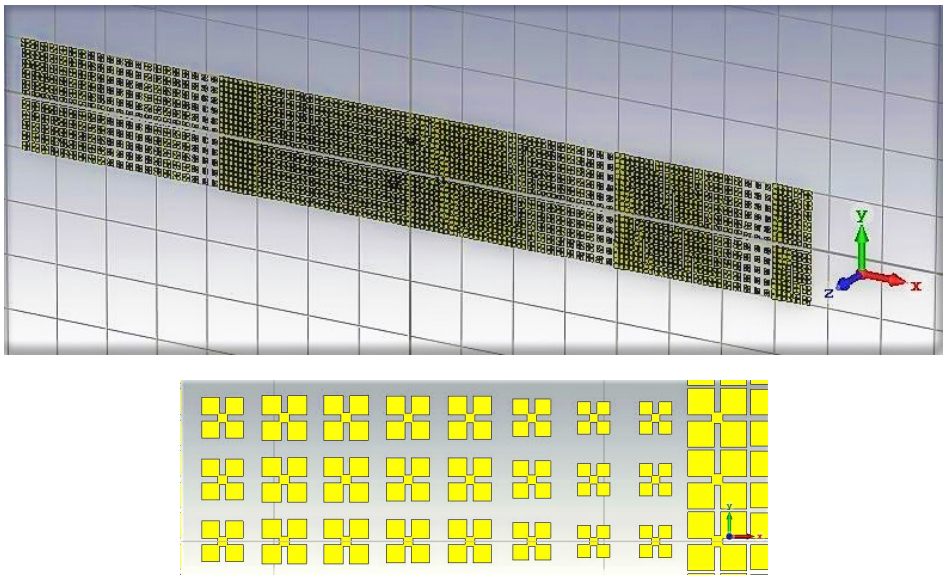

FIGURE 5.6: Top: Array of patches as modelled in CST Microwave Studio. Bottom: Magnified view of a region of the array.

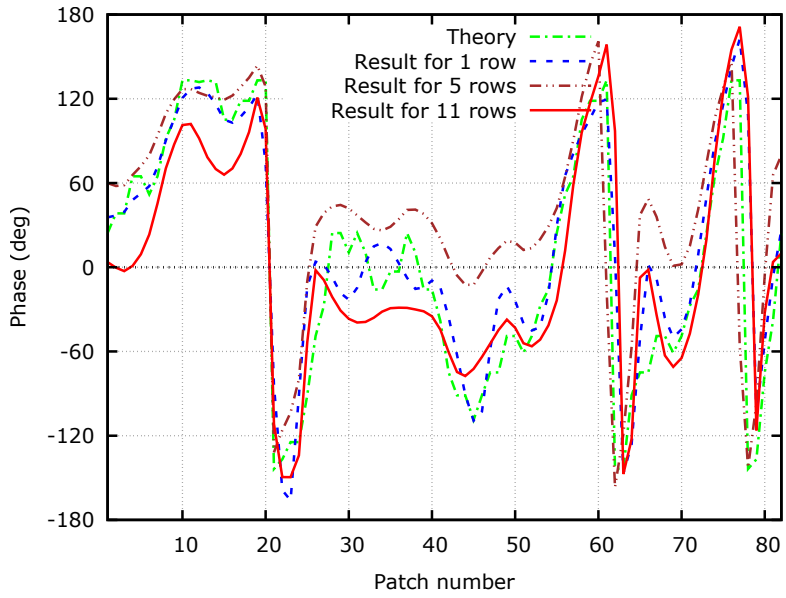

FIGURE 5.7: Phase response of the array with one row of patches placed in a two-plate waveguide (which represents an array with effectively infinite number of horizontal rows), and with 5 and 11 rows placed in free space, as compared to the theoretical prediction.

5.4 Experimental results

In order to provide an experimental validation of the proposed reflectarray design, we selected the array with 11 rows (Fig. 5.9). The dimension of the structure was 341.43 mm by 46.15 mm. Substrate was Rogers RO4360G2 with relative permittivity of 6.15 and thickness of 1.524 mm. The metallization thickness was 17.5 μm. Since the total structure length was larger than

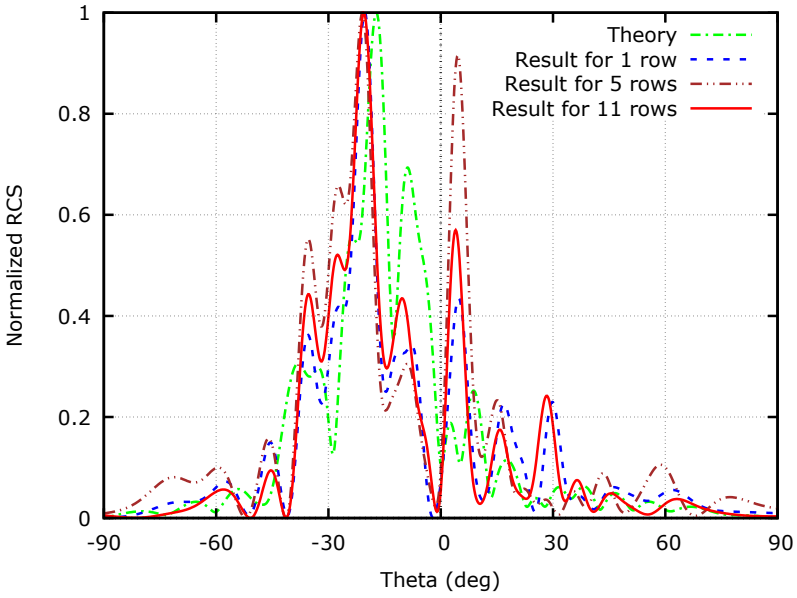

FIGURE 5.8: Far field radiation patterns for an array with 1 row (in a parallel plate waveguide), 5 rows and 11 rows (in free space), as compared with the theoretical result.

the maximum length available for the substrate, the reflectarray structure was made in two halves and then glued together as is shown in Fig. 5.9. The reflectarray was produced with printed circuit board (PCB) technology using a CNC (Computer Numerical Control) milling machine.

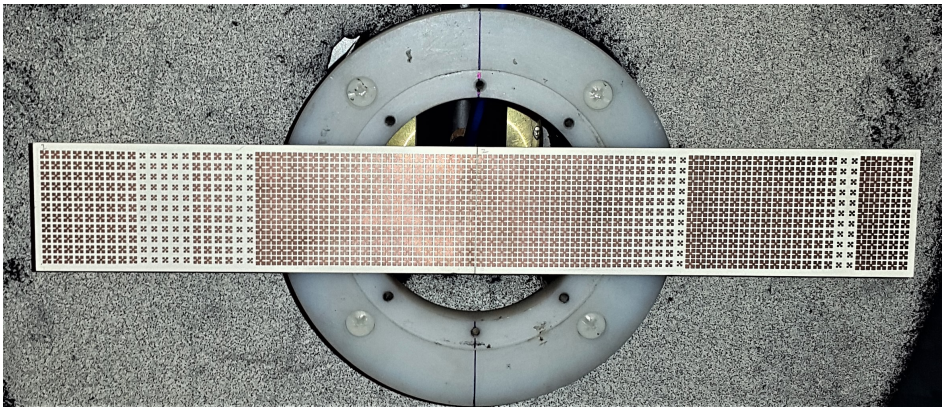

FIGURE 5.9: Reflectarray with 11 rows of slotted patches formed on a printed circuit board. A part of the supporting structure and the anti-reflection absorber are seen behind the array.

To conduct the experiment in anechoic chamber we designed an arm to rotate the transmitter antenna together with the reflect array around the y-axis while the receiver antenna was fixed at one end of the chamber (Fig. 5.10), in order to measure bistatic radar cross section (RCS). In this way, the angle of incidence is kept constant while the angle at which the field scattered by the reflectarray is measured is changing.

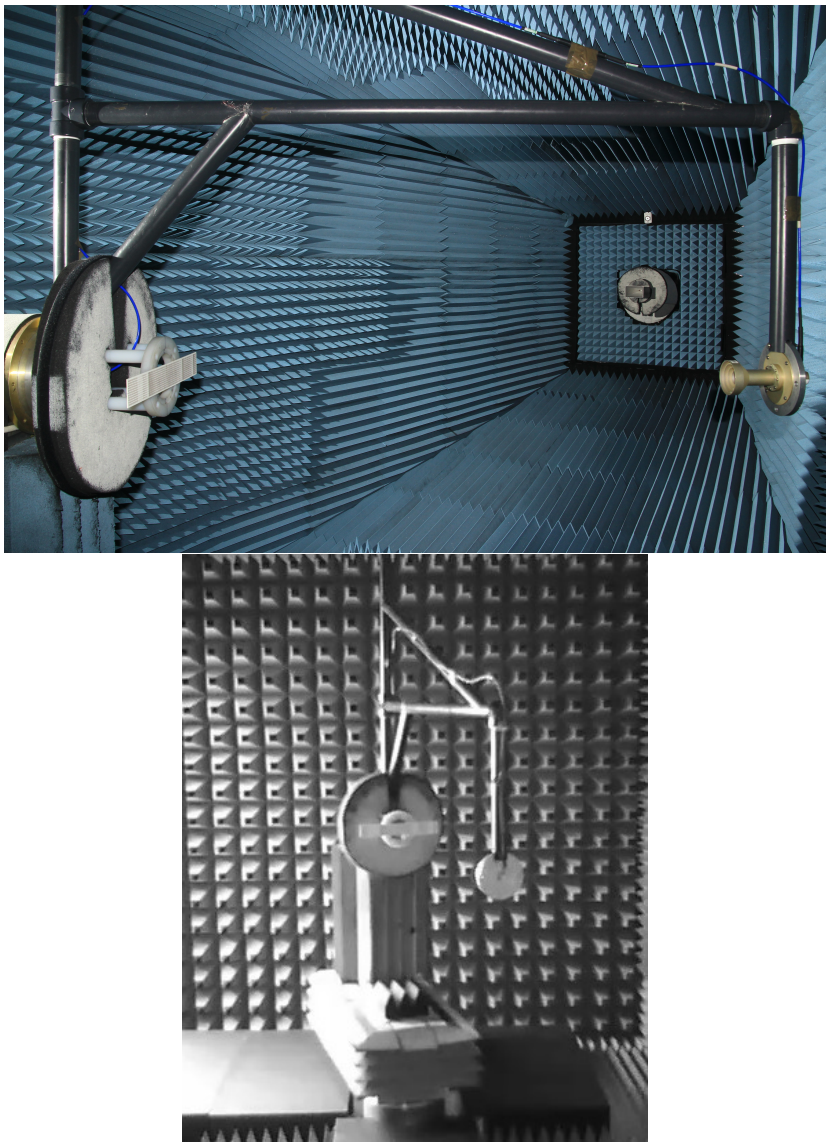

FIGURE 5.10: Photo of the complete experimental setup assembled for anechoic chamber measurements of bi-static radar cross section. The supporting structure built from PTFE pipes, the array and the transmitting antenna are seen in the front. The receiving antenna is seen in the back. Bottom: Another view from the camera installed inside the anechoic chamber.

The supporting structure was made from polytetrafluoroethylene (PTFE) pipes. PTFE has a relatively low refracting index at microwave frequencies, which helps to minimize reflections from the support.

As the receiver we used a pyramidal horn antenna operating at 9 GHz frequency and with the working frequency range between 8 GHz to 12 GHz. The transmitter antenna was a corrugated conical horn antenna. We did the measurements in the presence of the array and also without the array, in order to measure the reflection from the surroundings.

Fig. 5.11 shows the comparison between the measurement results and the theoretical and simulated values. The shift in the position of the main maximum is due to a systematic error

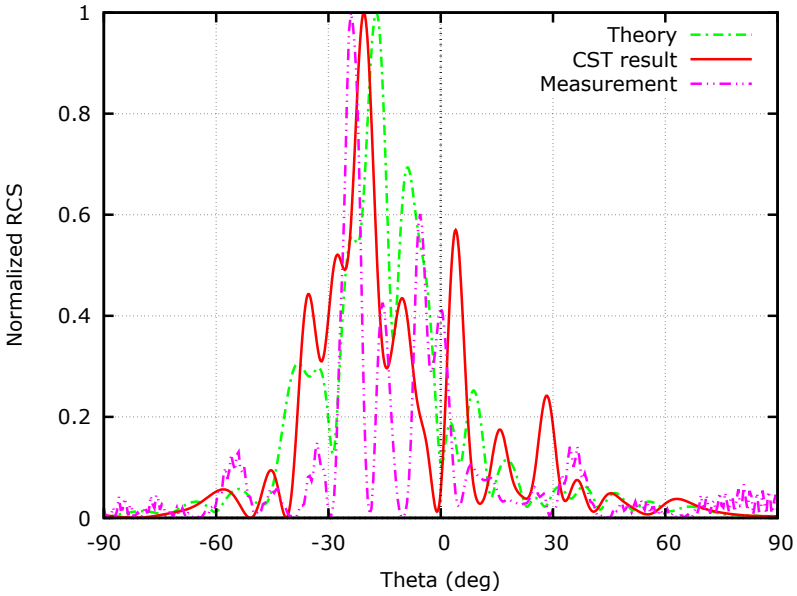

FIGURE 5.11: Comparison of the analytical, numerical and measurement results for the normalized bi-static radar cross section.

in the milling process that tends to make slots and gaps in the metallization slightly wider than required. By measuring the dimensions of the unit cell elements under a microscope, it was found that, on average, the gaps between the patches were 0.09 mm bigger as compared with the required values. The standard deviation of the measured systematic increase in the gap size was 0.03 mm. These rather high values of the errors inherent to the production process explain the difference between the measurement and the simulation results. Indeed, the minimum gap in metallization made by the milling process is 0.2 mm, which is very close to the minimum feature size in the structure (also about 0.2 mm), therefore these small features could not be reproduced with a high accuracy. Nevertheless, considering all the inaccuracies the behaviour of the prototype structure follows the desired pattern.

5.5 Conclusion

The focus of this work has been on developing a new approach to so-called coding metasurfaces. The approach is based on the use of fractal interpolation functions (FIF). FIF are a versatile tool to produce quasi-random self-similar patterns. Here, we have used such patterns to model the far-field scattering characteristics of a reflectarray realized as a metasurface with

FIF-encoded reflection phase. We have proved analytically that if the reflection phase distribution belongs to a specific class of FIF, then the far-field radiation pattern of the structure is also approximately a FIF. In order to test this concept in practice, we have proposed a method to construct metasurfaces with a given phase distribution pattern by using arrays of slotted patches. A number of simulations in CST Microwave Studio have been performed to determine the geometry of the unit cells which results in the largest reflection phase variation with respect to the variation of the structural parameters. In the next step, the designed metasurface has been prototyped and its performance has been evaluated with direct measurements of bi-static RCS of the structure in an anechoic chamber. Although the prototype has demonstrated expected behaviour close to the main lobe of the reflection pattern, we have found that the inaccuracies associated with the used production method (CNC milling) prevented us from reproducing the expected behaviour in the sidelobe regions.

Chapter 6

Conclusions and Future Work

6.1 Conclusions

In this work we investigated the fractal-based metamaterials. We developed several theoretical and numerical models applicable to the class of fractal MMs. The self-similar fractals, which were the main focus of this work, showed a great potential in enabling analytical modelling for such rather complicated structures.

In the case of the 1D MM based on a fractal set, we developed a homogenization method using the self-similarity property of the fractal set. The analytically derived effective parameters were verified numerically. It was shown that, in the quasi-static limit, the effective permittivity of such MM is a weighted average of the permittivities of the dielectric layers in the fractal, which agrees well with similar results obtained for the quasi-static behaviour of periodic layered media and further validates our method of homogenization. In order to solve Maxwell's equations, we used a recursive function approach inherent to the fractal nature of the problem. We also generalized this method for 1D fractal MM at higher frequencies, and, for the non-magnetic case, the effective permittivity dyadic analytically derived with this framework were validated numerically by FDTD simulations.

For the case of 2D fractal MM, we designed and studied a metasurface based on the space-filling curves, in our case, the Hilbert curve. To homogenize this structure, we calculated the effective surface impedance of the structure. The self-similarity properties of this fractal structure allowed us to develop an equivalent circuit model based on an extension of the Babinet-Booker's principle for electromagnetic fields. The results from the analytical model

and the simulations were in good agreement. The developed methods are applicable for other MM structures exhibiting self-similarity and complementarity properties.

The 3D fractal wire medium (WM) was another topic of investigation. In this problem, unlike the traditional WM, we distributed the wires based on the Sierpinski carpet fractal. The fractal distribution influenced both the positions and the diameters of the wires. We simulated the band diagrams for the TE and TM polarization cases. The result suggested that the fractal WM can result in lighter and more compact structure as compared to the traditional WM.

In another part of this thesis, we developed a new approach to coding metasurfaces, which we named fractal coding metasurfaces. The fractal coding metasurfaces can be used in reflectarrays for beam forming and controlling applications. We used an approach based on the fractal interpolation functions (FIF) in order to generate the necessary quasi-random self-similar patterns of the reflection phase. The FIF properties helped us to model the far-field scattering characteristics of the structure with the FIF-encoded reflection phase. Most importantly, we proved analytically that if the reflection phase distribution belongs to the special class of FIFs, then the far-field radiation pattern of the structure is also approximately a FIF. We proposed a method for the construction of an array of slotted patches realizing the given phase distribution . The method is not dependent on the unit cell design. We checked our method by numerical simulation of an example of such structure. We also designed a prototype of a FIF-based reflectarray and measured the resulted radiation pattern. The simulations and the experimental results showed close relation.

6.2 Future Work

The idea of using fractal geometry in the design of MMs is very young and still has great potential for future investigation. In this work, the focus has been primarily on the self-similar fractals, however, this class of fractals comprises just a small group of such objects. Investigating other classes of fractals, especially the random fractals, which are characterized by a richer set of parameters, may open new horizons in applications of such structures in the design of the EM MMs.

The homogenization approaches developed in this work apply to the structures having infinite extents in 1D, 2D, or 3D spaces. However, such simplifying assumptions may lead to

inaccuracies when considering practical designs. Thus one possible extension is to develop homogenization techniques which are able to take into account the edge effects in the finite fractal arrays. It is interesting to look for the relation between the effective parameters of the infinite and finite structures, and study, e.g. how the number of unit cells in a structure affects these parameters.

In this thesis, the EM fractal MMs have been investigated. However, similar ideas can be developed, for example, for acoustic metamaterials, since the acoustic wave propagation in certain systems obeys similar wave equations. The concept of homogenization is as well applicable in acoustics. In particular, homogenization of the acoustic MMs implies calculating effective Young's modulus and mass density, which are similar to the permittivity and permeability of the EM MMs. Although acoustic MMs are already a well establish concept, there is still lots to be done for the fractal acoustic MMs.

Appendix A

General Remarks on Homogenization

In general, the response of a medium to the applied electromagnetic field can be expressed through a set of polarizability tensors. The polarizability tensors represent the linearisation[1] of the response of a material to an applied electric and/or magnetic field for small field strengths, and therefore provide a first order approximation to said response. For example, in a MM formed by many arrays of inclusions distributed in a fractal manner, each inclusion will have the polarizability tensor defined with respect to the average electric filed in the MM. This polarizability depends on the fractal structure. Namely, considering the induced electric polarization density $\mathbf{P}$ as a function of the average electric field $\mathbf{E}$, the electric polarizability tensor χ_{ij} is defined as the Frechet derivative of $\mathbf{P}$ with respect to $\mathbf{E}$ at $\mathbf{E} = 0$, that is, $\chi_{ij} = \partial P_i/\partial E_j|_{\mathbf{E}=0}$.[2] In chiral and bi-anisotropic media, the electric field $\mathbf{E}$ can induce magnetic polarization $\mathbf{M}$, and *vice versa*, the magnetic field $\mathbf{H}$ can induce electric polarization $\mathbf{P}$, so that in this more general case

$$P_i = \chi_{ij}^{ee} E_j + \chi_{ij}^{em} H_j, \tag{A.1}$$

$$M_i = \chi_{ij}^{me} E_j + \chi_{ij}^{mm} H_j \tag{A.2}$$

where $\chi_{ij}^{ee} = \partial P_i/\partial E_j|_{\mathbf{E}=\mathbf{H}=0}$, $\chi_{ij}^{em} = \partial P_i/\partial H_j|_{\mathbf{E}=\mathbf{H}=0}$, etc.

[1] The response of a MM can be nonlinear if it includes certain types of dielectrics or semiconductors or ferrites, for example.

[2] For sufficiently small $\mathbf{E}$, we can expand $\mathbf{P}$ as a Taylor series: $\mathbf{P} = \mathbf{P}(\mathbf{E} = 0) + \chi\mathbf{E} + O(||E||^2)$ where the higher order terms are small. And, because we assume $\mathbf{P} = 0$ when $\mathbf{E} = 0$ (no polarization without applied field), we are left with: $P_i = \chi_{ij} E_j$ where the repeated indices denote summation (Einstein notation).

After the polarizability tensors are found, the homogenization problem is solved and the dispersion equation for the wave propagating in the media can be formulated from solving the uniform Maxwell equations

$$\nabla \times \mathbf{E} = -j\omega(\mu_0 \mathbf{H} + \mathbf{M}), \tag{A.3}$$

$$\nabla \times \mathbf{H} = j\omega(\varepsilon_0 \mathbf{E} + \mathbf{P}) \tag{A.4}$$

1D Fractal Metamaterials

Typically, when dealing with such MMs the purpose is to find the dispersion relation for the waves propagating in a single chain (or multiple parallel chains) of subwavelength elements repeated in a fractal manner. Analytical formulas can be derived expressing the material parameters of such 1D-media and their relation to the fractal iteration level. In particular, the effective dielectric permittivity can be calculated in each case.

The above mentioned traditional approach, however, is not always the best one when applied to 1D structures. In 1D structures, where the propagation happens along just a single direction, it is possible to obtain the effective parameters by using the ABCD (transfer) matrix. Thus, a 1D fractal MM can be realized as a layered dielectric structure, and the EM properties of this structure can be studied by the ABCD matrix approach.

2D Fractal Metamaterials

In order to homogenize two-dimensional MMs, the effective surface polarizability tensors need to be calculated for the metasurfaces which describe the homogenized behaviour of these structures.

These quantities relate (in the linear approximation) the induced surface currents (electric and/or magnetic) with the fields at the metasurface. Analytical expressions relating these quantities with the scattering matrix elements of the metasurface need to be derived, as well as a method of extraction of the polarizability tensor components from a set of reflection/-transmission measurements will be developed. The method should take into account the peculiarities inherent to fractal structures, such as the pseudo-random scattering pattern and the geometrical self-similarity properties.

3D Fractal Metamaterials

To homogenise three-dimensional fractal MMs means to derive a form of material relations applicable to this class of MMs. In order to find such effective parameters, one can start with the Tellegen form of material relations describing interaction between electric and magnetic polarizations and fields in a reciprocal medium:

$$\mathbf{D} = \varepsilon\mathbf{E} + \zeta\mathbf{H}, \tag{A.5}$$

$$\mathbf{B} = \mu\mathbf{H} - \zeta^T\mathbf{E}. \tag{A.6}$$

Here, the material tensors ε, μ, and ζ are functions of frequency (accounting for the frequency dispersion) and the wave vector (accounting for the spatial dispersion).

An analytical-numerical homogenization technique based on the works of [34] can be developed for such cases.

Appendix B

Embedded External Source for Homogenization

To explain better the presence of the embedded external source which we take in a form of a plane wave of current spread over all dielectric layers, let us consider the following source in which the current is concentrated within infinitely thin sheets (of any physical nature, for example, they can be formed by grids of very thin ideally conducting wires with fixed currents; when such wires are very thin they do not influence the average electromagnetic field due to the high effective inductance and, respectively, high effective reactive impedance of the wires [70]) placed in the infinitesimal gaps between the adjusting dielectric layers of the periodically repeated fractal supercells. Mathematically, this source can be written as Eq. (B.1).

$$\vec{J}_{\text{ext}}(z) = \sum_{n=-\infty}^{+\infty} \vec{J}_{\text{s,ext}} e^{ik_z z} \delta(z - nL_N), \tag{B.1}$$

where $\vec{J}_{\text{s,ext}}$ is the sheet surface current (located at $z = 0$), $L_N = L \times N_{\text{cells}}$ is the size of a supercell formed by N_{cells} adjusting fractal cells, and $\delta(z)$ is the Dirac delta function. The source from Eq. (B.1) is Bloch-periodic: $\vec{J}_{\text{ext}}(z + L_N) = \vec{J}_{\text{ext}}(z) e^{ik_z L_N}$, where k_z is a unrestricted parameter which determines the phase shift between currents in different sheets.

Maxwell's equations and boundary conditions for the first supercell at $[0, L_N]$ are:

$$\nabla \times \vec{E} = i\omega\mu_0\vec{H},$$
$$\nabla \times \vec{H} = -i\omega\epsilon_0\epsilon_{\mathrm{r}}(z)\vec{E} + \vec{J}_{\mathrm{s,ext}}\delta(z), \tag{B.2}$$
$$\text{BCs:} \quad \vec{E}, \vec{H}\big|_{z=L_N} = \vec{E}, \vec{H}\big|_{z=0} e^{ik_z L_N}. \tag{B.3}$$

We can expand the source term in the Fourier-Bloch series:

$$\vec{J}_{\mathrm{ext}}(z) = \sum_{n=-\infty}^{+\infty} e^{i\frac{2\pi}{L_N}nz} e^{ik_z z}\vec{C}_n, \tag{B.4}$$

where

$$\vec{C}_n = \frac{1}{L_N}\int_{-L_N/2}^{L_N/2} \vec{J}_{\mathrm{s,ext}} e^{ik_z z}\delta(z) e^{-i\frac{2\pi}{L_N}nz} dz$$
$$= \frac{1}{L_N}\vec{J}_{\mathrm{s,ext}}. \tag{B.5}$$

By substituting the Eq. (B.5) into Eq. (B.4), we have the final expression for the source. It has the same form as the one which has been used in the analytical and numerical calculations.

$$\vec{J}_{\mathrm{ext}}(z) = \frac{\vec{J}_{\mathrm{s,ext}}}{L_N} e^{ik_z z} \sum_{n=-\infty}^{+\infty} e^{i\frac{2\pi}{L_N}nz}. \tag{B.6}$$

So it is safe to say that the embedded source used in the calculations can be represented in practice by current sheets placed at the boundaries of fractal supercells. By means of Fourier-Bloch expansion we prove that such a source is equivalent to a superposition of many distributed plane wave sources.

As an alternative approach to obtain a distributed source with a given profile, we can add a series of electrodes placed in pairs [one electrode above the structure (at $x = \frac{h}{2}$) and one electrode below the structure (at $x = -\frac{h}{2}$)], separated along the z-axis by $\Delta z \ll \lambda$, with each such pair of electrodes connected to an AC current source with complex amplitude $I_n \equiv I(z_n)$ (here and below we work in the frequency domain), where z_n is the coordinate of the pair at the z-axis. The vertical distance, h, between the electrodes in pairs is considered to be sufficiently small.

Without the fractal structure present (i.e., when the electrodes are separated by vacuum) each vertical pair of electrodes acquires voltage $V_n = -\frac{I_n}{i\omega C}$, where C is the capacitance of the electrode pair in vacuum. Thus, when the fractal structure is present, we can say that electrodes induce external electric field $\vec{E}_{\text{ext}}(z_n) = \frac{\vec{x}_0 V_n}{h}$ in this structure (the same process creates also magnetic field $\vec{H}_{\text{ext}}$, as predicted by the Maxwell's equations). On the other hand, for the total field inside the structure we can write:

$$\begin{aligned} \vec{E}_{\text{tot}} &= \vec{E}_{\text{ext}} + \vec{E}, \\ \vec{H}_{\text{tot}} &= \vec{H}_{\text{ext}} + \vec{H}. \end{aligned} \tag{B.7}$$

As we will show below, the fields $\vec{E} = \vec{E}_{\text{tot}} - \vec{E}_{\text{ext}}$ and $\vec{H} = \vec{H}_{\text{tot}} - \vec{H}_{\text{ext}}$ in the above expressions can be understood as the fields created by a distributed plane wave current source. We can write Maxwell's equations inside the dielectric while it is polarized by the electrodes:

$$\begin{aligned} \nabla \times \vec{E}_{\text{tot}} &= i\omega\mu_0 \vec{H}_{\text{tot}}, \\ \nabla \times \vec{H}_{\text{tot}} &= -i\omega\epsilon_0\epsilon_{\text{r}}(z)\vec{E}_{\text{tot}}. \end{aligned} \tag{B.8}$$

For the external fields in absence of the dielectric layers, we can write the following equations:

$$\begin{aligned} \nabla \times \vec{E}_{\text{ext}} &= i\omega\mu_0 \vec{H}_{\text{ext}}, \\ \nabla \times \vec{H}_{\text{ext}} &= -i\omega\epsilon_0 \vec{E}_{\text{ext}}. \end{aligned} \tag{B.9}$$

By subtracting the Eq. (B.9) from Eq. (B.8), and substituting Eq. (B.7), we will have the relations for the electric and magnetic fields $\vec{E}$ and $\vec{H}$:

$$\begin{aligned} &\nabla \times \vec{E} = i\omega\mu_0 \vec{H}, \\ &\nabla \times \vec{H} = -i\omega\epsilon_0\epsilon_{\text{r}}(z)\vec{E}_{\text{tot}} + i\omega\epsilon_0\vec{E}_{\text{ext}} = -i\omega\epsilon_0\epsilon_{\text{r}}(z)\vec{E} + \vec{J}_{\text{ext}}, \end{aligned} \tag{B.10}$$

where

$$\begin{aligned} \vec{J}_{\text{ext}} &\equiv -i\omega\epsilon_0(\epsilon_{\text{r}}(z) - 1)\vec{E}_{\text{ext}} \\ &= -i\omega\epsilon_0(\epsilon_{\text{r}}(z) - 1)\frac{V_n}{h}\vec{x}_0 = \epsilon_0(\epsilon_{\text{r}}(z) - 1)\frac{I_n}{Ch}\vec{x}_0, \end{aligned} \tag{B.11}$$

and here the distributed external current $\vec{J}_{\text{ext}}$ is expressed through the source currents I_n. And this can be a way of implementing the distributed external current in practice.

Appendix C

Simulation Control file for MPB for 1D Fractal MM

```
;; These functions are used to define the fractal

(define 1D-fractal
  (lambda (cen L eps1 eps2 ratio order)
   (if (> order 0)
    (append
     (1D-fractal (+ (* -0.5 L (- 1 ratio)) cen)
                 (* ratio L) eps2 eps1 ratio (- order 1))
     (list (list cen (* L (- 1 (* 2 ratio))) eps1))
     (1D-fractal (+ (* 0.5 L (- 1 ratio)) cen)
                 (* ratio L) eps2 eps1 ratio (- order 1)))
   (list (list cen L eps1)))))

;; MPB related

(set! num-bands 4)

;; all k vectors lie in xz plane

; only kz is changing (propagation normal to the layers)
```

```
(set! k-points (list
            (vector3 0 0 0)
            (vector3 0 0 0.5)))

(set! k-points (interpolate 31 k-points))

;; This function takes the list of coordinates of centres
;; of dielectric layers and the values of epsilon and
;; makes the structure for MPB

(define make-fractal-structure
    (lambda (objs acc)
    (if (pair? objs)
        (let* ( (obj (car objs))
            (rest (cdr objs))
            (cen (car obj))
            (d (cadr obj))
            (eps (caddr obj)) )
            (make-fractal-structure
            rest
            (cons        ;cons: construct the pair out of elements
                (make block
                (center 0 0 cen)
                (size no-size no-size d) ;no-size: infinite
                (material
                    (make dielectric (epsilon eps))))
                acc)))
        acc)))

(define-param cen 0)
(define-param L 1)
(define-param eps1 4)
(define-param eps2 1)
```

```
(define-param ratio 0.45)
(define-param order 11)

(set! geometry (make-fractal-structure
            (1D-fractal cen L eps1 eps2 ratio order) '()))

(set! geometry-lattice (make lattice (size no-size no-size L)))

(set! resolution (expt 2 (+ order 2))) ; resolution = 2^(n+3)

(run-yeven output-efield output-hfield) ; TE modes

(run-yodd output-efield output-hfield) ; TM modes
```

Bibliography

[1] Marcel Proust. *The Captive, The Fugitive*, volume 5 of *In Search of Lost Time*. Modern Library, 1993. ISBN 0679424776,9780679424772.

[2] V. G. Veselago. The electrodynamics of substances with simultaneously negative values of ϵ and μ. *Sov. Phys. Usp.*, 10:509–514, Jan-Feb 1968.

[3] L D Landau, L. P. Pitaevskii, and E. M. Lifshitz. *Electrodynamics of Continuous Media*. Elsevier, 2nd edition, Jan 1984.

[4] J. B. Pendry, A. J. Holden, W. J. Stewart, and I. Youngs. Extremely low frequency plasmons in metallic mesostructures. *Phys. Rev. Lett.*, 76:4773–4776, Jun 1996. doi: 10.1103/PhysRevLett.76.4773. URL http://link.aps.org/doi/10.1103/PhysRevLett.76.4773.

[5] J.B. Pendry, A.J. Holden, D.J. Robbins, and W.J. Stewart. Magnetism from conductors and enhanced nonlinear phenomena. *Microwave Theory and Techniques, IEEE Transactions on*, 47(11):2075–2084, Nov 1999. ISSN 0018-9480. doi: 10.1109/22.798002.

[6] R. A. Shelby, D. R. Smith, and S. Schultz. Experimental verification of a negative index of refraction. *Science*, 292(5514):77–79, 2001. doi: 10.1126/science.1058847. URL http://www.sciencemag.org/content/292/5514/77.abstract.

[7] J. B. Pendry. Negative refraction makes a perfect lens. *Phys. Rev. Lett.*, 85:3966–3969, Oct 2000. doi: 10.1103/PhysRevLett.85.3966. URL http://link.aps.org/doi/10.1103/PhysRevLett.85.3966.

[8] Nicholas Fang, Hyesog Lee, Cheng Sun, and Xiang Zhang. Sub-diffraction-limited optical imaging with a silver superlens. *Science*, 308(5721):534–537, 2005. doi: 10.1126/science.1108759. URL http://www.sciencemag.org/content/308/5721/534.abstract.

[9] J. B. Pendry, D. Schurig, and D. R. Smith. Controlling electromagnetic fields. *Science*, 312(5781):1780–1782, 2006. doi: 10.1126/science.1125907. URL http://www.sciencemag.org/content/312/5781/1780.abstract.

[10] Ulf Leonhardt. Optical conformal mapping. *Science*, 312(5781):1777–1780, 2006. doi: 10.1126/science.1126493. URL http://www.sciencemag.org/content/312/5781/1777.abstract.

[11] D. Schurig, J. J. Mock, B. J. Justice, S. A. Cummer, J. B. Pendry, A. F. Starr, and D. R. Smith. Metamaterial electromagnetic cloak at microwave frequencies. *Science*, 314 (5801):977–980, 2006. doi: 10.1126/science.1133628. URL http://www.sciencemag.org/content/314/5801/977.abstract.

[12] Jensen Li, Lei Zhou, C. T. Chan, and P. Sheng. Photonic band gap from a stack of positive and negative index materials. *Phys. Rev. Lett.*, 90:083901, Feb 2003. doi: 10.1103/PhysRevLett.90.083901. URL http://link.aps.org/doi/10.1103/PhysRevLett.90.083901.

[13] Ilya V. Shadrivov, Andrey A. Sukhorukov, and Yuri S. Kivshar. Complete band gaps in one-dimensional left-handed periodic structures. *Phys. Rev. Lett.*, 95:193903, Nov 2005. doi: 10.1103/PhysRevLett.95.193903. URL http://link.aps.org/doi/10.1103/PhysRevLett.95.193903.

[14] Shulin Sun, Xueqin Huang, and Lei Zhou. Two-dimensional complete photonic gaps from layered periodic structures containing anisotropic left-handed metamaterials. *Phys. Rev. E*, 75:066602, Jun 2007. doi: 10.1103/PhysRevE.75.066602. URL http://link.aps.org/doi/10.1103/PhysRevE.75.066602.

[15] Alexander A. Zharov, Ilya V. Shadrivov, and Yuri S. Kivshar. Nonlinear properties of left-handed metamaterials. *Phys. Rev. Lett.*, 91:037401, Jul 2003. doi: 10.1103/PhysRevLett.91.037401. URL http://link.aps.org/doi/10.1103/PhysRevLett.91.037401.

[16] Matthias W. Klein, Christian Enkrich, Martin Wegener, and Stefan Linden. Second-harmonic generation from magnetic metamaterials. *Science*, 313(5786):502–504, 2006. doi: 10.1126/science.1129198. URL http://www.sciencemag.org/content/313/5786/502.abstract.

[17] Yongmin Liu, Guy Bartal, Dentcho A. Genov, and Xiang Zhang. Subwavelength discrete solitons in nonlinear metamaterials. *Phys. Rev. Lett.*, 99:153901, Oct 2007. doi: 10.1103/PhysRevLett.99.153901. URL http://link.aps.org/doi/10.1103/PhysRevLett.99.153901.

[18] Constantin R Simovski and Sailing He. Frequency range and explicit expressions for negative permittivity and permeability for an isotropic medium formed by a lattice of perfectly conducting ω particles. *Physics Letters A*, 311(2–3):254 – 263, 2003. ISSN 0375-9601. doi: http://dx.doi.org/10.1016/S0375-9601(03)00494-8. URL http://www.sciencedirect.com/science/article/pii/S0375960103004948.

[19] Hongsheng Chen, Lixin Ran, Jiangtao Huangfu, Xianmin Zhang, Kangsheng Chen, Tomasz M. Grzegorczyk, and Jin Au Kong. Left-handed materials composed of only s-shaped resonators. *Phys. Rev. E*, 70:057605, Nov 2004. doi: 10.1103/PhysRevE.70.057605. URL http://link.aps.org/doi/10.1103/PhysRevE.70.057605.

[20] Viktor Podolskiy, Andrey Sarychev, and Vladimir Shalaev. Plasmon modes and negative refraction in metal nanowire composites. *Opt. Express*, 11(7):735–745, Apr 2003. doi: 10.1364/OE.11.000735. URL http://www.opticsexpress.org/abstract.cfm?URI=oe-11-7-735.

[21] G. Dolling, C. Enkrich, M. Wegener, J. F. Zhou, C. M. Soukoulis, and S. Linden. Cut-wire pairs and plate pairs as magnetic atoms for optical metamaterials. *Opt. Lett.*, 30(23):3198–3200, Dec 2005. doi: 10.1364/OL.30.003198. URL http://ol.osa.org/abstract.cfm?URI=ol-30-23-3198.

[22] A. V. Rogacheva, V. A. Fedotov, A. S. Schwanecke, and N. I. Zheludev. Giant gyrotropy due to electromagnetic-field coupling in a bilayered chiral structure. *Phys. Rev. Lett.*, 97:177401, Oct 2006. doi: 10.1103/PhysRevLett.97.177401. URL http://link.aps.org/doi/10.1103/PhysRevLett.97.177401.

[23] J. Van Kranendonk and J.E. Sipe. V foundations of the macroscopic electromagnetic theory of dielectric media. volume 15 of *Progress in Optics*, pages 245 – 350. Elsevier, 1977. doi: http://dx.doi.org/10.1016/S0079-6638(08)70480-3. URL http://www.sciencedirect.com/science/article/pii/S0079663808704803.

[24] J.-M. Lerat, N. Malléjac, and O. Acher. Determination of the effective parameters of a metamaterial by field summation method. *Journal of Applied Physics*, 100(8):084908, 2006. doi: http://dx.doi.org/10.1063/1.2355427. URL http://scitation.aip.org/content/aip/journal/jap/100/8/10.1063/1.2355427.

[25] David R. Smith and John B. Pendry. Homogenization of metamaterials by field averaging (invited paper). *J. Opt. Soc. Am. B*, 23(3):391–403, Mar 2006. doi: 10.1364/JOSAB.23.000391. URL http://josab.osa.org/abstract.cfm?URI=josab-23-3-391.

[26] A. M. Nicolson and G. F. Ross. Measurement of the intrinsic properties of materials by time-domain techniques. *IEEE Transactions on Instrumentation and Measurement*, 19(4):377–382, Nov 1970. ISSN 0018-9456. doi: 10.1109/TIM.1970.4313932.

[27] W. B. Weir. Automatic measurement of complex dielectric constant and permeability at microwave frequencies. *Proceedings of the IEEE*, 62(1):33–36, Jan 1974. ISSN 0018-9219. doi: 10.1109/PROC.1974.9382.

[28] D. R. Smith, S. Schultz, P. Markoš, and C. M. Soukoulis. Determination of effective permittivity and permeability of metamaterials from reflection and transmission coefficients. *Phys. Rev. B*, 65:195104, Apr 2002. doi: 10.1103/PhysRevB.65.195104. URL http://link.aps.org/doi/10.1103/PhysRevB.65.195104.

[29] Xudong Chen, Tomasz M. Grzegorczyk, Bae-Ian Wu, Joe Pacheco, and Jin Au Kong. Robust method to retrieve the constitutive effective parameters of metamaterials. *Phys. Rev. E*, 70:016608, Jul 2004. doi: 10.1103/PhysRevE.70.016608. URL http://link.aps.org/doi/10.1103/PhysRevE.70.016608.

[30] Constantin R. Simovski and Sergei A. Tretyakov. Local constitutive parameters of metamaterials from an effective-medium perspective. *Phys. Rev. B*, 75:195111, May 2007. doi: 10.1103/PhysRevB.75.195111. URL http://link.aps.org/doi/10.1103/PhysRevB.75.195111.

[31] Constantin R. Simovski. Bloch material parameters of magneto-dielectric metamaterials and the concept of bloch lattices. *Metamaterials*, 1(2):62 – 80, 2007. ISSN 1873-1988. doi: http://dx.doi.org/10.1016/j.metmat.2007.09.002. URL http://www.sciencedirect.com/science/article/pii/S1873198807000229.

[32] O. Luukkonen, Stanislav I. Maslovski, and S.A. Tretyakov. A stepwise nicolson-ross-weir-based material parameter extraction method. *Antennas and Wireless Propagation Letters, IEEE*, 10:1295–1298, 2011. ISSN 1536-1225. doi: 10.1109/LAWP.2011.2175897.

[33] Chris Fietz and Gennady Shvets. 1d current driven metamaterial homogenization. volume 7754, pages 77540V–77540V–8, 2010. doi: 10.1117/12.860871. URL http://dx.doi.org/10.1117/12.860871.

[34] Andrea Alù. First-principles homogenization theory for periodic metamaterials. *Phys. Rev. B*, 84:075153, Aug 2011. doi: 10.1103/PhysRevB.84.075153. URL http://link.aps.org/doi/10.1103/PhysRevB.84.075153.

[35] John David Jackson. *Classical Electrodynamics*. Wiley, 3rd edition, Dec 1998.

[36] Vladimir M. Shalaev. Electromagnetic properties of small-particle composites. *Physics Reports*, 272(2–3):61 – 137, 1996. ISSN 0370-1573. doi: http://dx.doi.org/10.1016/0370-1573(95)00076-3. URL http://www.sciencedirect.com/science/article/pii/0370157395000763.

[37] S. Datta, C. T. Chan, K. M. Ho, and C. M. Soukoulis. Effective dielectric constant of periodic composite structures. *Phys. Rev. B*, 48:14936–14943, Nov 1993. doi: 10.1103/PhysRevB.48.14936. URL http://link.aps.org/doi/10.1103/PhysRevB.48.14936.

[38] O. Ouchetto, Cheng-Wei Qiu, S. Zouhdi, Le-Wei Li, and A. Razek. Homogenization of 3-d periodic bianisotropic metamaterials. *Microwave Theory and Techniques, IEEE Transactions on*, 54(11):3893–3898, Nov 2006. ISSN 0018-9480. doi: 10.1109/TMTT.2006.885082.

[39] Kenneth Falconer. *Fractal Geometry: Mathematical Foundations and Applications*. Wiley, 3rd edition, Jan 2014.

[40] Benoit B. Mandelbrot. *The Fractal Geometry of Nature*. Holt, Henry & Company, Inc., 1st edition, Aug 1982.

[41] Y. Kim and D. L. Jaggard. The Fractal Random Array. *Proceedings of the IEEE*, 74 (9):1278–1280, 1986. ISSN 15582256. doi: 10.1109/PROC.1986.13617.

[42] C. Puente-Baliarda, J. Romeu, R. Pous, and A. Cardama. On the behavior of the sierpinski multiband fractal antenna. *Antennas and Propagation, IEEE Transactions on*, 46(4):517–524, Apr 1998. ISSN 0018-926X. doi: 10.1109/8.664115.

[43] S. Costanzo, F. Venneri, G. Di Massa, A. Borgia, A. Costanzo, and A. Raffo. Fractal Reflectarray Antennas: State of Art and New Opportunities. *International Journal of Antennas and Propagation*, 2016:1–17, 2016. ISSN 1687-5869. doi: 10.1155/2016/7165143. URL https://www.hindawi.com/journals/ijap/2016/7165143/.

[44] M. Lehman. Fractal diffraction gratings built through rectangular domains. *Optics Communications*, 195(1-4):11–26, Aug 2001.

[45] Mitsuo Wada Takeda, Soshu Kirihara, Yoshinari Miyamoto, Kazuaki Sakoda, and Katsuya Honda. Localization of electromagnetic waves in three-dimensional fractal cavities. *Phys. Rev. Lett.*, 92:093902, Mar 2004. doi: 10.1103/PhysRevLett.92.093902. URL http://link.aps.org/doi/10.1103/PhysRevLett.92.093902.

[46] Yoshinari Miyamoto, Hideaki Kanaoka, and Soshu Kirihara. Terahertz wave localization at a three-dimensional ceramic fractal cavity in photonic crystals. *Journal of Applied Physics*, 103(10):103106, 2008. doi: http://dx.doi.org/10.1063/1.2924327. URL http://scitation.aip.org/content/aip/journal/jap/103/10/10.1063/1.2924327.

[47] Kazuaki Sakoda. Electromagnetic eigenmodes of a three-dimensional photonic fractal. *Phys. Rev. B*, 72:184201, Nov 2005. doi: 10.1103/PhysRevB.72.184201. URL http://link.aps.org/doi/10.1103/PhysRevB.72.184201.

[48] Yong-Jun Bao, Bo Zhang, Zhe Wu, Jian-Wen Si, Mu Wang, Ru-Wen Peng, Xiang Lu, Jun Shao, Zhi-feng Li, Xi-Ping Hao, and Nai-Ben Ming. Surface-plasmon-enhanced transmission through metallic film perforated with fractal-featured aperture array. *Applied Physics Letters*, 90(25):251914, 2007. doi: http://dx.doi.org/10.1063/1.2750528. URL http://scitation.aip.org/content/aip/journal/apl/90/25/10.1063/1.2750528.

[49] Xiaoguang Sun and Dwight L. Jaggard. Wave interactions with generalized cantor bar fractal multilayers. *Journal of Applied Physics*, 70(5):2500–2507, 1991. doi: http://dx.doi.org/10.1063/1.349407. URL http://scitation.aip.org/content/aip/journal/jap/70/5/10.1063/1.349407.

[50] M. Bertolotti, P. Masciulli, and C. Sibilia. Spectral transmission properties of a self-similar optical fabry-perot resonator. *Optics Letters*, 19(11):777–779, Jun 1994.

[51] Nader Engheta and Richard W Ziolkowski, editors. *Metamaterials: Physics and Engineering Explorations*. Wiley-IEEE Press, Aug 2006.

[52] Weijia Wen, Lei Zhou, Jensen Li, Weikun Ge, C. T. Chan, and Ping Sheng. Subwavelength photonic band gaps from planar fractals. *Phys. Rev. Lett.*, 89:223901, Nov 2002. doi: 10.1103/PhysRevLett.89.223901. URL http://link.aps.org/doi/10.1103/PhysRevLett.89.223901.

[53] Lei Zhou, Weijia Wen, C. T. Chan, and Ping Sheng. Reflectivity of planar metallic fractal patterns. *Applied Physics Letters*, 82(7):1012–1014, 2003. doi: http://dx.doi.org/10.1063/1.1553993. URL http://scitation.aip.org/content/aip/journal/apl/82/7/10.1063/1.1553993.

[54] Lei Zhou, C T Chan, and Ping Sheng. Theoretical studies on the transmission and reflection properties of metallic planar fractals. *Journal of Physics D Applied Physics*, 37, Feb 2004. doi: 10.1088/0022-3727/37/3/009.

[55] Lei Zhou, Weijia Wen, C. T. Chan, and Ping Sheng. Multiband subwavelength magnetic reflectors based on fractals. *Applied Physics Letters*, 83(16):3257–3259, 2003. doi: http://dx.doi.org/10.1063/1.1622122. URL http://scitation.aip.org/content/aip/journal/apl/83/16/10.1063/1.1622122.

[56] J.M. Hao, L. Zhou, and C.T. Chan. An effective-medium model for high-impedance surfaces. *Applied Physics A*, 87(2):281–284, 2007. ISSN 0947-8396. doi: 10.1007/s00339-006-3825-4. URL http://dx.doi.org/10.1007/s00339-006-3825-4.

[57] Weijia Wen, Z. Yang, Gu Xu, Yonghai Chen, Lei Zhou, Weikun Ge, C. T. Chan, and Ping Sheng. Infrared passbands from fractal slit patterns on a metal plate. *Applied Physics Letters*, 83(11):2106–2108, 2003. doi: http://dx.doi.org/10.1063/1.1611271. URL http://scitation.aip.org/content/aip/journal/apl/83/11/10.1063/1.1611271.

[58] Weijia Wen, Lei Zhou, Bo Hou, C. T. Chan, and Ping Sheng. Resonant transmission of microwaves through subwavelength fractal slits in a metallic plate. *Phys. Rev. B*, 72:153406, Oct 2005. doi: 10.1103/PhysRevB.72.153406. URL http://link.aps.org/doi/10.1103/PhysRevB.72.153406.

[59] Christophe Caloz and Tatsuo Itoh. *Electromagnetic Metamaterials: Transmission Line Theory and Microwave Applications*. Wiley-IEEE Press, Dec 2005.

[60] David Hilbert. Ueber die stetige Abbildung einer Linie auf ein Flächenstück. *Mathematische Annalen*, 38:12, 1891.

[61] Jacques Babinet. Beiträge zur meteorologischen Optik. *Annalen der Physik und Chemie*, 5(117):128–143, 1837.

[62] Moeini, Samaneh and Pedro, Jose Carlos. Fractal metamaterial based on sierpinski carpet. In *Antennas and Propagation Conference (LAPC), 2014 Loughborough*, pages 557–559, Nov 2014. doi: 10.1109/LAPC.2014.6996449.

[63] Moeini, Samaneh and Pedro, Jose Carlos. Material parameters extraction for 1d fractal metamaterial. In *First International Workshop on Metamaterials-by-Design*, Dec 2015.

[64] Samaneh Moeini. Homogenization of spatially dispersive 1d fractal metamaterials. In *Proc. SPIE*, volume 9883, pages 98830Z–98830Z–11, 2016. doi: 10.1117/12.2220590. URL http://dx.doi.org/10.1117/12.2220590.

[65] Moeini, Samaneh and Pedro, Jose Carlos. Extraction of material parameters in 1-d fractal metamaterial. *EPJ Applied Metamaterials*, 3:7, 2016. doi: 10.1051/epjam/2016007. URL http://dx.doi.org/10.1051/epjam/2016007.

[66] Moeini, Samaneh and Cui, Tie Jun. Metasurfaces with fractal coding of the far-field radiation pattern. In *Progress In Electromagnetics Research Symposium (PIERS)*. PIERS, May 2017.

[67] Samaneh Moeini and Tie Jun Cui. Fractal Coding Metamaterials. *Annalen der Physik*, 531(2):1800134, feb 2019. ISSN 00033804. doi: 10.1002/andp.201800134. URL http://doi.wiley.com/10.1002/andp.201800134.

[68] Samaneh Moeini. Homogenization of Fractal Metasurface Based on Extension of Babinet–Booker's Principle. *IEEE Antennas and Wireless Propagation Letters*, 18 (5):1061–1065, may 2019. ISSN 1536-1225. doi: 10.1109/LAWP.2019.2909134. URL https://ieeexplore.ieee.org/document/8681070/.

[69] David M. Pozar. *Microwave Engineering*. John Wiley & Sons, Inc, 4th edition, 2011. ISBN 978-0-470-63155-3. URL https://books.google.pt/books?id=JegbAAAAQBAJ.

[70] Sergei Tretyakov. *Analytical Modeling in Applied Electromagnetics*. Artech House, 2002. ISBN 978-1-58053-367-6.

[71] John D. Joannopoulos, Steven G. Johnson, Joshua N. Winn, and Robert D. Meade. *Photonic Crystals: Molding the Flow of Light*. Princeton University Press, 2 edition, 2008. ISBN 0691124566,9780691124568. URL http://press.princeton.edu/titles/8696.html.

[72] Ardavan F. Oskooi, David Roundy, Mihai Ibanescu, Peter Bermel, J.D. Joannopoulos, and Steven G. Johnson. Meep: A flexible free-software package for electromagnetic simulations by the fdtd method. *Computer Physics Communications*, 181(3):687 – 702, 2010. ISSN 0010-4655. doi: http://dx.doi.org/10.1016/j.cpc.2009.11.008. URL http://www.sciencedirect.com/science/article/pii/S001046550900383X.

[73] Jin Au Kong. *Electromagnetic Wave Theory*. John Wiley & Sons, 1986. ISBN 0471828238,9780471828235.

[74] Christopher L Holloway, Edward F Kuester, Joshua A Gordon, J. O'Hara, Jim Booth, and David R Smith. An Overview of the Theory and Applications of Metasurfaces: The Two-Dimensional Equivalents of Metamaterials. *IEEE Antennas and Propagation Magazine*, 54(2):10–35, apr 2012. ISSN 1045-9243. doi: 10.1109/MAP.2012.6230714. URL http://ieeexplore.ieee.org/document/6230714/.

[75] G. Peano. Sur une courbe, qui remplit toute une aire plane. *Mathematische Annalen*, 36(1):157–160, 1890. ISSN 00255831. doi: 10.1007/BF01199438.

[76] K. J. Vinoy, K. A. Jose, V. K. Varadan, and V. V. Varadan. Hilbert curve fractal antennas with reconfigurable characteristics. In *2001 IEEE MTT-S International Microwave Sympsoium Digest (Cat. No.01CH37157)*, volume 1, pages 381–384 vol.1, May 2001. doi: 10.1109/MWSYM.2001.966911.

[77] Jaume Anguera, Carles Puente, Enrique Martínez, and Edouard Rozan. The fractal hilbert monopole: A two-dimensional wire. *Microwave and Optical Technology Letters*, 36(2):102–104, 2002. doi: 10.1002/mop.10687. URL https://onlinelibrary.wiley.com/doi/abs/10.1002/mop.10687.

[78] J. M. González-Arbesú, S. Blanch, and J. Romeu. The hilbert curve as a small self-resonant monopole from a practical point of view. *Microwave and Optical Technology Letters*, 39(1):45–49, 2003. doi: 10.1002/mop.11122. URL https://onlinelibrary.wiley.com/doi/abs/10.1002/mop.11122.

[79] R. Azaro, F. Viani, L. Lizzi, E. Zeni, and A. Massa. A monopolar quad-band antenna based on a hilbert self-affine prefractal geometry. *IEEE Antennas and Wireless Propagation Letters*, 8:177–180, 2009. ISSN 1536-1225. doi: 10.1109/LAWP.2008.2001428.

[80] J. Huang, J. Shiao, and J. Wu. A miniaturized hilbert inverted-f antenna for wireless sensor network applications. *IEEE Transactions on Antennas and Propagation*, 58(9): 3100–3103, Sept 2010. ISSN 0018-926X. doi: 10.1109/TAP.2010.2052583.

[81] J. Li, T. Jiang, C. Cheng, and C. Wang. Hilbert fractal antenna for uhf detection of partial discharges in transformers. *IEEE Transactions on Dielectrics and Electrical Insulation*, 20(6):2017–2025, December 2013. ISSN 1070-9878. doi: 10.1109/TDEI.2013.6678849.

[82] M. Barra, C. Collado, J. Mateu, and J. M. O'Callaghan. Miniaturization of superconducting filters using hilbert fractal curves. *IEEE Transactions on Applied Superconductivity*, 15(3):3841–3846, Sept 2005. ISSN 1051-8223. doi: 10.1109/TASC.2005.850553.

[83] H. Parsamyan, A. Babajanyan, and K. Lee. Microwave fractal bandpass filters based on modified hilbert curves of the first and the second orders. *Journal of Contemporary Physics (Armenian Academy of Sciences)*, 53(2):146–151, Apr 2018. ISSN 1934-9378. doi: 10.3103/S1068337218020068. URL https://doi.org/10.3103/S1068337218020068.

[84] Stefano De Zuani, Thomas Reindl, Marcus Rommel, Bruno Gompf, Audrey Berrier, and Martin Dressel. High-order hilbert curves: Fractal structures with isotropic, tailorable optical properties. *ACS Photonics*, 2(12):1719–1724, 2015. doi: 10.1021/acsphotonics.5b00363. URL https://doi.org/10.1021/acsphotonics.5b00363.

[85] L. Yousefi and O. M. Ramahi. Artificial magnetic materials using fractal hilbert curves. *IEEE Transactions on Antennas and Propagation*, 58(8):2614–2622, Aug 2010. ISSN 0018-926X. doi: 10.1109/TAP.2010.2050438.

[86] H. Xu, G. Wang, and M. Qi. Hilbert-shaped magnetic waveguided metamaterials for electromagnetic coupling reduction of microstrip antenna array. *IEEE Transactions on Magnetics*, 49(4):1526–1529, April 2013. ISSN 0018-9464. doi: 10.1109/TMAG.2012.2230272.

[87] Ruirui Chen, Sucheng Li, Chendong Gu, Shahzad Anwar, Bo Hou, and Yun Lai. Electromagnetic characteristics of hilbert curve-based metamaterials. *Applied Physics A*, 117(2):445–450, Nov 2014. ISSN 1432-0630. doi: 10.1007/s00339-014-8679-6. URL https://doi.org/10.1007/s00339-014-8679-6.

[88] Gang Yong Song, Qiang Cheng, Bei Huang, Hui Yuan Dong, and Tie Jun Cui. Broadband fractal acoustic metamaterials for low-frequency sound attenuation. *Applied Physics Letters*, 109(13):131901, 2016. doi: 10.1063/1.4963347. URL https://doi.org/10.1063/1.4963347.

[89] Xinzhe Zhao, Guoqiang Liu, Chao Zhang, Dong Xia, Zhumao Lu, Xinzhe Zhao, Guoqiang Liu, Chao Zhang, Dong Xia, and Zhumao Lu. Fractal acoustic metamaterials for transformer noise reduction. *Applied Physics Letters*, 074101(113), 2018. ISSN 00036951. doi: 10.1063/1.5038431.

[90] R. J. Purser, Manuel Pondeca, and Sei-Young Park. Construction of a Hilbert curve on the sphere with an isometric parametrization of area. Technical Report July, 2009. URL http://www.emc.ncep.noaa.gov/officenotes/newernotes/on460.pdf.

[91] H. E J Neugebauer. Extension of babinet's principle to absorbing and transparent materials, and approximate theory of backscattering by plane, absorbing disks. *Journal of Applied Physics*, 28(3):302–307, 1957. ISSN 00218979. doi: 10.1063/1.1722735.

[92] H.G. Booker. Slot aerials and their relation to complementary wire aerials (Babinet's principle). *Journal of the Institution of Electrical Engineers - Part IIIA: Radiolocation*, 93(4):620–626, 1946. ISSN 2054-0744. doi: 10.1049/ji-3a-1.1946.0150. URL http://digital-library.theiet.org/content/journals/10.1049/ji-3a-1.1946.0150.

[93] X. Liu, W. Li, Z. Zhao, R. Lu, S. Zhu, Z. Xu, X. Chen, and A. Zhang. Babinet principle for anisotropic metasurface with different substrates under obliquely incident plane wave. *IEEE Transactions on Microwave Theory and Techniques*, 66(6):2704–2713, June 2018. ISSN 0018-9480. doi: 10.1109/TMTT.2018.2818150.

[94] S. I. Maslovski, S. A. Tretyakov, and P. A. Belov. Wire media with negative effective permittivity: A quasi-static model. *Microwave and Optical Technology Letters*, 35(1): 47–51, 2002. ISSN 1098-2760. doi: 10.1002/mop.10512. URL http://dx.doi.org/10.1002/mop.10512.

[95] Michael Fielding Barnsley. Fractal functions and interpolation. *Constructive Approximation*, 2(1):303–329, 1986. ISSN 01764276. doi: 10.1007/BF01893434.

[96] Cristian Della Giovampaola and Nader Engheta. Digital metamaterials. *Nat Mater*, 13(12):1115–1121, Dec 2014. ISSN 1476-1122. URL http://dx.doi.org/10.1038/nmat4082. Article.

[97] Tie Jun Cui, Mei Qing Qi, Xiang Wan, Jie Zhao, and Qiang Cheng. Coding metamaterials, digital metamaterials and programmable metamaterials. *Light Sci Appl*, 3:e218, Oct 2014. URL http://dx.doi.org/10.1038/lsa.2014.99. Original Article.

[98] Lanju Liang, Meiqing Qi, Jing Yang, Xiaopeng Shen, Jiquan Zhai, Weizong Xu, Biaobing Jin, Weiwei Liu, Yijun Feng, Caihong Zhang, Hai Lu, Hou-Tong Chen, Lin Kang, Weiwei Xu, Jian Chen, Tie Jun Cui, Peiheng Wu, and Shenggang Liu. Anomalous terahertz reflection and scattering by flexible and conformal coding metamaterials. *Advanced Optical Materials*, 3(10):1374–1380, 2015. ISSN 2195-1071. doi: 10.1002/adom.201500206. URL http://dx.doi.org/10.1002/adom.201500206.

[99] Xiang Wan, Mei Qing Qi, Tian Yi Chen, and Tie Jun Cui. Field-programmable beam reconfiguring based on digitally-controlled coding metasurface. *Scientific Reports*, 6: 20663 EP –, Feb 2016. URL http://dx.doi.org/10.1038/srep20663. Article.

[100] Vincenzo Galdi. Metasurfaces for Field Manipulation and Sensing. In *11th International Congress on Engineered Material Platforms for Novel Wave Phenomena–Metamaterials 2017*, Marseille, 2017.

[101] Sai Sui, Hua Ma, Jiafu Wang, Yongqiang Pang, Jieqiu Zhang, and Shaobo Qu. Two-dimensional qr-coded metamaterial absorber. *Applied Physics A*, 122(1):28, Dec 2015. ISSN 1432-0630. doi: 10.1007/s00339-015-9545-x. URL https://doi.org/10.1007/s00339-015-9545-x.

[102] Shuo Liu, Tie Jun Cui, Quan Xu, Di Bao, Liangliang Du, Xiang Wan, Wen Xuan Tang, Chunmei Ouyang, Xiao Yang Zhou, Hao Yuan, Hui Feng Ma, Wei Xiang Jiang, Jiaguang Han, Weili Zhang, and Qiang Cheng. Anisotropic coding metamaterials and their powerful manipulation of differently polarized terahertz waves. *Light Sci Appl.*, 5: e16076, May 2016. URL http://dx.doi.org/10.1038/lsa.2016.76. Original Article.

[103] Fu Liu, Mohammad Sajjad Mirmoosa, Xuchen Wang, Sergei Tretyakov, Anna C. Tasolamprou, Odysseas Tsilipakos, Alexandros Pitilakis, Nikolaos V. Kantartzis, Christos Liaskos, Maria Kafesaki, Eleftherios N. Economou, Costas M. Soukoulis, Sergi Abadal,

Albert Cabellos-Aparicio, and Eduard Alarcón. Programmable Metasurfaces: State of the art and Prospects. *Proceedings of the ISCAS '18*, 2018.

[104] Rui Yuan Wu, Chuan Bo Shi, Shuo Liu, Wei Wu, and Tie Jun Cui. Addition theorem for digital coding metamaterials. *Advanced Optical Materials*, 6(5):1701236, 2018. doi: 10.1002/adom.201701236. URL https://www.onlinelibrary.wiley.com/doi/abs/10.1002/adom.201701236.

[105] Tie Jun Cui. Microwave metamaterials—from passive to digital and programmable controls of electromagnetic waves. *Journal of Optics*, 19(8):084004, 2017. URL http://stacks.iop.org/2040-8986/19/i=8/a=084004.

[106] Massimo Moccia, Shuo Liu, Rui Yuan Wu, Giuseppe Castaldi, Antonello Andreone, Tie Jun Cui, and Vincenzo Galdi. Coding metasurfaces for diffuse scattering: Scaling laws, bounds, and suboptimal design. *Advanced Optical Materials*, 5(19):1700455, 2017. doi: 10.1002/adom.201700455. URL https://onlinelibrary.wiley.com/doi/abs/10.1002/adom.201700455.

[107] Mingbo Pu, Zeyu Zhao, Yanqin Wang, Xiong Li, Xiaoliang Ma, Chenggang Hu, Changtao Wang, Cheng Huang, and Xiangang Luo. Spatially and spectrally engineered spin-orbit interaction for achromatic virtual shaping. *Scientific Reports*, 5:1–6, 2015. ISSN 20452322. doi: 10.1038/srep09822.

[108] Cheng Huang, Jianing Yang, Xiaoyu Wu, Jiakun Song, Mingbo Pu, Changtao Wang, and Xiangang Luo. Reconfigurable metasurface cloak for dynamical electromagnetic illusions. *ACS Photonics*, 5(5):1718–1725, 2018. doi: 10.1021/acsphotonics.7b01114. URL https://doi.org/10.1021/acsphotonics.7b01114.

[109] Xin Xie, Xiong Li, Mingbo Pu, Xiaoliang Ma, Kaipeng Liu, Yinghui Guo, and Xiangang Luo. Plasmonic metasurfaces for simultaneous thermal infrared invisibility and holographic illusion. *Advanced Functional Materials*, 28(14):1706673, 2018. doi: 10.1002/adfm.201706673. URL https://onlinelibrary.wiley.com/doi/abs/10.1002/adfm.201706673.

[110] John E Hutchinson. Fractals and self similarity. *Indiana University Mathematics Journal*, 30:713–747, 1981. ISSN 0003-9527. doi: 10.1512/iumj.1981.30.30055.

[111] Krzysztof Ciesielski. On Stephan Banach and some of his results. *Banach J. Math. Anal. Banach Journal of Mathematical Analysis*, 1(1):1–10, 2007. URL http://www.math-analysis.org.

[112] Michael Fielding Barnsley and Andrew N. Harrington. The calculus of fractal interpolation functions. *Journal of Approximation Theory*, 57(1):14–34, 1989. ISSN 10960430. doi: 10.1016/0021-9045(89)90080-4.

[113] Zhigang Feng, Lixin Tian, and Jianli Jiao. Integration and Fourier Transform of Fractal Interpolation Functions. *Fractals*, 13(01):33–41, 2005. ISSN 0218-348X. doi: 10.1142/S0218348X05002726.

[114] Sophocles J. Orfanidis. *Electromagnetic Waves and Antennas*. Rutgers University, 2014. URL http://www.ece.rutgers.edu/~orfanidi/ewa/.